Experimental and theoretical investigations of radio-frequency and optical trapping potentials for atomic ions

by

Manas Sajjan

A thesis
presented to the University of Waterloo
in fulfillment of the
thesis requirement for the degree of
Master of Science
in
Physics (Quantum Information)

Waterloo, Ontario, Canada, 2020

Author's Declaration

I hereby declare that I am the sole author of this thesis. This is a true copy of the thesis, including any required final revisions, as accepted by my examiners.

I understand that my thesis may be made electronically available to the public.

Abstract

Over the years, trapped ion have emerged as one of the premier candidates for universal quantum simulation due to its long coherence time, low initialization and detection errors, robust high-fidelity gate sets and fully connected yet tunable spin-graph. In this thesis we exclusively focus on the generation of the trapping potential in a four-rod trap, one of the most commonly studied ion-trapping architecture. We elaborate the fabrication of the trapping electrodes using electro-etching techniques and explore the underlying mechanism in details. We discuss how these electrodes are powered by DC and RF field to generate the confining potential responsible for trapping the ions of interest in 3D. We conclude by studying how this trapping potential can be modified by external means like using an optical tweezer. Employing such an optical tweezer we propose a new quantum-thermodynamic protocol which shall allow us to experimentally access the thermal properties of a mixed-specie ion chain using a single-specie ion chain. The scheme is based on Jarynski's equality and obviates the need to trap dual-ionic species as far as illustrating the mechanical properties of the chain are concerned. We present results ratifying the utility of the proposal. The scheme is useful to obtain mode-specific thermal properties hitherto unexplored experimentally.

Acknowledgements

The primary vote of thanks should be extended to my supervisor Dr.K.R.Islam for the numerous discussions we had perfecting the outcome of each and every project elaborated in the thesis. He never lost faith in me through thick and thin and was ever-ready to discuss not only science but also life in general. His enthusiasm in deconstructing new results, perspicacity, dedication to his craft and keen scientific outlook are exemplary traits that I shall try to imbibe in my professional pursuits hereafter. It would'nt be an overstatement to say that this work is a culmination of our combined effort. I would also like to express my sincerest gratitude to Dr.Alan Jamison and Dr.Na Young Kim for agreeing to be in my advisory committee and scrutinizing the contents of this thesis. Thanks should also be extended to Dr.Crystal Senko for sharing her insight with the members of the QITI group in the discussions we had during our joint group meetings.

A big shout out to my fellow group members at QITI lab both past and present - Roland, Sainath, Gilbert, Nikhil, Feresteh, Yi Hong, Zewen, Nik and all Co-op students (apologies if I have missed a name inadvertently). It was great sharing office space with Gilbert and Nikhil both of whom were ever ready to teach me the nuances of an experimental discipline such as this. Sainath time and again have been a great resource in the lab to dispel my doubts in any of my projects. I shall always cherish the late night discussions with him on our way back home. A special vote of thanks to Roland for taking me under his wing especially during the initial few months of my tenure here. Lot of this would'nt have been possible without his suggestions and help. Towards the end of my tenure, the theory team -Feresteh, Yi Hong,Zewen have been extremely helpful in developing the results of Chapter 4. Feresteh in general have been a great friend and colleague who I could always fall back to for any help and discussion. Our collaborators and friends in the Senko group- Pei Jiang, Brenden, Noah, Rich, Matt have always extended their support in the hour of need. A special mention for Pei Jiang for sharing his knowledge in designing the RF resonator elaborated in Chapter 3. Beyond the confines of IQC, my friends and roommates - Sourya, Soumik and Saptarshi have made my days in Waterloo entertaining.

On a personal front I express my gratitude to Dr.David Mazziotti of University of Chicago, Dr.Anindya Datta of IIT Bombay and Dr.Indranil Chakraborty of St.Xavier's College, Kolkata. Their respective influence in my life and scientific career is profound and have made me who I am today. Last but not least, I would like to express my gratitude toward my parents, Rishan, Supriya and Srijeeta- without the love, support and encouragement of all them, I cannot envision my life.

Dedication

This is dedicated to my parents and nephew.

Table of Contents

Chapter 1

Introduction

Quantum mechanics is entrusted with providing a computational paradigm to investigate the probabilities of various possible classical outcomes in the event of an observation being made on the system of interest. The theory envisages protocol for calculating the evolution of probability amplitudes associated with these outcomes and the post-measurement state of the system. For a generalized many-body quantum system of N mutually interacting particles each with m degrees of freedom, such probability amplitudes collectively form a vector that lives in a state space defined by the span of m^N classical configurations[1]. This essentially means that any effort to simulate the physical properties of such systems would require committing m^N complex valued probability amplitudes to the device memory, and handling linear transformations of dimensions $m^N \times m^N$ (assuming no symmetry restrictions which is usually present). This explicates clearly that even for modest system sizes, the task of simulating both statics and dynamics of many-interacting quantum systems on a classical computing platform can be daunting or even unrealistic due to the exponentially scaling resource overhead. An interesting way to solve the problem would be to harness the power of non-classical features like quantum superposition, entanglement etc to formulate computing devices. At its very core, such devices would in principle thus be using quantum-mechanics to gain insightful conclusion into the quantum description of systems of technological and/or scientific interest. This was proposed by Feynmann[2] and ever since have gained considerable attention. Over the past-two decades all efforts in this sub-field of study came to be unified under the broad purview of quantum simulation[3, 1].

For most quantum simulation schemes, the fundamental unit of information is encoded within a system with two computationally relevant degrees of freedom (m=2). Such a computational subspace is known as a qubit. Various platforms have been identified wherein universal quantum simulators based on qubits have been encoded and controlled like in cold atoms[4], trapped ions[5], photonics[6], superconducting qubits[7]to name a few. Other quantum simulation schemes wherein a qubit is not the fundamental manipulable unit of information also exists like in the simulation of Bose-Hubbard and Fermi-Hubbard Hamiltonian using optical lattices of ultracold atomic ensembles[8, 9]. Such studies are the not the focus of this thesis and shall not be discussed herein. For more information about these, an interested reader can refer to [4, 10].

Two specific approaches exists in simulating quantum properties of matter in qubit-based platforms. The first one, known as analog quantum simulation[11, 12, 13] requires choosing a simpler auxillary quantum system that can be effectively controlled and manipulated. The generator of time-translation (either Hamiltonian or the generalized Liouvillian) for the system of interest is then mapped onto that of the auxillary system. Evolving this auxillary system directly sheds invaluable insight into physical properties of the target system. Variants of this protocol in which the time translator of the auxillary sytem is modified slowly in real-time to match that of the target have also been studied and proposed[14]. The second approach known as digital quantum simulation[15, 16] involves decomposing the unitary evolution for the closed target system of interest into a sequence of quantum gates acting on a chosen qubit register. For open systems, wherein the dynamics is non-unitary, one approach involves dilating the generator onto a larger space into an implementable unitary gate[17]. Unlike the analog scheme which requires the existence of a mimic system and hence can be problem-specific, digital schemes are more universal. However digital schemes suffer from accumulation of errors due to approximate decomposition of the dynamics of the system into an available gate set (digitization error) Both schemes have been implemented to study a variety of problems [1, 18, 12, 19, 20]

Among the platforms mentioned for quantum simulation in the previous paragraph, trapped ions have emerged as a leading candidate due to its long coherence times[21],low initialization and detection errors[22, 23], innate indistinguishability of the ions which offers protection against fabrication defects unlike in superconducting qubits[24] and its fully connected yet programmable ion-ion interaction mediated by phonons[25]. Indeed a large variety of problems like quantum magnetism[26, 5], ground-state electronic structure of simple molecules[27], lattice gauge theories[28], thermalization vs localization dynamics[29] have been studied using this platform with reasonable accuracy. Most of the commonly used ions in this platform are that of the alkaline-earth metal category or heavier elements which after single-ionization generates a single-lone electron in an outermost shell much like that in a hydrogen-atom. Two different types of qubits are commonly used in this platform depending on the choice of electronic energy levels which are used to encode the information. For protocols using ions like $^{40}\mathrm{Ca}^{+}$, a narrow quadrupole allowed optical transition is used for qubit implementation[30]. Unlike that, for the case of $^{171}\mathrm{Yb}^{+}$ which we shall focus on in this thesis, the two hyperfine states of the ground state manifold generated by interaction of the electronic and nuclear spins is used as qubits [31]. Single-qubit operations in the latter category can either be initiated by microwave transitions[32, 23] between the hyperfine states or by two-photon Raman transitions[33]. For two qubit interaction, several proposals exists[34, 35, 36] all of which relies on mediation due to phonons of the crystallized ion chain. At the heart of it, such schemes couples the internal electronic and the external motional degrees of freedom optically. The protocols generate spin-dependant forces relayed by the targeted phonon bus[37]. Excellent reviews about such proposals can be found in Ref[25].

An universal quantum simulator using trapped ions for encoding the qubits can be built in several architectural designs[38]. Of the ones, a quadrupole blade-trap and a four-rod trap are more commonly employed and well studied. In this thesis we shall explore the construction and design of a four-rod trap that has been successfully built in the group over the past two years with special emphasis on the generation of the trapping potential by RF and DC fields. We shall also in the last chapter we shall also see how this trapping potential can be externally controlled/modified using an optical tweezer. In the following section, we shall study the outline for the various chapters of the thesis and the relevant contribution by the author.

1.1 Thesis Outline and Major Contributions by the author

- We shall see in Chapter 2 that a four-rod trap as the name suggests involves four rod shaped electrodes and two needle shaped electrodes to generate a confining potential for the ions in 3D. In Chapter 2 we shall study how these four rod-shaped electrodes and the two-needle shaped electrodes have been fabricated for the construction of the ion-trapping apparatus in the group. The author has successfully built all 4 of the rods and have also manufactured a pair of needles following protocol in Ref.[39]. For reasons to be discussed in Chapter 2, a new protocol have also been developed for generating needle-shaped electrodes from rods by one of the co-worker in the group[40]. To test the efficacy of the method, the final pair of needles that have been used in our trapping apparatus have been made using this protocol. The author is one of the co-developers of the protocol and will be a part of a publication under preparation elaborating the results. Unlike the needles, however the four rods developed by the author have been used in the present ion-trapping apparatus operational in the group.

- We shall learn in Chapter 3 that the four rods will have to be powered by an RF field to create a confining potential. The needles are powered by DC[41]. The author shall describe the details of the circuitry that has been implemented in the lab for powering the rods. One of the principal component of the circuit is an RF resonator which is a voltage amplifier and a frequency filter. The author has built the RF resonator that is used in the ion-trapping apparatus operational in the group and has designed the circuitry powering it. The chapter also has details of simulation undertaken by the author of the trapping potential created by the RF.

- We shall learn in Chapter 4 how to manipulate and change the trapping potential using optical tweezers. We shall investigate the effect of such tweezers on the internal electronic state as well as the external motional modes of the ion. We then propose an experiment of evaluating thermal properties of a particular trapped ionic species using optical tweezer on a different ionic species. The proposal is reliant on Jarynski's equality[42] and has not been hitherto implemented using optical tweezers on ion traps. Also the proposal allows computing thermodynamic properties of mixed-ion species using single-ion chains and can be generalized to obtain mode-specific properties, a scheme that has never been implemented in experimental ion-trapping platforms. The proposal is entirely new and the author is responsible for formulating the initial idea and has done all simulations shown in this chapter to ratify the proposal. The results of this chapter will appear as a publication under preparation.

Chapter 2

Construction of trapping electrodes

2.1 Chapter at a glance

The basic geometry used for trapping unipositive Yb ions in our experimental setup is that of a quadrupole trap [43, 44, 45, 46]. The setup is illustrated in Fig.2.1 with the relevant geometrical parameters of the six electrodes as used in our experiment. It is conventional to assign the principal symmetry axis (C_4) of the rods (and needles) to z-direction as denoted in Fig.2.1 . The two orthogonal directions in the transverse plane are assigned x and y as shown in Fig.2.1. The four cylindrical rod-shaped electrodes in the trap (see Fig.2.1) provides a time-dependant near-perfect hyperbolic potential in the transverse direction using AC electric field (see Chapter 3). The effective pseudopotential associated with this field is confining and harmonic. The two needle electrodes confine the ions along the z-direction creating a parabolic repulsive potential. For most experiments, the confining potential provided by the cylindrical rod-shaped electrodes are far higher than that of the two needles which expounds why multiple ions if trapped crystallizes into a linear chain along the principal symmetry axis (C_4). In this chapter, the following questions will be answered.

- How are the four rod-shaped electrodes (see Fig2.1) fabricated and what is the underlying mechanism for the process?
- How are the two needle-shaped electrodes (see Fig2.1) fabricated and what is the underlying mechanism for the process?

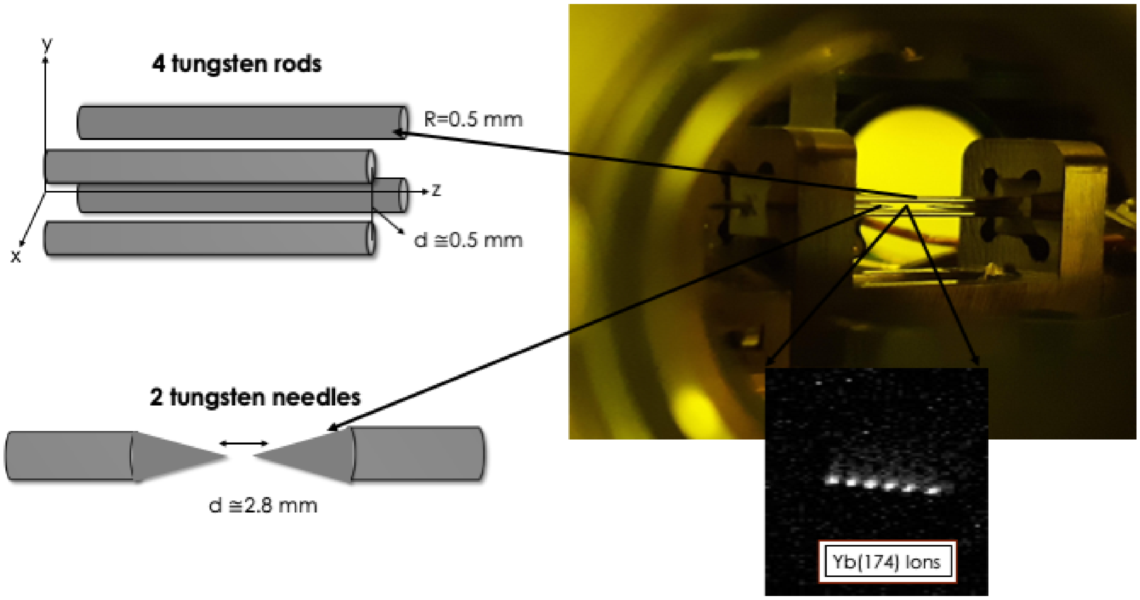

Figure 2.1: The picture of the trapping electrode system used in the actual experiment for trapping $^{174}\mathrm{Yb}^{+}$ and $^{171}\mathrm{Yb}^{+}$ ions. Set of trapping electrodes consists of 4 tungsten rods and 2 tungsten needles. The geometric parameters of each of these electrodes are magnified and highlighted on the left using the representative schematic of a cartoon

2.2 Fabrication and characterization of trap electrodes

The primary material we use for the construction of the rods would be tungsten.

Why use tungsten (W) for fabricating trap electrodes ?

- Tungsten(W) as a metal is very hard. has a Brinell hardness (HB) of 294[47], modulus of elasticity of 405 GPa[48] and tensile strength of 980 MPa[47]. This quality provides the electrodes mechanical strength against distortion during fabrication.

- DC electrical conductivity of tungsten is $1.79e7$ S/m[47] at 20 C° with a temperature coefficient of 0.0045 K^{-1} [49]. The skin depth of W at the frequency of our interest 10-20 MHz (see Chapter 3) is 27.1 μm[50] compared to more commonly used metals like copper(Cu) which has a DC electrical conductivity of $5.96e7$ S/m and skin depth of 14.6 μm [50] at similar frequencies. From the values indicated it is clear that W is an inferior electrical conductor unlike Cu(W has 4 times less DC conductivity and roughly twice as much skin depth over which the electrical energy can penetrate and be lost as heat). However unlike Cu, tungsten is not as readily oxidizable. The standard molar free energy of formation (ΔG_f°) of copper (II) oxide is -143.368 kJ/mol [51] and that of copper (I) oxide -142.020 kJ/mol [52] at 25 C°. Kinetically the oxidation activation energy at low temperature has been found to be 20-50 kJ/mol[53, 54] for both conversions dependant strongly on the presence of moisture, surface quality of the metal or dissolved ionic electrolytes. These oxides of copper so formed are semiconductors with a bandgap of 1-3 eV[55] and DC electrical conductivity orders of magnitude less than that of the pure metal. Measurements indicates copper(I) oxide has a DC electrical conductivity in the range of $1e{-}6$ to 0.1 S/m and for copper(II) oxide it is 100 to $1e5$ S/m depending on temperature, method of preparation, film thickness and environmental conditions[55, 56]. For tungsten, several different oxides are possible of the kind WO_{3-x}. Among these, WO_3 is most stable and has a ΔG_f° of -865.531 kJ/mol at 25 C° [51] which makes this oxide more stable with respect to the metal than the oxides of pure copper. However, kinetically the conversion is much slower with an activation energy of 90-200 kJ/mol[57, 58] with the lower values attainable only at higher temperatures. As a result the shelf-life/longevity of pure tungsten metal at a given pressure of oxygen will be higher than that of copper. DC electrical conductivity of WO_3 has been found to be 10 S/m at 25 C°[59] (dependant on method of preparation and thickness) which is comparable or even superior than oxides of copper for certain specifications. More noble metals like gold (Au) or platinum (Pt) too can act as a proxy to tungsten in this regard due to their relative inertness to oxide formation. However fabricating rods using these metals can be expensive

- The work function of Tungsten is 4.55 eV (272 nm)[60, 61, 62]. For optical addressing of the trapped Yb ions, we will use wavelengths like 369 nm, 355 nm, 935 nm, 399 nm. The function for W being high, photons of these frequencies will not be able to provide enough energy to photo-ionize W.

- Tunsgten is also vacuum compatible with an outgassing rate of 1.62e-10 Torr L s^{-1} cm^{-2} (obtained after 10 hours of initial pump down at ordinary temperature in [63])

- Tunsgten can also be electropolished easily using NaOH/KOH solution[64, 39, 65, 66, 67, 68] to improve texture and surface quality of the electrodes thereby eradicating structural imperfections should there be any.

Why electropolish commercial tungsten rods for fabricating trap electrodes ?

For the aforementioned reasons, commercially available tungsten rods from Midwest Tungsten Service (MTS) of diameter 0.53-0.55 mm were purchased and then electropolished for making the 4 rods. Without such electropolishing, the surface texture of the rods is seen to be dented and hence uneven and rough as is illustrated in Fig.2.2. Such dents as seen in the picture would be under 50 μm. Dents much smaller than that exists too but is not resolvable using the imaging setup used herein. Presence of such dents would create a non-uniform trapping potential for the ions and amplify micromotion. Micromotion as we shall see in Chapter 3 corresponds to motion induced in the ionic lattice due to the 'jitters' caused by directly following the fast RF driving frequency which is used to create the trapping potential[69]. Signatures of this motion is seen over and above the slower frequency harmonic motion induced by the trap. Excess micromotion can create additional sidebands in the excitation spectrum of the transition used for Doppler cooling of the ions. As a result, if the cooling laser is tuned above any of these sidebands , the ion would be heated up instead of being cooled irrespective of whether the laser is red-detuned from the addressed cooling transition[69]. Such heating reduces the lifetime of the ion in the trap and can aggressively populate the motional modes of these ions which can be detrimental to gate fidelities [70]. The macor holders responsible for housing the rods are also machined so as to accommodate the rods of correct diameter. It is hard commercially to obtain 4 compatible rods with an average diameter of exactly 0.5 mm and excellent surface quality at the length scale of the trapped ions. Electropolishing commercial rods of bigger diameters seems to satisfy both the conditions.

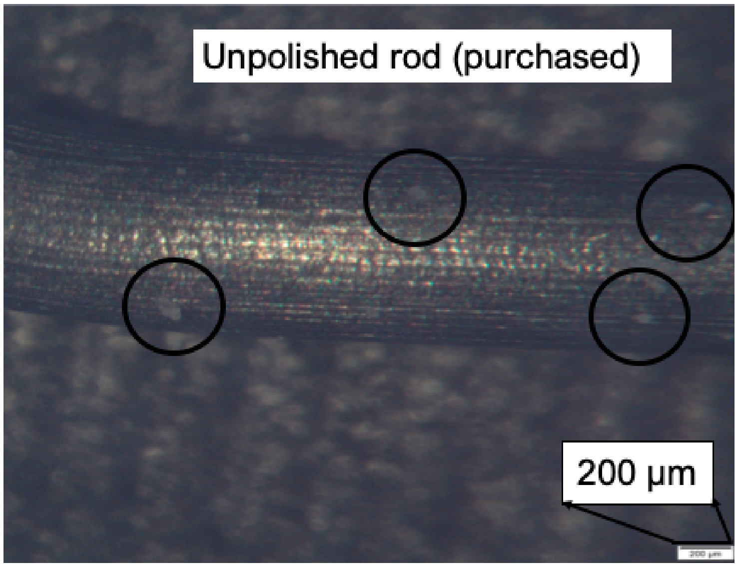

Figure 2.2: Surface quality of purchased rods with highlighted dents thereby illustrating need for electropolish. Lack of lustre and general roughness of the surface is also evident. The image is taken from the bare rods with 2.0x zoom

2.2.1 Mechanism of Electropolishing

The basic idea lies in the formation of an electrolytic cell created with a graphite (C) electrode as cathode(-) and the tunsgten rod to be electroetched as anode(+)[39]. It is important to have a schematic description of the set-up to understand the process well.The schematic of the set-up is illustrated in Fig2.3. The set-up uses NaOH solution of 2M concentration as the electrolytic bath. The tungsten rod to be polished is controlled mechanically by a translation stage which allows us to adjust the height of the rod dipped in the said bath. It is then connected to the positive electrode of a DC power supply thereby serving as the anode. A graphite rod connected to the negative terminal of the same power supply is also dipped into the same bath. A milli-ammeter is connected to the circuit in series to monitor the overall current.

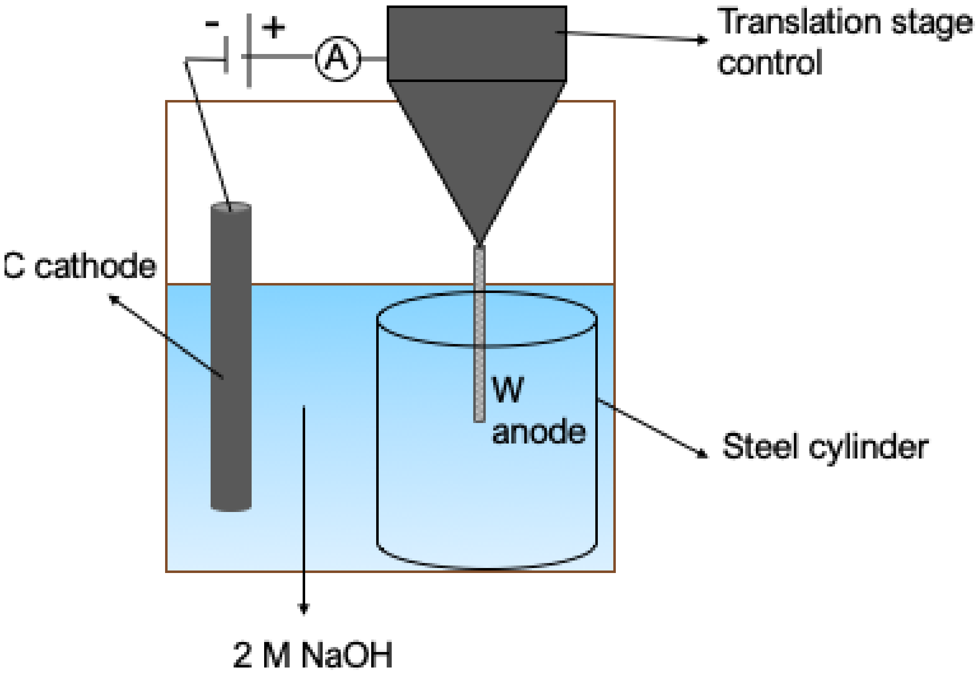

Figure 2.3: The schematic of the setup used for electropolishing tunsgten (W) electrodes.

Ref[65, 71] investigates the underlying mechanism for the oxidative dissolution of W to form tungstate ions ($WO_4{}^{-2}$) in alkaline medium. It proposes the formation of several insoluble intermediary tunsgten oxides((WO^+, WO_2, WO_3) and oxo-acids ($WO_3H, HWO_4{}^-$) which are eventually attacked by the alkali to form the said anionic radical. The reactions are:

$$\mathrm{W(s) + 2OH^- \rightarrow WO^+(s) + H_2O + 3e.} \tag{2.1}$$

$$\mathrm{WO^+(s) + 2OH^- \rightarrow WO_2 + H_2O + e.} \tag{2.2}$$

$$\mathrm{WO_2 + OH^- \rightarrow WO_3H + e} \tag{2.3}$$

$$\mathrm{WO_3H + OH^- \rightarrow WO_3 + e + H_2O} \tag{2.4}$$

$$\mathrm{WO_3 + OH^- \rightarrow HWO_4{}^-} \tag{2.5}$$

$$\underline{\mathrm{HWO_4{}^- + OH^- \rightarrow WO_4^{-2} + H_2O}} \tag{2.6}$$

$$\mathrm{At\ anode(W) : W(s) + 8OH^- \rightarrow WO_4^{-2} + 4H_2O + 6e} \qquad \mathrm{E^{\phi}_{W/WO_4{}^{-2}} = 1.05V[72]} \tag{2.7}$$

The stability of the involved species as a function of pH is elaborated in ref [65]. It claims that for pH ≥ 8 (which is the case as we use extremely concentrated NaOH beyond the range which produces a definable pH in the scale between 0-14), the most stable specie is ($WO_4{}^{-2}$) and thus all the equilibria from Eq.2.1 to 2.6 all lies to the right. For pH $\leq$ 8, WO_3 dominates and precipitates as a monohydrate whereas for pH $\leq$ 4, the pure WO_3 precipitates. The overall reaction in strongly alkaline medium thus can be summarized as electrolytic dissolution of solid tunsgten from rod to form soluble tungstate ions ($WO_4{}^{-2}$). This reaction happens at the oxidation half-cell (anode) as the oxidation state of tunsgten in the said tungstate radical is +6 (this is indeed oxidation as atomic tunsgten has electronic configuration of [Xe]$4f^14$ $5d^4$ $6s^2$ and an oxidation state of 0 in elemental state). At the cathodic half-cell we have a concomitant reduction of H_2O to H_2 which can be written as.

$$\text{At cathode(C)} : 6\mathrm{H_2O} + 6\mathrm{e} \rightarrow 3\mathrm{H_2} + 6\mathrm{OH}^-. \quad \mathrm{E}^{\phi}_{\mathrm{H_2O/H_2}} = -2.48\mathrm{V}[72] \tag{2.8}$$

From the above data, the overall cell potential is -1.43 V ($E^{\phi}_{\mathrm{H_2O/H_2}} + E^{\phi}_{W/\mathrm{WO_4}^{-2}}$). This is close to the conclusion in Fig.4.8,4.9,4.10 of ref[65] where the Pourbaix diagram shows elemental tungsten to be stable below -1.3 V for high pH but unstable with respect to tungstate above this value. Hence one requires an external DC power source with an applied potential of at least 1.43 V to drive the reaction. The evolution of H_2 at the cathode causes turbulence in the bath which may be detrimental to the overall surface quality of the tungsten rod. The purpose of the steel cylinder in Fig2.3 is to shield the anode from such disturbances. It has been empirically observed in Ref[39], that the cylindrical symmetry of the shield is necessary to create a uniform electric field at the tungsten anode thereby enhancing the final surface quality.

Even though the reaction requires only 1.43 V to be initiated under standard conditions as seen above, but in reality one needs to provide much higher potential partly to compensate for the diminishing conductance of the medium with time as the concentration of OH^- depletes. Also Ref[39] have shown that not all values of external potential can lead to a smooth surface quality of the etched tungsten electrode. In fact four different regimes are proposed based on the current density vs the applied potential profile as is illustrated in Fig.2.4.

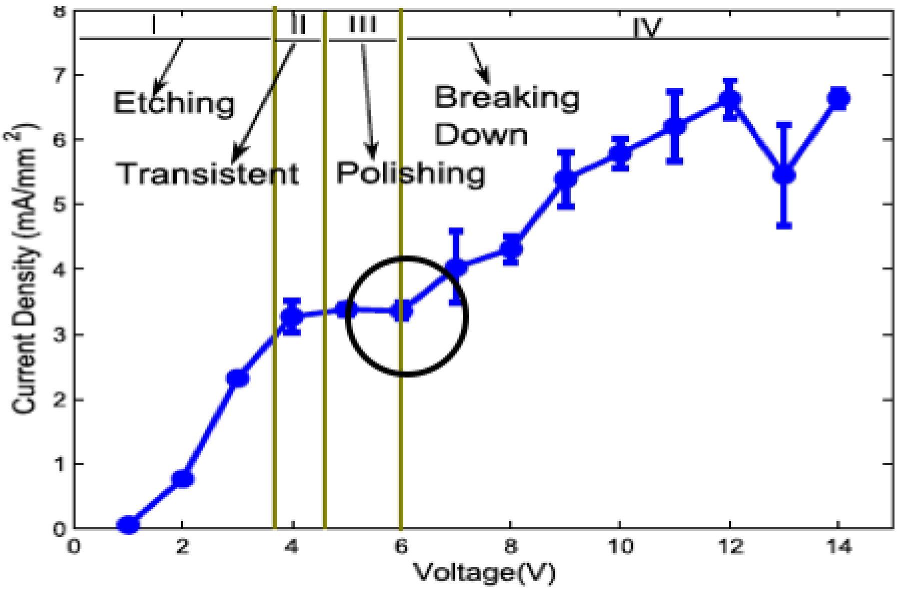

Figure 2.4: The plot of current density (J) versus applied potential (V) for the electropolishing tunsgten (W) showing various regimes. The polishing regime is highlighted within a black oval. The figure is adapted from Ref [39]

In zone I ($\leq$ 4 V), the electrochemical reaction is initiated even though its rate is slow. This is the ohmic regime wherein, current density increases linearly with the applied electric field. In zone II ($\approx$ 4-5 V), the tungstate ions (($WO_4{}^{-2}$) so formed are attracted by the increasing positive charge density at the anode thereby resulting in a passivated electrical double layer. This electrical double layer resists further OH^- from approaching the electrode thereby slowing down the reaction. This effect along with the decreasing OH^- concentration is responsible for lowering of conductance and saturation of current density. In zone IV ($6 \leq V \leq 14$), the reaction becomes turbulent and conductivity and hence current density escalates rapidly due to occurrence of auxillary reactions like

$$2H_2O \rightarrow O_2 + 4H^+ + 4e$$

Reactions such as these also introduces turbulence near the anode which may lead to the appearance of large pits on the final electro-etched tunsgten rod. Moreover we have also seen that for voltages beyond 10 V, there is a direct colloidal breakdown of the electrolyte leading to a white residue. It is thus only zone III ($\approx$ 6V) wherein the passivating layer discussed above saturates and any bulging features on the electrode surface gets dissolved smoothly . It is in this regime where best results for polishing is obtained in terms of surface quality and henceforth we shall continue to set the applied voltage to this value.

2.2.2 Protocol for Electropolishing

The actual experimental set-up used for electropolishing is shown in Fig.2.5. The steps we followed (similar to that in [39])are:

- The purchased rods are ground to size and carefully cut to 35 mm in length. One has to ensure that the rod does not show cracks internally or even splinter during this process
- 700 mL of a 2 M solution of sodium hydroxide (NaOH) is prepared in deionized water and poured in a pyrex container. Since the molar mass of NaOH is 40 gm/mol, one would require 28 gm of NaOH to be dissolved in a solution with total volume 700 mL to achieve the said concentration
- The W rod to be electropolished is held with an alligator clip that is connected to a translation stage
- Using the vertical scale and control of the stage the rod is lowered so as to dip 30 mm of it into the solution. It is important to ensure that the rod is perpendicular to the solution. This completes the anodic assembly
- An alligator clip is used to hold a commercially purchased graphite cathode (around 30-40 mm in length) perpendicular to the solution like the rod. One has to keep the rod and cathode on opposite sides of the dish to prevent turbulence from the cathodic reaction from reaching the rod. This completes the cathodic half cell too.
- The anodic and the cathodic half cells are connected to the DC power supply using cables and banana clips. A multi-meter in series is also inserted into the circuit. The power supply is set to constant voltage mode on 5.8-6 volts DC and one needs to ensure the current density in the solution is 3.5 mA/mm^2 to be in the polishing regime (zone III in Fig.2.4). This can be ascertained by monitoring the current in the multi-meter. Knowing the dimensions of the electrode dipped, current density can thereby be computed.
- The rod is polished for 2-2.5 minutes. This will yield a diameter of 0.45 mm- 0.48 mm (the rods initially are 0.51-0.53 mm).It is important to monitor the time spent during

the electro-etching procedure with a stopwatch as too long would make the rods thinner and unusable and too short a time spent would require multiple iterations to reach a desired diameter and surface quality. The chances of erroneously introducing a surface pit in the latter case would thereby be high.

Using these steps one is able to achieve good surface quality for most of the rods used as is seen in a comparative study in Fig. 2.6.

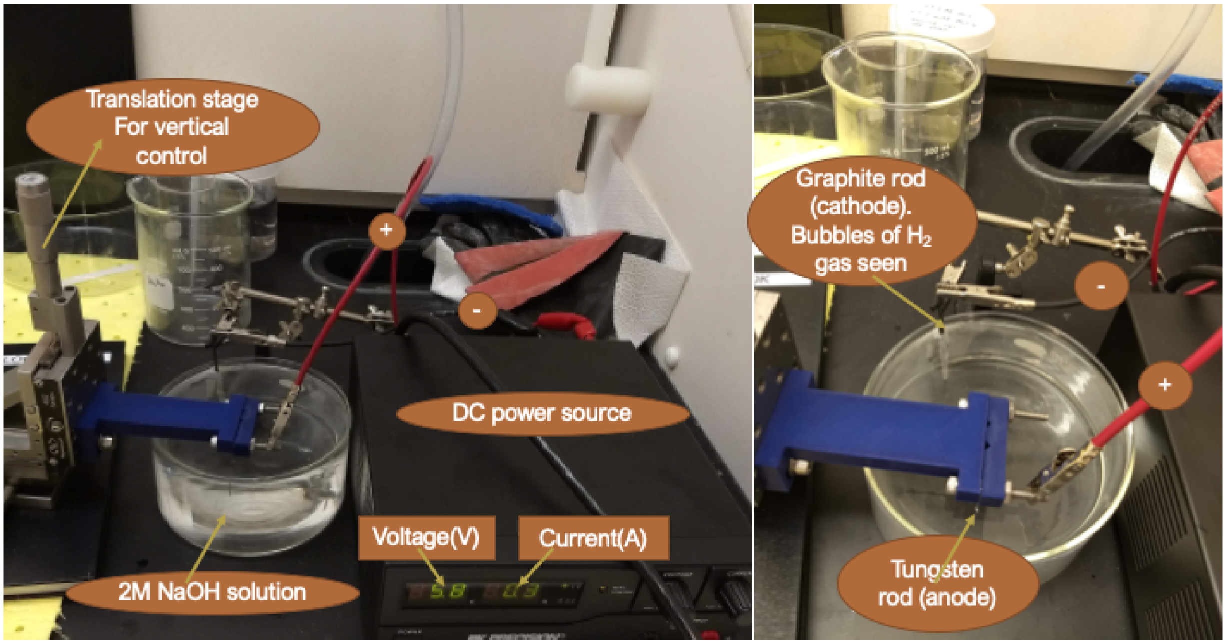

Figure 2.5: The actual setup used during the electropolishing tunsgten (W) electrodes in the laboratory (see text for description)

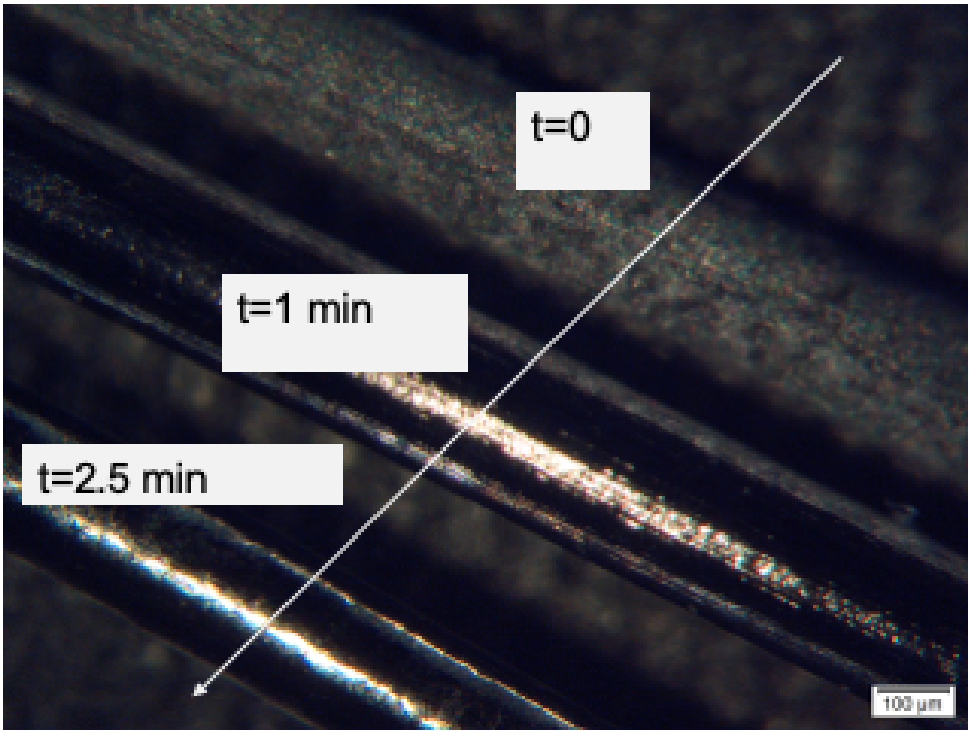

Figure 2.6: Comparison between polished and unpolished rods with time.

2.2.3 Final results

Once the rods are all polished, the unpolished portions were bent to an angle of 45 degrees. This will allow spot welding a constantan flap on the rod for electrical communication. The rods are then stored cleaned in de-ionized water , studied under microscope for imaging of surface quality. The procedure in the previous section is repeated many times before we have 4 compatible rods which are usable as electrodes. These rods thereafter were stored in inert gas (N_2) to prevent oxidative degradation. The picture of the best quadruplet we achieved is shown in Fig. 2.7.

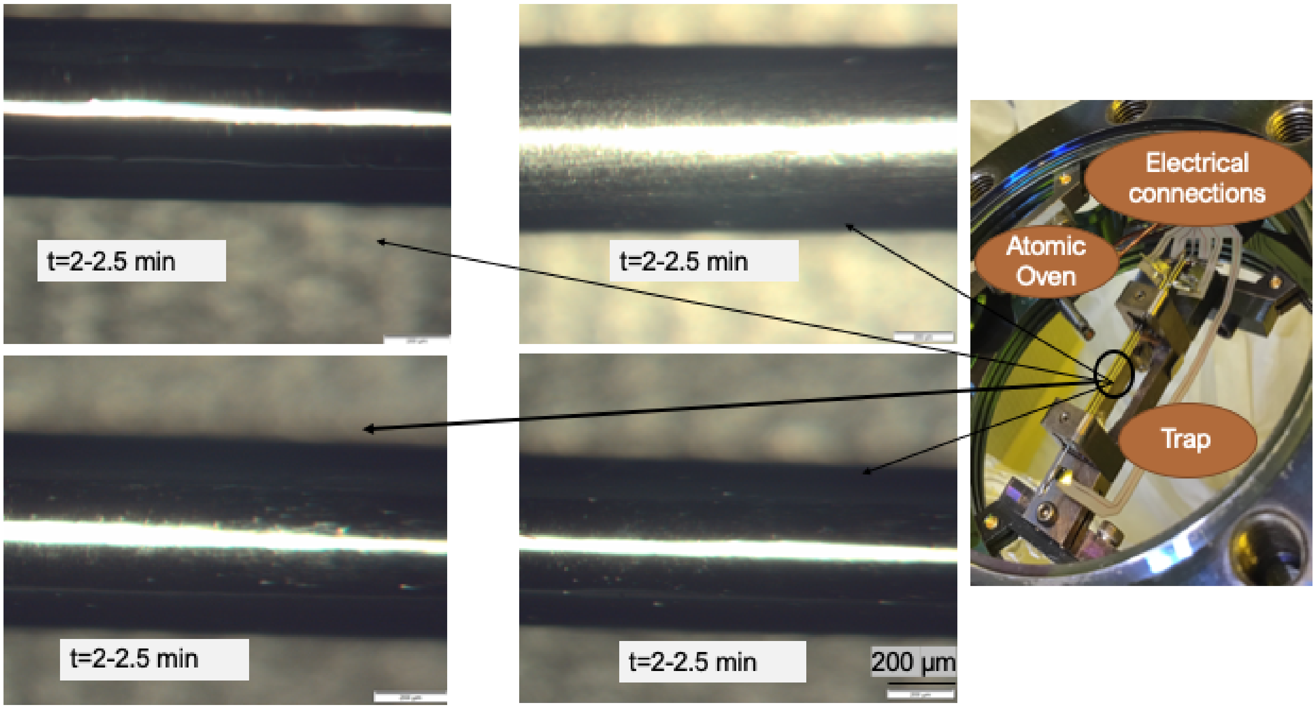

Figure 2.7: Surface quality of polished rods near the central region of the trap after 2-2.5 mins of electropolishing by the procedure mentioned in previous section. The procedure had to be repeated many times until we achieved these 4 compatible rods which were used in the final assembly. We see that all four rods are lustrous and devoid of noticeable surface defects or roughness unlike that in the unpolished case shown in Fig.2.2. The picture on the right shows the location and arrangements of these rods inside the vacuum chamber. The rods are held in place inside the trap holder in holes carved on macor cubes. The central region which is most important to the ions is highlighted by the black oval.

2.2.4 Fabrication of needles

Even though the basic mechanism for the electrochemical etching was described in section 2.2.1, but it might come as a surprise that the same reaction is capable of producing conical shaped tips starting from cylindrical rods if done for appropriate amount of time. This behavior is illustrated schematically in Fig2.8

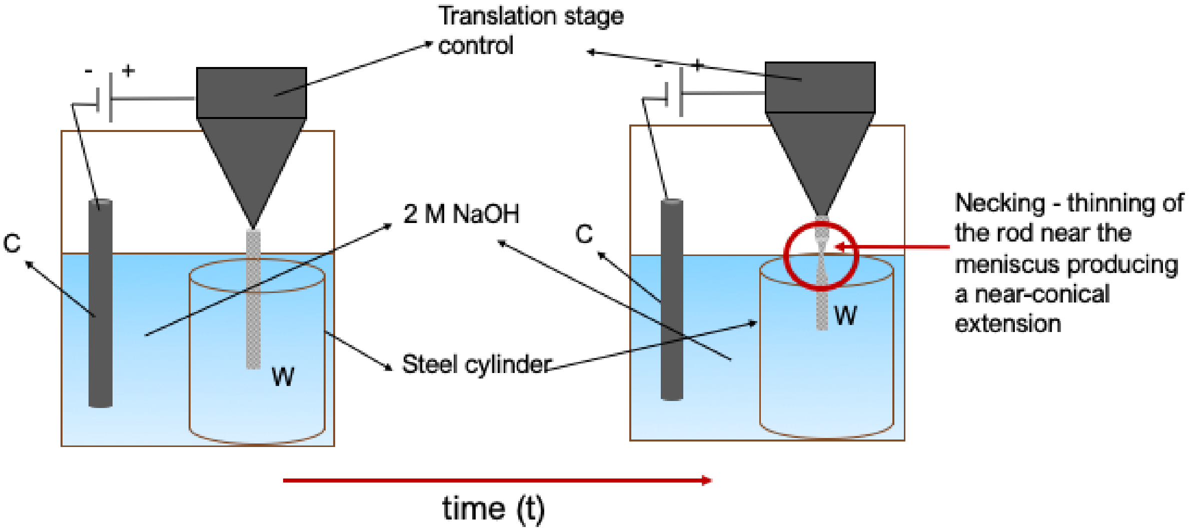

Figure 2.8: The actual setup used during the electropolishing tunsgten (W) electrodes in the laboratory. The electrolytic bath on the right shows a thin, electropolished tungsten rod due to reasons mentioned in previous sections. However, there is enhanced depletion of tungsten layer just below the meniscus of the solution (a phenomenon called necking). If the reaction is allowed to proceed for sufficiently long time, the said region loses the tensile strength to support the mass of the electrode underneath and hence breaks up revealing a conical tip.

We shall thus use this reaction to produce a pair of needle-shaped trapping electrodes for axial confinement (along z-direction) of the ions. The needle tip should be approximately around 20 μm with a conical radial profile of half-cone angle close to 0.058 rad (obtained from simulation). Too sharp a radial profile for the needles (as used in STM tip) is unsuitable for ion-trapping as they may cause arcing due to high-voltages used in these electrodes. Besides, an extremely sharp tip is susceptible to errors due to misalignment and may also be vulnerable to being destroyed by minor accidental bumps during fabrication. We shall see later than the final pair of needles were manufactured using a slightly modified procedure wherein the profile was parabolic as opposed to being conical [40]

2.2.5 Cause of necking

The reason for necking can be ascribed to a complex interplay of surface chemistry, ionic stability and distribution of ions of various species in the electrolytic bath. All the interesting physics happens near the tunsgten electrode i.e. at the anodic half cell and so one shall focus on this exclusively. The key reasons for this behavior can be summarized as

- Firstly its important to appreciate that the meniscus of water near metallic surfaces of d-block elements is concave. This has been ratified using DFT calculations as in Ref [73, 74, 75, 76], which shows how the highest occupied molecular orbitals of a single monomer of water i.e. the lone pair on the oxygen centre interacts with the band of orbitals (predominantly of d-type) near the Fermi-level of the metal. This interaction results in decreased negative charge density at the oxygen (as its the donor) and hence in turn enhances the positive charge density on the hydrogen atoms of the monomer. Once a monolayer is formed through interaction of several such H_2O monomers, the oxygen centre of the next layer of water molecules can now act as hydrogen bond donor to the electron-deficient hydrogen atoms of the first monomer layer. In this way the molecules of water wets the surface and presents an acute contact angle. Presence of electrolyte like OH^- and tungstate ions($WO_4{}^{-2}$) only means that these species can too act as an electron pair donor and interact with the metal in the same way. The presence of positive charge on the metal surface like in this case further facilitates the process due to electrostatic reasons.

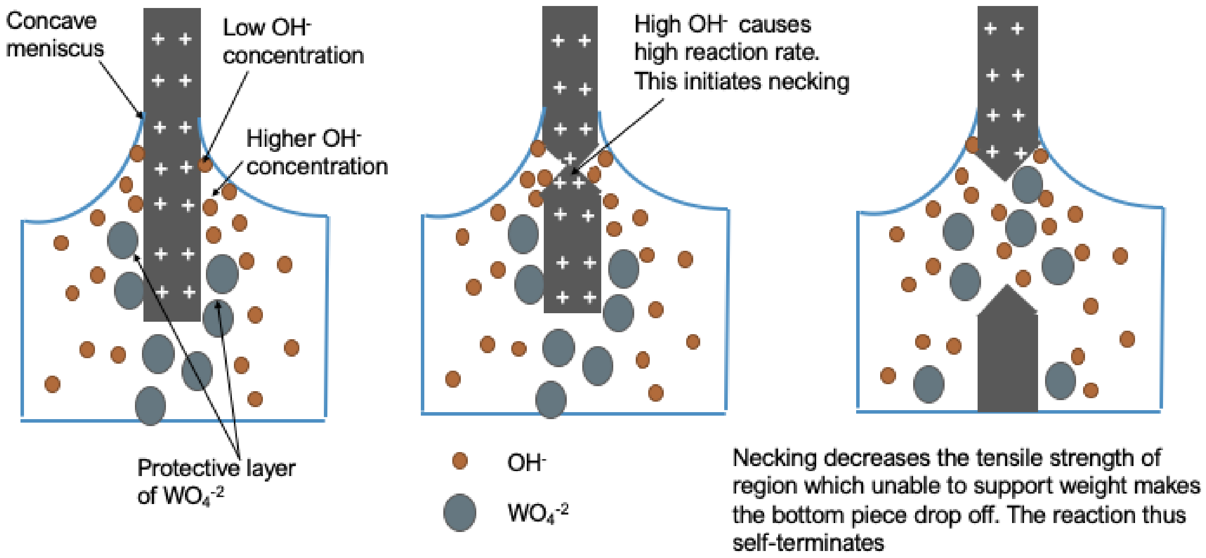

Figure 2.9: Necking scheme for creation of a conical tip(see text). The vertical grey bar shows tungsten electrode(anode)

- Even though OH^- can interact with the metal electrode yet the distribution of OH^- along the electrode surface is not homogeneous[65]. This is explicitly experimentally proven in the work by studying that the Gibbs adsorption isotherm (GAT) for a mixture of KOH/water was negative. Positive value of GAT curves indicates that the solute added prefers to stay at the interface whereas the negative value indicates the solute being repelled from the interface into the bulk. This is due to the fact that ionic electrolytes like OH^- tends to increase surface tension as within the bulk of the solution the ion can be stabilized by ion-dipole interaction. In the meniscus, due to absence of solvent molecules on all sides, the ion does not enjoy uniform interaction and hence the stabilization energy is weak. This means that OH^- will be distributed preferably below the meniscus wherein it enjoys a stronger interaction potential (due to concavity, see above point) compared to at the meniscus.

- One of the reaction by-product is tungstate ion ${WO_4}^{-2}$. These ions are heavy and less mobile than OH^-. In fact Ref [65] reports the properties and the flow kinetics of the concentrated fluid of ${WO_4}^{-2}$ ions obtained from the reaction. They report that the GAT curves for tungstate ion at low concentration is positive, indicating that it can preferrentially be located at the air-water interface. However beyond a certain concentration, as is in this reaction, the value of GAT dips and become negative like that in the case for OH^- ions. The tungstate ions in that case would prefer to be in the bulk. Let us now see why even in the bulk, the distribution of tungstate would not be uniform. Ref[65]reports that the reaction products (predominantly ${WO_4}^{-2}$ ions) emerging from the electrode has an interfacial tension of 0.34 mN/m, a change in density of 28.59 kg/m^3 with respect to the surrounding medium. The viscosity of this jet was also reported to be 0.0018 Pa· s which is higher than that of just alkali and water. These observations indicates that the reaction products would emerge as a jet in the downward direction and would not venture too far away from the tungsten surface due to high viscosity and interfacial tension of the jet. Presence of positive charges on the tungsten anode only makes this effect worse. Thus the distribution of tungstate ions in the bulk would preferentially be along the electrode surface and that too towards the bottom end in the form of an emerging immiscible fluid moving towards the lowermost surface of the container in which the reaction is occurring. This can be contrasted with the distribution of OH^- which like ${WO_4}^{-2}$ also prefers to remain close to the electrode surface (as mentioned in first point , OH^- acts an electron donor to the metal d-orbitals much like solvent water and positive charges on the electrode further aids this). But unlike OH^-, the preferential distribution of ${WO_4}^{-2}$ is towards the bottom half of the electrode as a viscous emerging jet as shown in Fig.2.9

The reaction jet containing ${WO_4}^{-2}$ ions forms a protective double layer around the electrode surface especially towards the bottom half wherein its concentration is high (see third point) as shown in Fig.2.9. Just below the meniscus but much above the lower end of the rod, there is a sweet spot which is not surrounded and passivated by ${WO_4}^{-2}$ and has continuous access to fresh OH^- from the bulk of the solution. Above this region, there is not enough OH^- ions due to concavity of the meniscus (see second and first point) whereas below this region even though there is enough OH^- ions in the bulk to participate in the etching yet they are prevented from reaching the electrode by the passivating layer of emerging ${WO_4}^{-2}$. Whatever OH^- is trapped in this layer between the ${WO_4}^{-2}$ jet and the electrode, that performs the usual etching and are consumed in no time. These ions are not replenished from the bulk as the supply chain is blocked. Thus the reaction in this sweet spot happens at an unaffected rate which is much more than that at the neighboring regions along the electrode surface. This region then starts to thin and develop a neck like feature. After some time when the tensile strength of the region plummets due to its waning thickness, the electrode off breaks revealing a conical tip as shown in Fig.2.9 unable to support the of weight of the portion underneath.

2.2.6 Protocol for making needles

- The purchased rods are cut to size to 35 mm length. One has to ensure that the rod does not show cracks internally or even splinter during this process
- 700 mL of a 2 M solution of sodium hydroxide (NaOH) is prepared in deionized water and poured in a pyrex container. Since the molar mass of NaOH is 40 gm/mol, one would require 28 gm of NaOH to be dissolved in a solution with total volume 700 mL to achieve the said concentration.
- The W rod to be electropolished and converted to needle is held with an alligator clip that is connected to a translation stage.
- Using the vertical scale and control of the stage the rod is lowered so as to dip 3-4 mm of it into the solution. It is important to ensure that the rod is perpendicular to the solution. This completes the anodic assembly
- An alligator clip is used to hold a commercially purchased graphite cathode (around 10 mm in length) perpendicular to the solution like the rod. One has to keep the rod and cathode on opposite sides of the dish to prevent turbulence from the cathodic reaction from reaching the rod. This completes the cathodic half cell too.
- The anodic and the cathodic half cells are connected to the DC power supply using cables and banana clips. A multi-meter in series is also inserted into the circuit. The power supply is set to constant voltage mode on 5.8-6 volts DC and one needs to ensure the current density in the solution is 3.5 mA/mm^2 to be in the polishing regime (zone III in Fig.2.4). This can be ascertained by monitoring the current in the multi-meter. Knowing the dimensions of the electrode dipped, current density can thereby be computed. In case if the desired current density is not reached, one can vary the length of the cathode dipped
- As mentioned before, about 3-4 mm of the rod is dipped at a time. The rod is attached to a stepper motor control which rotates the rod clockwise (or anticlockwise) while electro-etching. A second stepper motor is used to pull the rod out of the solution at a slowest rate possible. This is repeated until satisfactory needle profile is made (around 15 dips for a 5 micron tip).
- Thereafter 12.6 mm of the whole needle obtained in the previous step is dipped and etched for 2 minutes following the protocol for the rods. This will allow us to fit the needle in the macor.

- The needle so formed is cut down to size so that 7 mm extrudes from the trap holder.
- The needles are then stored in inert gas

2.2.7 Final Results

We obtained the first set of needles from this procedure in collaboration with other members of the Quantum Information with Trapped Ions team (henceforth called as QITI group with the principal investigator/supervisor being Dr.K.R.Islam) and also with members of Prof. Senko's lab. Fig.2.10 illustrates the quality of a representative needle so obtained. It should be noted that this is among the best few obtained from this method. Most of the needles obtained in other attempts had not a symmetric profile. The main **problems** with this method are:

- There is no clear directive on the draw rate at which the needles needs to be withdrawn from solution. Faster draw rates usually produce poorer surface quality while slower draw rates produces a very long drop-off time.
- The method is extremely sensitive to the precise alignment of the electrodes in solution. If the tungsten rod is not entirely placed perpendicular to the solution, then the overall profile of the needle so obtained is not symmetric along the cylindrical axis and hence unusable.

This method thus requires multiple runs to get a compatible pair which makes it inconvenient. If the pair of needles used are not similar in geometrical profile then the repulsive electrostatic potential the pair generates need not be symmetric around the midpoint of the axis connecting the tip of the needles. This can tilt the ion chains towards a particular needle even when both needles are biased to the same extent with respect to a common ground. We have even purchased needles from MTS and electro-polished those to improve the surface quality following the protocol for the rods mentioned before and this worked fine. A representative result is shown in Fig.2.11. However, ultimately a co-worker from QITI lab devised a modified version of the needle-making recipe mentioned in previous section. Since we wanted to test the efficacy of this new method, we generated the final pair of needles required for our ion-trap from this recipe. The details of the method can be found in [40] and is being considered for a publication which the author is a part of.

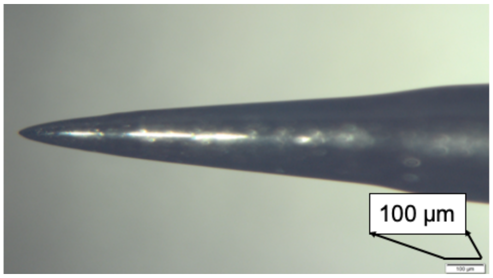

Figure 2.10: One of the best needle tip fabricated from the method in Ref[39]. See text for details.

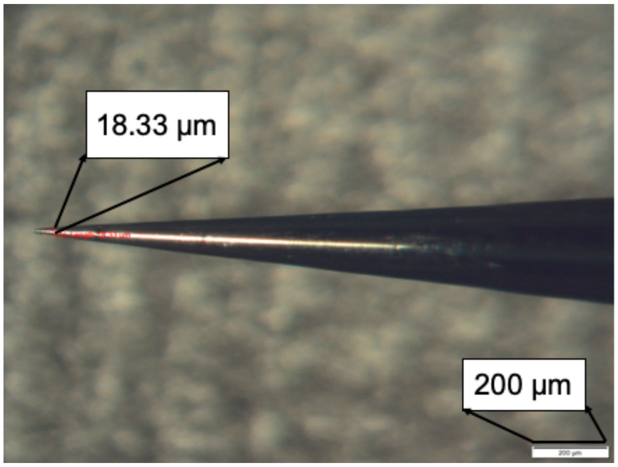

Figure 2.11: Needle tip profile obtained after electropolishing purchased needles from MTS (see text). This procedure worked fine and we could produce a compatible pair. However we wanted to test the efficacy of the new improvised method developed by a co-worker[40] and hence ended up generating the final pair of needles used in our ion-trapping apparatus from this new recipe.

2.3 Conclusion

In this chapter, the author has demonstrated how the actual trap electrodes used in our ion-trapping apparatus were generated. Fig.2.12 shows the electrode system as used in our ion-trap with the respective rods and needle alignments and their corresponding geometrical parameters . In the next chapter the author will show how these electrodes are electrically powered to generate the requisite trapping potential.

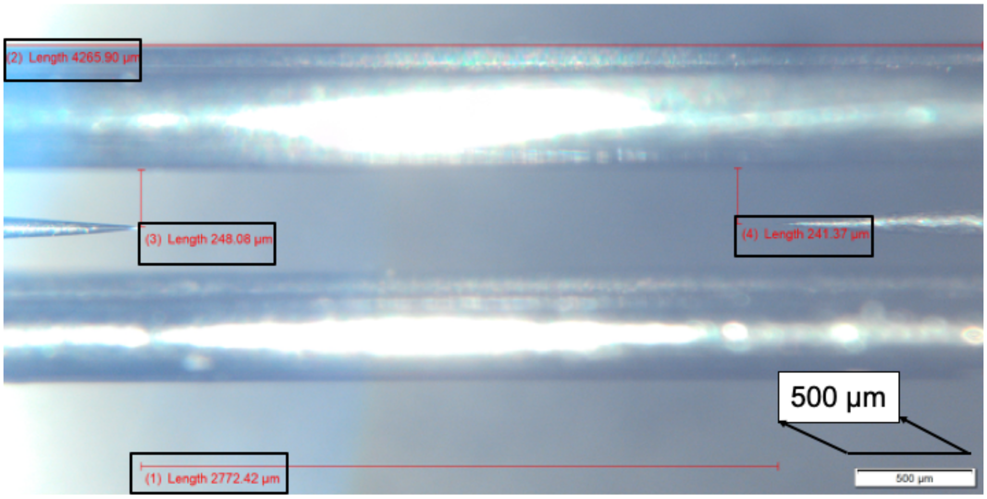

Figure 2.12: The exact alignment and geometrical parameters of the six-electrodes as used in our ion trapping apparatus

Chapter 3

Powering the trapping electrodes- Generation of radio-frequency induced trapping potential

3.1 Chapter at a glance

In the last chapter we studied how the four electrodes were fabricated for our four rod trapping apparatus. The four rods are powered by an oscillating potential generated using RF. The situation for the needles is far more simple and is entirely powered by a positively charged DC electric field source. The surface of the needles thus generates a repulsive potential for positively charged ion like $^{171}\mathrm{Yb}^{+}$ as has been used here thereby confining it towards the centre of the trap. The choice of a dynamically evolving potential for the rods stems from the inability to provide confining potential in 3D using DC electric field[77], a direct consequence of the Maxwell's equations which requires the divergence of electric field vector in a source-free region to be zero. For a dynamically varying field, the potential at each time-step satisfies the Maxwell's relation and the corresponding electric field is divergence free away from the electrode. This essentially means that the ion would still 'see' a confining and an anti-confining axis. However due to the changing polarity of the electrodes, the confining and the anti-confining axis is rapidly switched at a rate higher than the response time of the ion. This effectively creates a confining pondermotive potential[78, 69, 41]. Excellent reviews discussing the basic mechanism for trapping can be found in Ref.[78, 43, 46, 79, 69] and hence is not elaborated herein. We instead focus primarily on the electrical circuitry responsible for generating such a potential. Specifically we shall answer the following questions

- What are the electrical components required to power the rods and needles electrically ? As mentioned above, for powering the needles DC electric field is used which creates a harmonic confinement along the symmetry axis of the needles (z-direction in Fig.2.1). The circuitry for the needles has been designed by one of our collaborator and has been detailed in Ref.[41]. We shall not elaborate it here and henceforth shall just focus entirely on the rods. We shall see that for the rods which requires an AC field, one of the essential component is a helical coil RF resonator. An RF-resonator is essentially a serially connected RLC circuit [80, 81] whose parameters can be tuned to make it a frequency filter and a voltage amplifier. The chapter details the construction of the RF resonator as has been used in our ion-trapping apparatus
- We shall also see simulation results for the potential generated by RF field and a representative trajectory of a trapped ion in that potential.

3.2 Why use an RF resonator?

The reason for using the RF-resonator are the following:

- **Impedance matching** Directly connecting an amplified signal source to the trap electrodes through a transmission line may reflect back a lot of energy to the source port if the impedance of the trap electrodes(which is not usually precisely controlled) is not matched to the characteristic impedance of the transmission line. Having a resonator in between solves this issue. Resonator coil parameters can be tuned to match impedance so as to minimize reflection of power back to the source port. Such reflection if happen can even damage equipments connected in the circuitry powering the resonator.
- **Frequency filter and voltage amplification** As highlighted in the previous section, substantial energy transfer between the source and pick-up coil of a high-finesse (high Q) resonator happens near a particular frequency. As a result output power of the resonator is sensitive to the input frequency. In this respect the resonator acts as a frequency filter and protects the ions from unwanted frequencies. If such frequencies are present they would also titilate the motion of the ion undesirably making it chaotic and even contribute to motional heating[82]. The resonator also acts as a voltage amplifier. If the parameters of the resonator like self-inductance of

the pick-up coil be L, power dissipated be P, the capacitance of the load connected plus the resonator be C and finesse/Q-factor of resonator be Q, then the amplified output voltage after the resonator[81] is

$$V = (\frac{L}{C})^{1/4}\sqrt{P}Q \tag{3.1}$$

- **High slew rate Op-amp** It is hard to find a high-voltage low impedance amplifier for the purpose of voltage amplification on the trap electrodes at this frequency of interest. If Op-amps are used for this purpose, then at the frequency of interest ($\approx$ 20 MHz) the slew rate or switching time of the Op-amp will have to be enormous.

- All of the aforementioned points illustrates simply why an RF-resonator is useful. However we shall specifically design a helical-coil balanced drive RF-resonator. A balanced drive resonator has two open output terminals to be connected to two terminals of a receiving device. An unbalanced drive on the other hand will have one of its terminal grounded. The use of balanced drive is due to the fact that the absolute value of the oscillating potential at each open terminal of the resonator (subsequently at each electrode connected to it) is low for a given difference in potential. This means for a unbalanced drive the entire potential difference (say V) will have to maintained and supplied through one terminal whereas for a balanced drive one can supply $\frac{\pm V}{2}$ across two of the terminals. The reason for using a helical coil resonator is due to the convenient form-factor and also because of the fact that to maximize Q-factor of the resonator for a given resonance frequency, we shall see later (see Eq.3.12) that one has to maximize the self-inductance (L) of the resonator and minimize resistance (R) and capacitance (C). Helical coil resonators have high self-inductances satisfying this criterion.[81].

3.3 Importance and assembly of the source/antenna coil

In this section we will specifically talk about the source/antenna coil which is the primary metallic winding (in this case made of copper, see Fig.3.1) that receives energy input from an external device and relays it onto the pick-up coil of the resonator. A lumped circuit model of the source/antenna coil is given at the bottom of Fig.3.1 following the analysis in Ref.[81]. We will replicate the arguments of Section III A in Ref[81] in this section. In the model we will need the following definitions.

- L_a = self-inductance of antenna coil. Here the identifier 'a' is used to refer to antenna. This coil is referred to as L_1 in Section III A in Ref[81]
- Z_0 = impedance of amplifier/source output
- (L_c)= This refers to self-inductance of the pick-up/receiver coil. Here the identifier 'c' is used to signify the coupled coil. This coil is referred to as L_2 in Section III A in Ref[81].
- Z_L = the impedance of the load/trap connected to the resonator.
- M = the mutual inductance between the antenna and pick-up coil (receiver).

Using these parameters one can write the voltage drop across the antenna-coil (labelled as V_1) and across the pick-up coil (labelled as V_2 which is also voltage drop across the load/trap) as

$$V_1 = i\Omega_{RF}L_aI_1 + i\Omega_{RF}MI_2 \tag{3.2}$$

$$V_2 = i\Omega_{RF}L_cI_2 + i\Omega_{RF}MI_1 \tag{3.3}$$

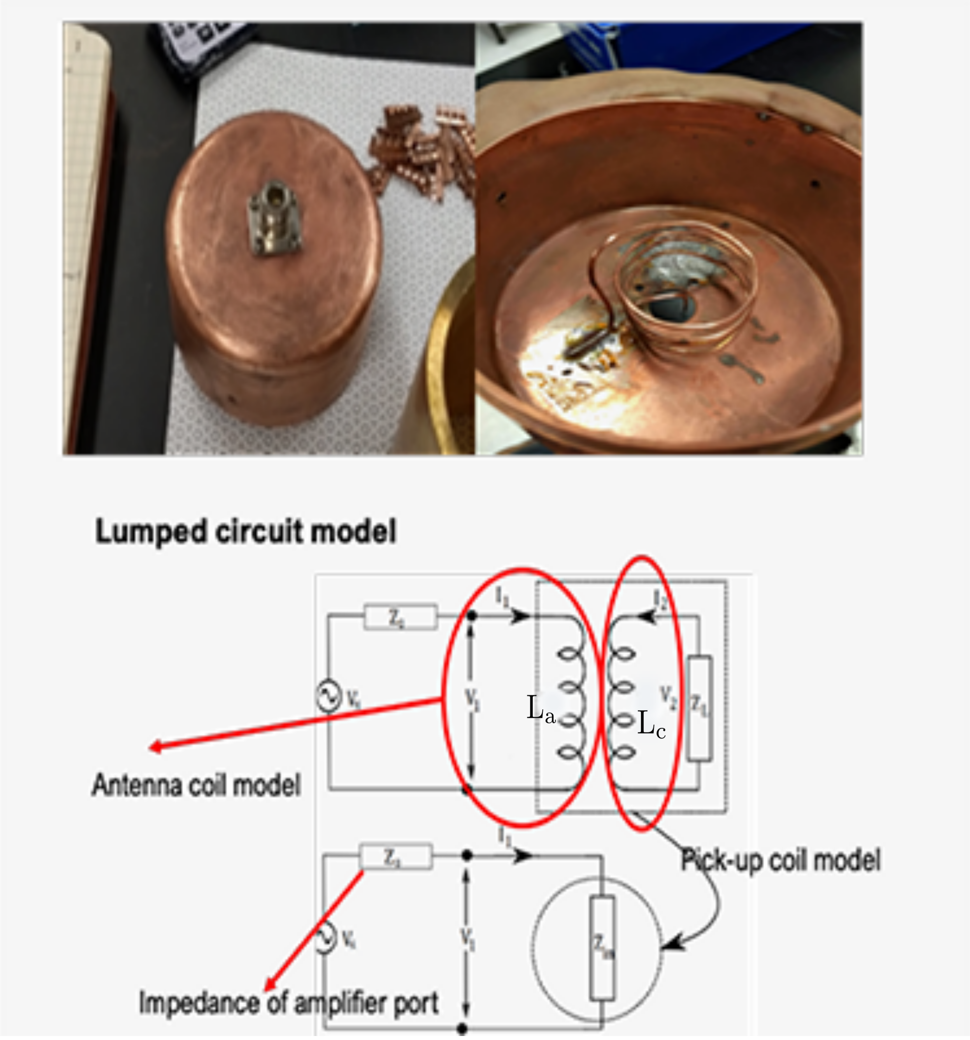

Figure 3.1: The actual pictures of the antenna coil assembled in the lab(top) and the associated lumped circuit model (bottom) adapted from Fig.3 (a) in Ref.[81]. The antenna coil is made from AWG 14 pure Cu wire with 4 windings and a winding diameter of 1 inch. The wire diameter is 0.064 inch (1.6256 mm).

Using the fact that $\mathrm{V_2} = -\mathrm{Z_L I_2}$, it is possible to write $\mathrm{I_2}$ from Eq.3.3 in terms of known parameters as follows:

$$\mathrm{I_2} = -\frac{\mathrm{i\Omega_{RF} M I_1}}{\mathrm{Z_L + i\Omega_{RF} L_c}} \tag{3.4}$$

Using Eq.3.4 in Eq.3.2 and recognizing that $\mathrm{V_1} = \mathrm{I_1 Z_{in}}$ where $\mathrm{Z_{in}}$ is the combined impedance of the resonator (both coils) and the load/trap (see Fig.3.1 we get

$$\mathrm{Z_{in}} = \mathrm{i}\Omega_{\mathrm{RF}}\mathrm{L_a} + \frac{\Omega_{\mathrm{RF}}^2 \mathrm{M}^2}{\mathrm{Z_L} + \mathrm{i}\Omega_{\mathrm{RF}}\mathrm{L_c}} \tag{3.5}$$

To minimize power reflection and afford a proper impedance match one has to ensure $\mathrm{Z_{in}} = \mathrm{Z_0}$ We see Eq.3.5 that for the combined impedance of the resonator + trap/load i.e.$\mathrm{Z_{in}}$ to be equal to external impedance $\mathrm{Z_0}$, one can play with a number of parameters of the antenna and pick-up coil like $\mathrm{L_a}$, $\mathrm{L_c}$, M etc. However we shall see shortly that $\mathrm{L_c}$ affects the resonance frequency of the circuit strongly and also affects $\mathrm{M} = \sqrt{\mathrm{L_c L_a}}\mathrm{k}$. For a fixed choice of resonance frequency, the only available parameter which can be manipulated is thus $\mathrm{L_a}$. $\mathrm{L_a}$ as mentioned before is the self-inductance of the antenna coil. If one simply models the antenna-coil winding as a solenoid, then the self-inductance can be expressed in terms of controllable variables like number of turns of the coil (N), pitch of the coil winding (p) and area of the coil winding (A) as follows

$$\mathrm{L_a} = \frac{\mathrm{A}\mu_0 \mathrm{N}}{\mathrm{p}} \tag{3.6}$$

This parameter set $(\mathrm{N}, \mathrm{A}, \mathrm{p})$ can thus be varied until proper impedance match is achieved (characterized by lowest attainable reflection of input power towards the source). In our case, we noted experimentally through trial and error that N=4, A= 1 inch, AWG-14 pure Cu wire (wire diameter is 0.064 inch (1.6256 mm)) can lead to good impedance matching reflecting about -40 dBm of input power. One end of the coil is soldered to the circular Cu base (as shown in Fig.3.1). The coil receives input RF power from the source/amplifier through an N-type connector.

3.4 Importance and assembly of the pick-up/receiver coil

In this section we will specifically talk about the pick-up/receiver coil which is the secondary metallic winding (in this case made of copper, see Fig.3.2) that receives energy through time-varying magnetic flux that couples it to the antenna coil inductively. This in turn generates an EMF which powers the rods. This is the most important component of the resonator as it controls the resonance frequency (henceforth referred to as Ω_{RF}^0) and also largely the finesse of the resonator. Fig.3.2 also displays the the lumped circuit model of this coil with the trap as load as adapted from Fig. 6 (a), (b), (c) in Ref[81]. We will replicate the arguments of Section III B in Ref[81] and adopt the following naming convention following the said reference.

- $\mathrm{L_a}$ = self-inductance of antenna coil as labelled before. Here the identifier 'a' is used to refer to antenna.
- $\mathrm{Z_0}$ = impedance of amplifier/source output
- ($\mathrm{R_c}$, $\mathrm{L_c}$, $\mathrm{C_c}$)- This triplet refers to resistance, self-inductance and capacitance of the pick-up/receiver coil respectively. $\mathrm{L_c}$ was named and used in the previous section. Here the identifier 'c' is used following the convention in Ref.[81] which names it the coupled coil.
- ($\mathrm{R_s}$, $\mathrm{C_s}$) - This doublet corresponds to the resistance and capacitance of the enclosing shield. The identifier 's' signifies shield.
- ($\mathrm{R_t}$, $\mathrm{C_t}$)- This doublet corresponds to the resistance and capacitance of the trap/load. The identifier 't' signifies trap.
- $\mathrm{R_j}$ is coil to shield resistance
- $\mathrm{C_w}$ is connecting wire capacitance

Following Ref.[81], we can now club together the various impedance terms defined above into two subgroups $\mathrm{Z_E}$, $\mathrm{Z_{coil}}$.

- $\mathrm{Z_{coil}}$ - This subgroup consists of $\mathrm{Z_M}$ (see Fig.3.2) connected in series to resistance $\mathrm{R_c}$ and the two together connected in parallel to $\mathrm{C_c}$. As seen in Fig.3.2, $\mathrm{Z_M}$ is the effective impedance due to the antenna-coil self-inductance ($i\Omega_{RF}L_a$), the impedance of amplifier/source input ($\mathrm{Z_0}$), impedance due to the self-inductance of the receiver coil ($i\Omega_{RF}L_c$) and the mutual inductance between the source and the pick-up coil. Using the same reasoning as enlisted in the source-coil section and in Ref.[81] we can arrive at the following expressions

$$\mathrm{Z_M} = i\Omega_{RF}\mathrm{L_c} - \frac{\Omega_{\mathrm{RF}}^2\mathrm{M}^2}{-\mathrm{Z_0} + \mathrm{i}\Omega_{\mathrm{RF}}\mathrm{L_a}} \tag{3.7}$$

$$\mathrm{Z_{coil}}^{-1} = \frac{1}{\mathrm{R_c} + \mathrm{Z_M}} - \frac{i}{\Omega_{RF}\mathrm{C_c}} \tag{3.8}$$

- $\mathrm{Z_E}$ - This is the effective impedance due to serially connected load capacitance ($\frac{-i}{\Omega_{RF}C_t}$) and load resistance ($R_t$), impedance due to parallel connected shield capacitance + wire capacitance which are mutually serially connected as in Fig.3.2 ($\frac{-i}{\Omega_{RF}(\mathrm{C_s}+\mathrm{C_w})}$). The overall impedance associated with $\mathrm{Z_E}$ subgroup is thus

$$\mathrm{Z_E}^{-1} = \frac{1}{\mathrm{R_t} + \frac{-\mathrm{i}}{\Omega_{\mathrm{RF}}\mathrm{C_t}}} + \frac{1}{-\frac{i}{\Omega_{RF}\mathrm{C_w}}} + \frac{1}{-\frac{i}{\Omega_{RF}\mathrm{C_s}}} \tag{3.9}$$

With the two definitions above the lumped-circuit model simplifies considerably and the equivalent circuit is basically due to the serial connection of $\mathrm{Z_E}$, $\mathrm{Z_{coil}}$, $\mathrm{R_j}$, $\mathrm{R_s}$ as shown in the bottom most panel of Fig.3.2. We see that the entire circuit is thus a simple RLC (the L and C part is present within $\mathrm{Z_E}$, $\mathrm{Z_{coil}}$). The resonance frequency of the circuit can be obtained from the condition below

$$\mathrm{Im}(\mathrm{Z_{coil}} + \mathrm{Z_E} + \mathrm{R_j} + \mathrm{R_s}) = 0 \tag{3.10}$$

Using Eq.3.10, Eq.3.9, Eq.3.8 and properties of RLC series circuit, we arrive at the following expression for the resonance frequency (Ω^0_{RF}) and Q-factor

$$\Omega^0_{RF} = \frac{1}{(\mathrm{L_c}(\mathrm{C_c} + \mathrm{C_s} + \mathrm{C_t} + \mathrm{C_w}))^{1/2}} \tag{3.11}$$

$$\mathrm{Q} = \frac{\Omega^0_{RF}\mathrm{L_c}}{R_{eff}} \tag{3.12}$$

where $\mathrm{R_{eff}}$ is defined as [81]

$$\mathrm{R_{eff}} = \mathrm{R_j} + \mathrm{R_c} + \mathrm{R_s} + \mathrm{R_t}\frac{\mathrm{a}^2}{(\mathrm{a}+1)^2} \tag{3.13}$$

$$\mathrm{a} = \frac{\mathrm{C_t}}{\mathrm{C_s} + \mathrm{C_w}} \tag{3.14}$$

In obtaining the above equation Eq.3.13 one has to use the condition for the helical coil resonator which requires the equivalent impedance of the resonator to be dominant in inductance (See Ref[81]). We thus see that the properties of this coil influences of the resonance frequency and Q-factor heavily. The construction of the coil was made following the empirical conditions enlisted down in Ref[80, 41]. We used N(no.of winding turns) = 14, diameter of the enclosing shield (D) = 88 mm, and pitch (spacing between coil winding) = 4.87 mm. As pointed out in Ref.[80], the diameter of the solenoidal core (say $\mathrm{d_0}$) will be chosen according to the diameter of the enclosing shield (D) such that $\frac{d_0}{D}$ =

0.55. Following this equation d_0 is chosen to be 48.4 mm. The coil chosen was pure AWG 12 Cu wire(diameter of wire = 2.05 mm). The coil is wound around a 3D printed PLA support structure as seen in Fig.3.2. The red coil support rings towards the terminal ends facilitates the easy mounting of the coil inside the shield.

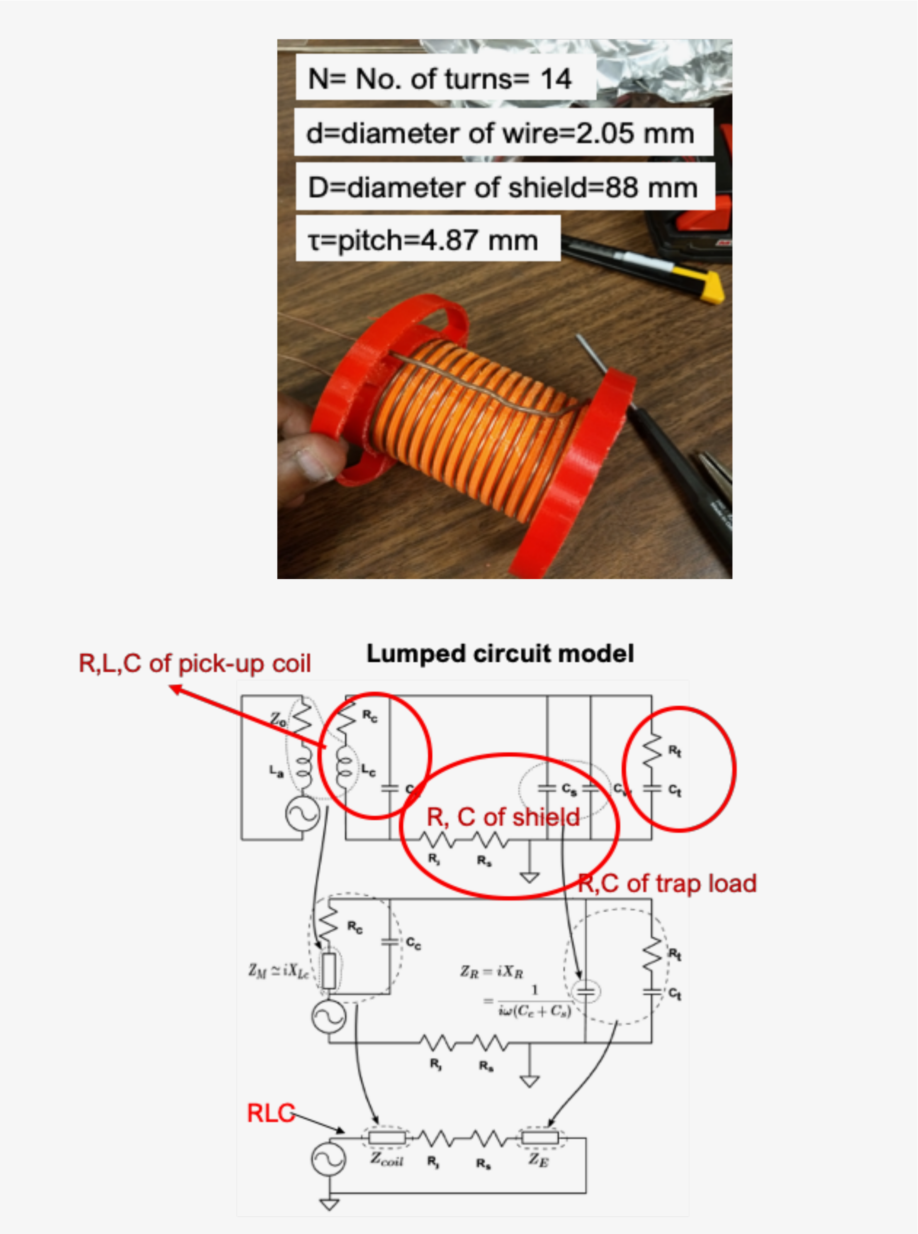

Figure 3.2: The actual pictures of the receiver/pick-up coil assembled in the lab(top) and the associated lumped circuit model (bottom) adapted from Ref.[81]. The parameters used in the construction of the coil are enlisted. The diameter of the solenoid is 48.4 mm and is chosen according to the diameter to the enclosing shield following [80]. The coil is wound around a 3D printed PLA core (orange). The red support rings helps to mount the coil within the shield.

3.5 Final Construction

- The antenna coil is assembled first. It is made from AWG 14 pure Cu wire (wire diameter 1.6256 mm) with N=4 windings and a winding diameter of 1 inch. The winding is done around a Thorlabs lens tube. One end of the coil is then soldered to an N-type connector cap (see Fig.3.1) attached to a Cu base. The outer edges of the Cu base was gold plated prior to that to prevent oxidative degradation. The other end is soldered to the Cu base directly as seen in Fig.3.1 and Fig.3.3 (b)

- The receiver/pick-up coil is assembled next. It is wound around a 3D printed PLA support core (orange) as shown in Fig.3.2. The coil is wound using N=14 turns with a AWG 12 Cu wire (wire diameter is 2.05 mm) with a pitch of 4.87 mm. The diameter of the 3D printed solenoidal core was chosen as 48.4 mm [80, 41].Also see Fig.3.3 (c)

- The red support rings at the terminal ends of the receiver coil are placed as seen in Fig.3.2 and Fig.3.3 (c)

- A Cu shield with a base diameter of 88 mm is gold-plated. This reduces oxidative degradation. See Fig.3.3 (d)

- The gold-plated Cu shield is placed on the circular Cu base containing the source coil. Copper fingerstocks are placed on the rims of the Cu base to ensure better electrical contact between the base and the shield. The pick-up coil with the ring supports are placed inside the shield maintaining a gap of 22 mm from the top open end of the shield. See Fig.3.3 (e). The copper fingerstocks used for this circular base are gold plated.

- Another circular Cu base with perforations to allow the wires the RF of the unbalanced drive to reach the trap is attached to the open end of the Cu shield. Copper fingerstocks placed on the rims of Cu base are used herein as well for good electrical communication. See Fig.3.3 (a). This circular base with the copper fingerstocks are gold plated.

- The resonator so assembled is tested for high impedance matching (low power reflection). If highest desirable impedance match is not attained, one can open the Cu base for the source coil and change the pitch of the coil or can enhance the mutual inductance between the source and pick-up coil by changing the separation between the two manually. The final resonator so obtained is soldered to the trap as seen in Fig.3.3 (f)

As mentioned in the above points, the shield, the circular base containing the perforations for the output terminals of the resonator and the fingerstocks for electrical contact were the only components that were gold-plated. There is nothing special about these components at all. Technically it would help if all the components (both the Cu bases and their respective fingerstocks, the coil wires for both the antenna and receiver coil, the Cu shield) were all electroplated as being Cu based they are all susceptible to oxidation. However the selective choice in components has to do with historical reasons as certain components (those not electro-plated) were already assembled by the time an in-house gold-plating facility was developed as a resource.

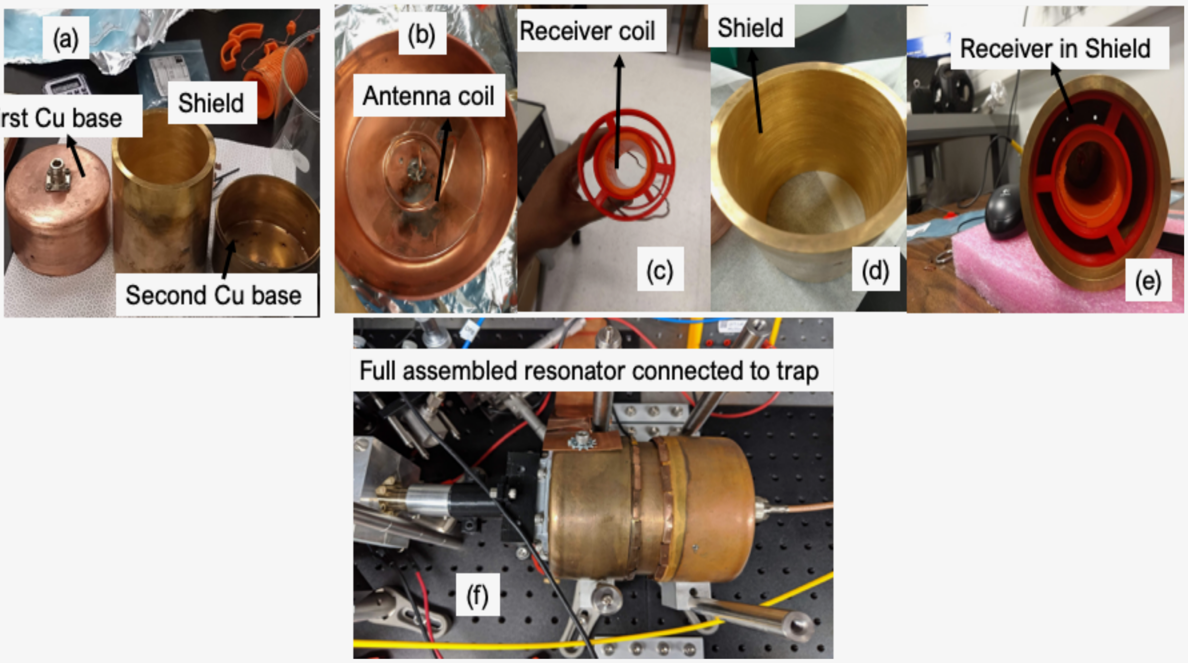

Figure 3.3: Pictures during the construction of the actual resonator used in our ion-trapping apparatus.(a) Pictures of the primary resonator metallic cases- the two Cu bases and one Cu shield. (b) The antenna coil soldered to the first Cu base. (c) The receiver coil around PLA core (orange) with red support rings (d) The gold-plated shield (e) The receiver coil unit inside the shield (f) The full resonator connected to the ion trap. The three Cu cases were gold-plated especially towards the rim and the outer-surface. This is done to establish good electrical contact with the fingerstocks and prevent rapid oxidative degradation.

3.6 Circuitry powering the resonator

The primary components responsible for providing the RF frequency to the resonator (see schematic in Fig.3.4)are as follows:

- A RF frequency generator/source- We use Rigol DG4102 (see Fig.3.6). We use the source to deliver an oscillating potential near the required resonance frequency ($\approx$ 20 MHz) at 16 dBm of input power and DC offset of 0 V. The choice of 16 dBm of input power is motivated by the need to set the peak voltages at the rods to near 200 V as elaborated in Ref.[41]. We shall see in the next section that the Q-factor and hence the voltage amplification factor for our trap is lower than the corresponding one in Ref.[41]. This would require us to use a higher input power to set the same voltage (the remaining parameters of our trap like its capacitance is 4-5 pF and the self-inductance of the resonator to be 12 μH are expected to be similar to Ref.[41] as predicted by simulation. However to prevent accidental damage due to electrical breakdown we continue to operate the trap at this input power. The output from the source is connected to -40 dBm attenuation ((-10 dBm) + (-30 dBm)).

- The source port provides the oscillating potential near the requisite frequency at a nett power of -26 dBm (16 dBm - 40 dBm). The signal is first amplified by an RF amplifier. Initially we were using Mini-Circuits ZHL-5W-1+ which has a 1 dB compression point (henceforth denoted as P1) = 37 dBm and a gain of 45 dB. However the amplifier generates a lot of heat. It was replaced later by LNA 700 from RF Bay. This new amplifier works in the frequency range 10-700 MHz, has a gain of 45 dB, P1 at 27 dBm. These stats are perfect for our requirements. The amplifier requires a DC voltage of 5V and draws nearly 180 mA. The Fig.3.6 shows the amplifier. Due to the attenuators in the source port mentioned in previous point, after the amplifier amplifies the signal the nett gain is 5 dB from the unattenuated input signal at 16 dBm. Such extreme attenuation followed by amplification is used so as to prevent accidental damage to the trap. This is ensured by the fact that for the operational frequency of our trap/resonance frequency of our resonator is 20.28 MHz. For this frequency the source DG4102 can output a sine wave of maximum amplitude of 18 dBm (5 Vpp). So we park the operating power of the signal generator to 16 dBm close to its maximum power . This way an experimenter would not be able to inadvertently increase the power of the signal at the input by a lot to cause a damage to any electrical component internal to the trap. The signal is then reduced in strength (using fixed attenuators) before further amplification. Unless these attenuators are removed from the circuitry which is a rare event any way, chances of excess electrical damage due to enhancement in electrical power at the source is thus mitigated. Well this also means that with our current circuitry the maximum power we can deliver is 23 dBm (18 dBm + 5 dBm). If this is insufficient for a specific application, we have the option of making a deliberate choice of removing the attenuators or using a better more powerful signal source (or amplifier with enhanced gain).

- The amplifier sends the signal into the in-coupling port of a bi-directional coupler Mini-Circuits ZFBDC20-61HP+ (see Fig.3.6). The transmitted port of the bi-directional coupler is connected to the resonator directly. The reflection port associated with this transmitted port is connected to a spectrum analyzer (after -20 dB attenuation) to sample the reflected power and check for resonance. The spectrum analyzer used for the purpose is from Rigol DSA832.
- The resonator is grounded to our optical table using a copper strip.

Using the above setup with an input power of 16 dBm from the RF frequency generator at frequency of 20.286 MHz and the amplifier LNA-700, we were able to generate secular frequencies in the radial direction (x and y) of $\sim 2\pi \times 0.4 - 0.43$ MHz. At this point we have not introduced what secular frequencies are, so we will reserve further discussion for a later section (Section 3.9.3). The said radial frequency was later modified to $\sim 2\pi \times 1.3$ MHz by using the maximum power from the RF source and amplifier ZHL-5W1+ with few attenuators removed.

3.7 Circuitry powering trap after the resonator

For the circuitry powering the trap after the resonator onwards we solder the two copper terminals of the balanced resonator to electrical feedthroughs in the vacuum chamber. This electrical feedthrough therefater powers a flexible printed circuit board (FPCB) which in turn provides the RF field and DC field to the rods and needles. For details see Section 3.3 in Ref.[41].

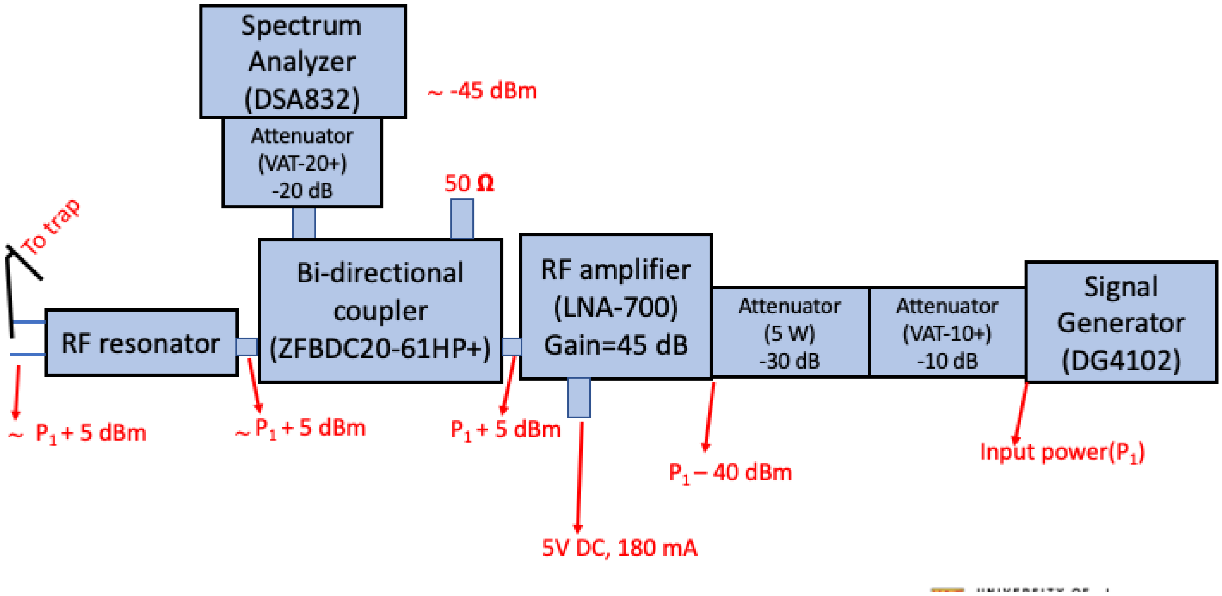

Figure 3.4: The scheme of the circuitry providing the RF field to the resonator. The Signal source (DG4102) provides an oscillating voltage at the frequency of interest of power P_1 in dBm. The power of this signal is then traced across all components of the circuitry. For our current operation the signal strength $\mathrm{P}_1 = 16$ dBm and the input frequency = resonance frequency of resonator $(\Omega^0_{\mathrm{RF}}) = 20.28$ MHz which resulted in a secular frequency along the radial directions (x and y) to be $\sim 2\pi \times 0.4 - 0.43$ MHz. The said frequency was modified to $\sim 2\pi \times 1.3$ MHz by further increase in RF power at the source. Since we have not discussed or defined secular frequencies so far, further elaboration about its generation is reserved for Section 3.9.3 and figures therein.

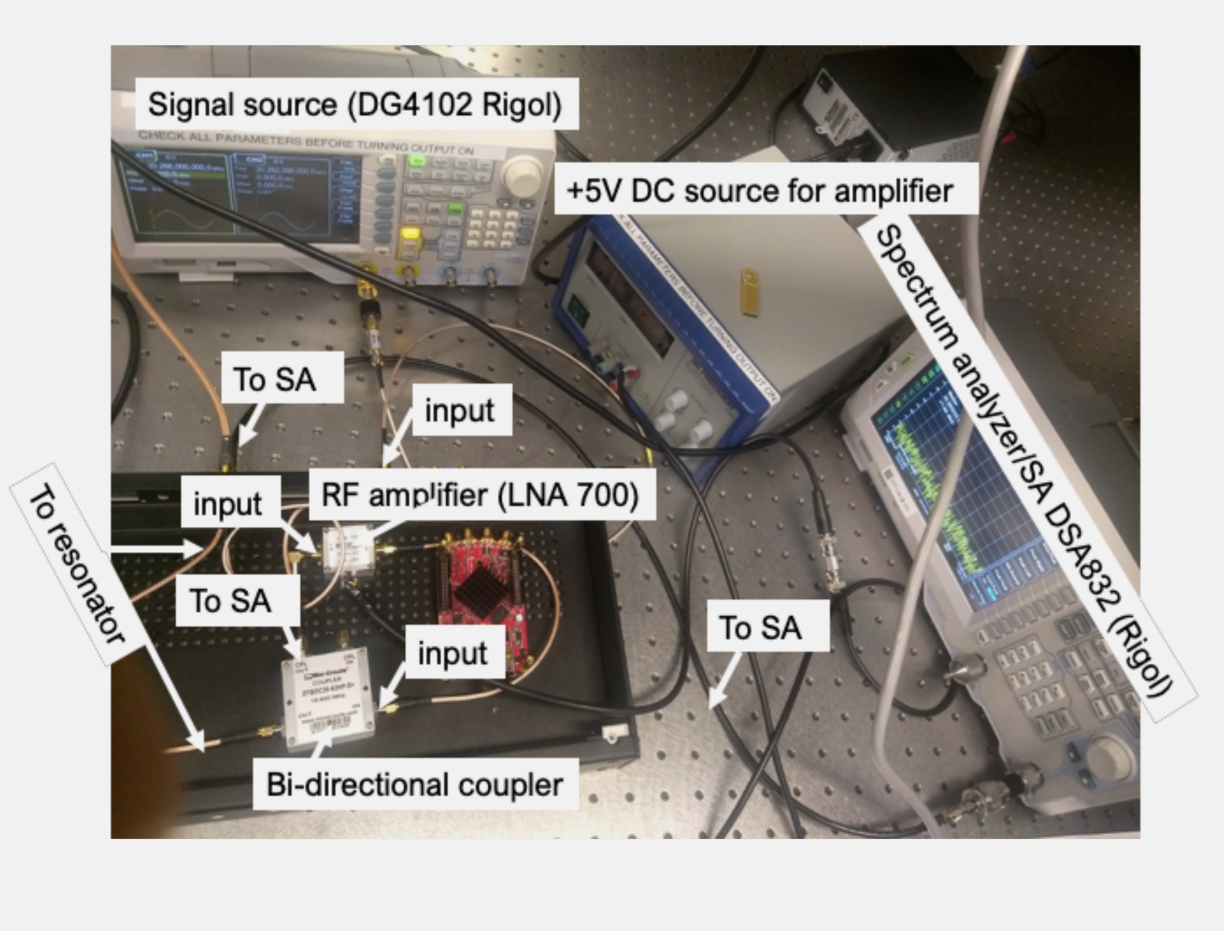

Figure 3.5: The circuitry providing the RF field to the resonator. The Signal source (DG4102) provides an oscillating voltage at the frequency of interest which is fed into the amplifier (LNA 700). From the amplifier the signal is fed into a bi-directional coupler. Transmitted port of the bi-directional coupler feeds directly into the resonator. The reflection port samples the energy reflected and sends it to the Spectrum analyzer (DSA832). See text for more details

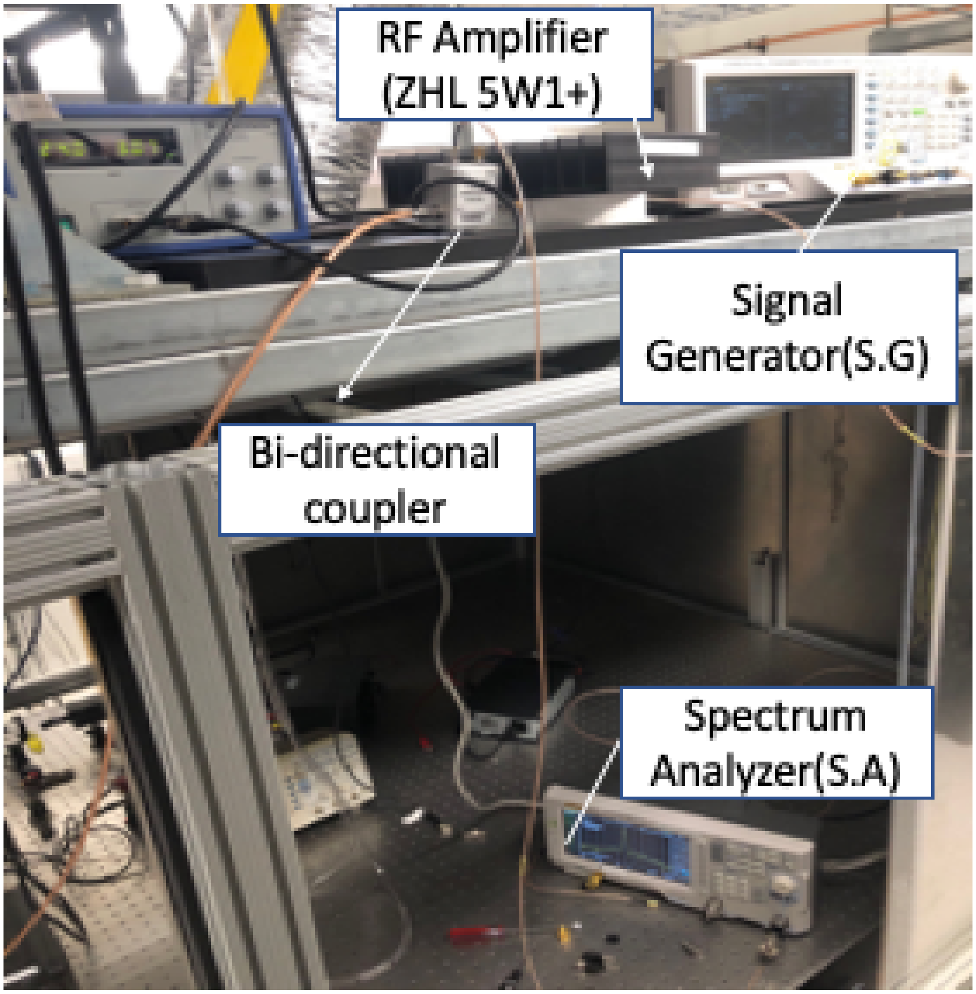

Figure 3.6: The circuitry providing the RF field to the resonator. The Signal source (DG4102) provides an oscillating voltage at the frequency of interest which is fed into the amplifier (ZHL5W1+). From the amplifier the signal is fed into a bi-directional coupler. Transmitted port of the bi-directional coupler feeds directly into the resonator. The reflection port samples the energy reflected and sends it to the Spectrum analyzer (DSA832). See text for more details

3.8 Properties of the resonator

The resonance frequency and the associated Q-factor of the resonator was measured using VNA (Rohde and Schwarz 9 kHz - 4 GHz ZVR) in a linear scale. The results are in Fig.3.8

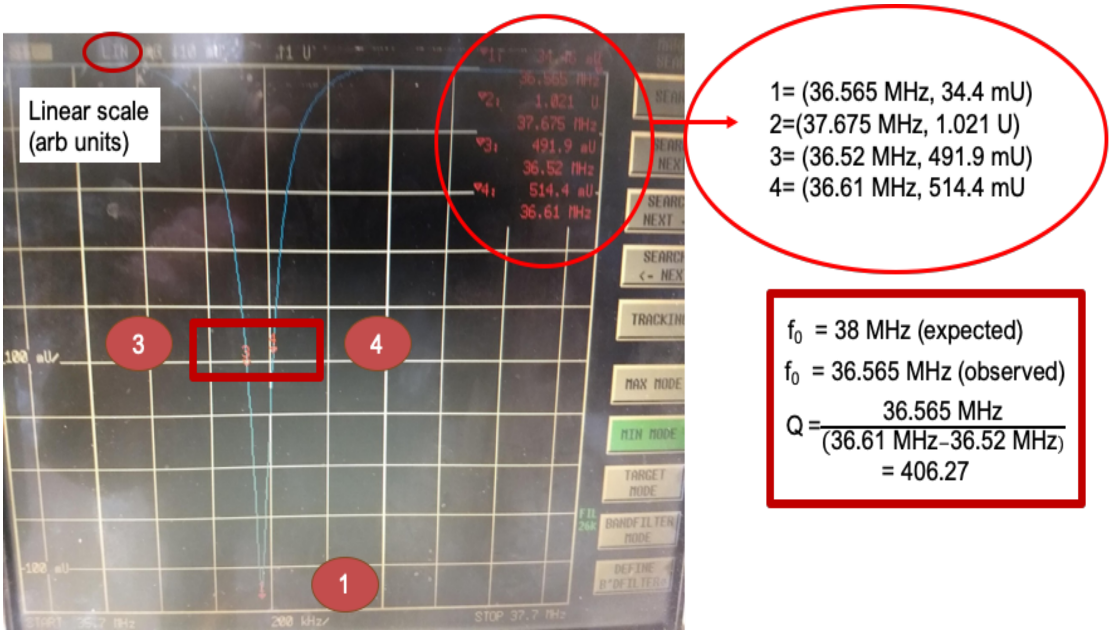

1= (36.565 MHz, 34.4 mU)
2=(37.675 MHz, 1.021 U)
3= (36.52 MHz, 491.9 mU)
4= (36.61 MHz, 514.4 mU

f_0 = 38 MHz (expected)
f_0 = 36.565 MHz (observed)

$$Q = \frac{36.565 \text{ MHz}}{(36.61 \text{ MHz} - 36.52 \text{ MHz})} = 406.27$$

Figure 3.7: The plot of the reflected signal from the resonator constructed under unloaded conditions as a function of input frequency in VNA (Rohde and Schwarz 9 kHz-4 GHz ZVR) in linear scale. Several markers are placed to identify important points in frequency space. Marker 1 identifies the resonance frequency at minimum reflection which is 36.565 MHz. The slightly lesser frequency than expected is probably due to the additional capacitance introduced by the PLA core and support rings in congruence with Eq.3.11. Marker 3 and 4 identifies frequency the point at half of the minimum reflection. Using these the Q factor computed is 406.27

The same resonator when connected to the actual trap as in Fig.3.3(f) and the resonance frequency is measured using Rigol Spectrum Analyzer DSA832 (9 kHZ - 3.2 GHz) the resonance frequency is found to be 20.283 MHz and the corresponding Q factor is 150. The drop in resonance frequency can be explained using the additional capacitance of the trap of about 4-5 pF [41]. But the Q-factor suffers not only due to additional trap capacitance but also due to resistive junctions created when the resonator is soldered to the trap.

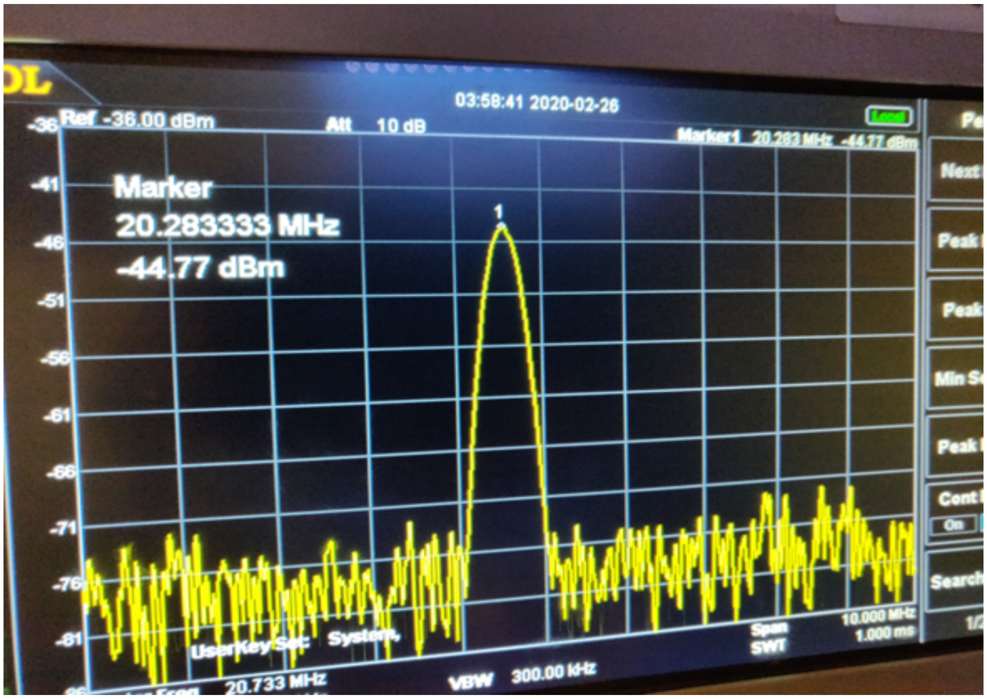

Figure 3.8: The same resonator as in Fig.3.8 connected to the actual trap as load as in Fig.3.3(f). Its resonance frequency and associated Q-factor is measured using Rigol Spectrum Analyzer DSA832 (9 kHZ - 3.2 GHz). The resonance frequency is found to be 20.283 MHz due to additional capacitance due to the trap (estimated to be 4-5 pF in Ref[41]).The drop in Q-factor to 150 is not only due to the trap capacitance but also due to the resistance introduced into the circuit due to soldered joints of the resonator with the trap.

3.9 What kind of potential is generated at the electrodes?

In this section we shall study the simulation results conducted by the author for studying the trajectory and the trapping mechanism for an ion in a trap made from four-rods and two needles as described in the last chapter.

3.9.1 Potential due to the rods

For the four-rods we use an alternating potential with a frequency of 20.2 MHz. The generation of this frequency and the role played by the RF resonator and other components of the RF circuitry to to relay this frequency to the trapping electrodes have already been discussed in the previous sections of this chapter. Herein we shall only focus on how this frequency is responsible for trapping the ion and show simulation results verifying the claim. Before we start let us recall the co-ordinate system that we are going to use for our discussion. It is elaborated in Fig.3.9

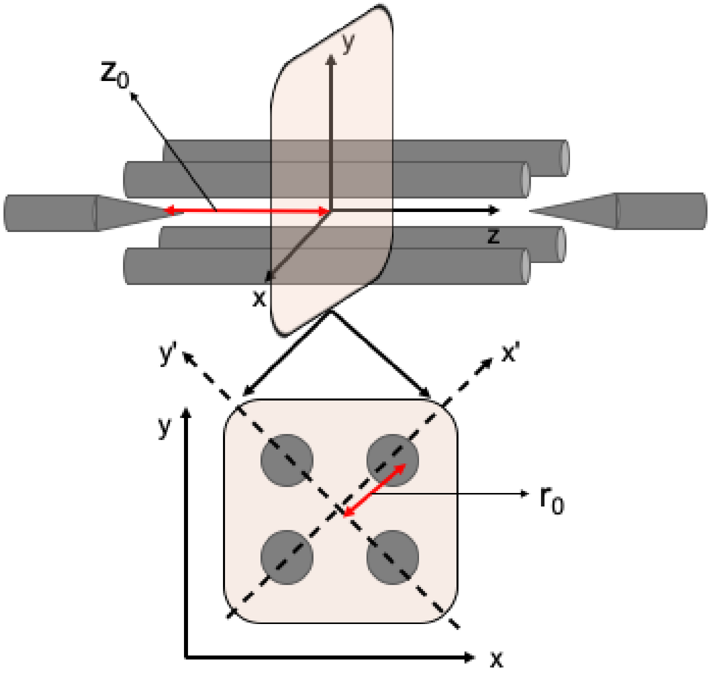

Figure 3.9: The co-ordinate frame of the 4 rods and 2 needles to be used for discussing the simulation results. The length scales r_0 and z_0 are marked.

The rods are powered by oscillating RF frequency with an amplitude of V_0 with a frequency of Ω^0_{RF}. The accompanying potential at a given time instant is of the form:

$$V_{\mathrm{rods}}(x', y', z, t) = V_0 \kappa \mathrm{Cos}(\Omega^0_{\mathrm{RF}} \mathrm{t})(\frac{\mathrm{x}'^2 - \mathrm{y}'^2}{\mathrm{r}_0^2}) \tag{3.15}$$

The quantity κ is known as structure factor and accounts for deviations of the actual rod geometry from hyperbolic rod geometry. Note to satisfy Maxwell's equation the potential is anti-confining in one of the two directions (shown along y' here). To understand the mathematical reasons as to why this leads to trapping conditions one can Ref[41]. But let us go over the physical picture. The sinusoidal time dependance switches the polarity of x' and y' at the resonance frequency of RF resonator Ω^0_{RF}. At a given time when the ion feels the confining potential along the direction x' it also feels the anti-confining potential of the direction y' and tends to roll off in that direction. If this switching between the confining and the anti-confining direction happens at a rate faster than the response time of the ion, then the ion effectively experiences an average potential which is confining. This is known as the pondermotive pseudopotential[78, 43, 46, 79, 69, 41]. The ion thus rolls back and forth near the centre of the xy plane (depending on its initial kinetic energy (K.E.)). To see the actual results of the simulated potential we will refer to the co-ordinate frame (x,y) obtained after clockwise rotation by $\frac{\pi}{4}$. The inter-relationship between (x', y') and (x,y) is

$$\begin{aligned} x' &= \frac{x}{\sqrt{2}} + \frac{y}{\sqrt{2}} \\ y' &= -\frac{x}{\sqrt{2}} + \frac{y}{\sqrt{2}} \end{aligned}$$

With this substitution Fig.3.11 shows the V_{rods} (x,y,z,t) plotted for z=0 plane. The z=0 plane is shown at the bottom in Fig.3.9 along with the circular cross-sections of the 4 rods. The actual profile of the rods are used (hence structure factor κ is accounted for) with a diameter of 0.5 mm for the four rods and $r_0 = 0.5$ mm (distance from centre to electrode as defined in Fig.3.9).V_0 is taken to be 1V but can be scaled.Ω^0_{RF} is 20.286 MHz.

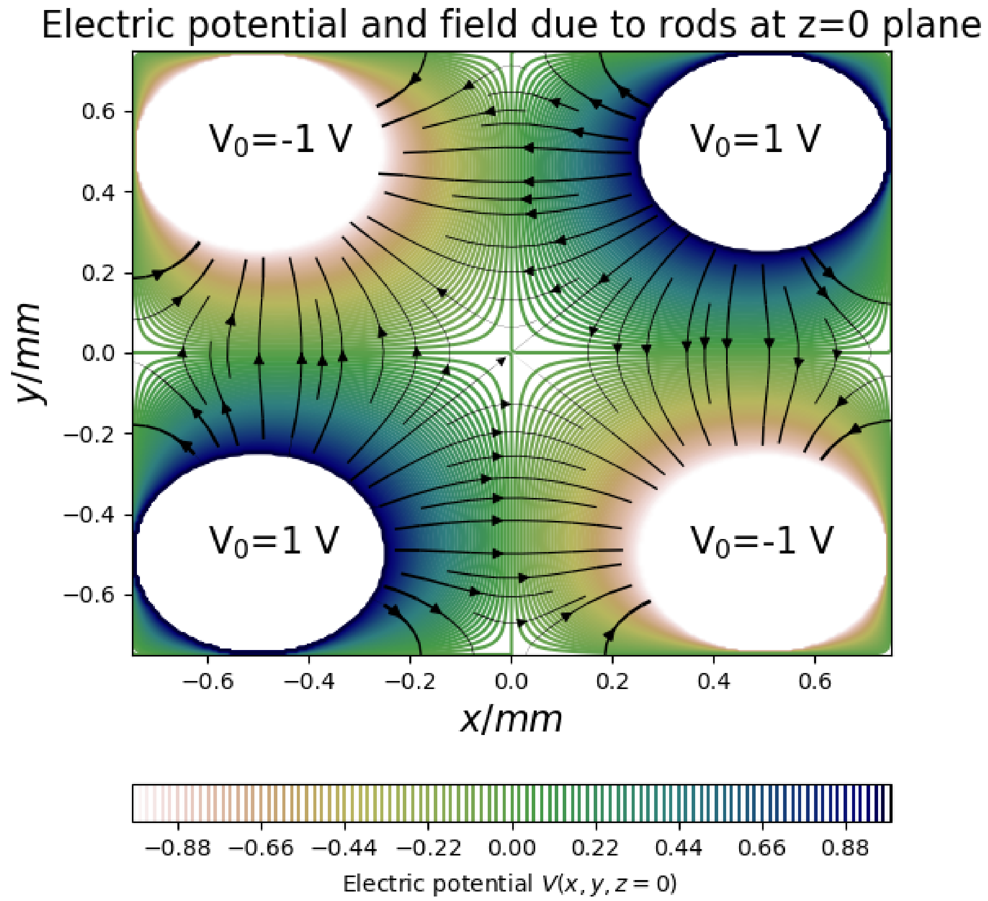

Figure 3.10: Simulated potential (and the electric field lines given by the gradient at each contour of the potential) generated from the 4-rods in the (x,y) plane. See text for further details

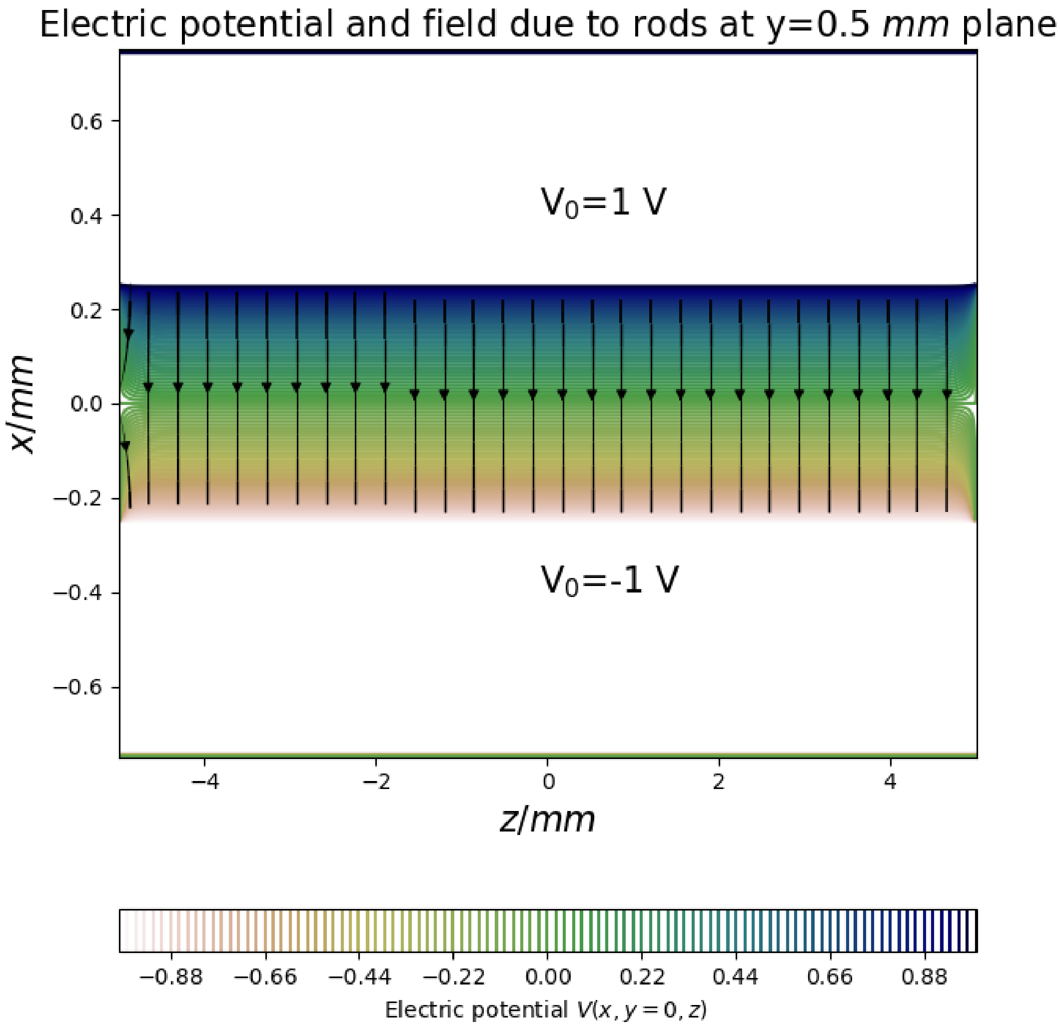

Figure 3.11: Simulated potential (and the electric field lines given by the gradient at each contour of the potential) generated from the 4-rods in the (x,z) frame for y=0.5 mm plane. See text for further details

3.9.2 Potential due to needles

The two needles are powered entirely by DC[41] and hence the accompanying potential is of the form

$$V_{\text{needles}}(x', y', z) = \mathrm{U}_0\left(\frac{\mathrm{z}^2}{\mathrm{z}_0^2} - \frac{\mathrm{x}'^2 + \mathrm{y}'^2}{2\mathrm{z}_0^2}\right)$$

Note to satisfy Maxwell's equation the potential is anti-confining along the transverse direction (x,y) even though it is confining along z. The parameter z_0 has been marked in Fig.3.9. Since the term $x'^2 + y'^2$ is rotationally invariant, the needle potential can also be expressed as

$$V_{\text{needles}}(x, y, z) = \mathrm{U}_0\left(\frac{\mathrm{z}^2}{\mathrm{z}_0^2} - \frac{\mathrm{x}^2 + \mathrm{y}^2}{2\mathrm{z}_0^2}\right)$$

Fig.3.12 shows the simulation of needle potential (and associated electric field in (x,z) for y=0 plane. The conical profile of the needle is used with a base diameter of 0.5 mm and a needle to needle tip distance ($2z_0$) of 2.8 mm as is true in our experimental setup.U_0 is taken to be 1V but can be scaled. This potential generates a harmonic confinement for positive charges along z.

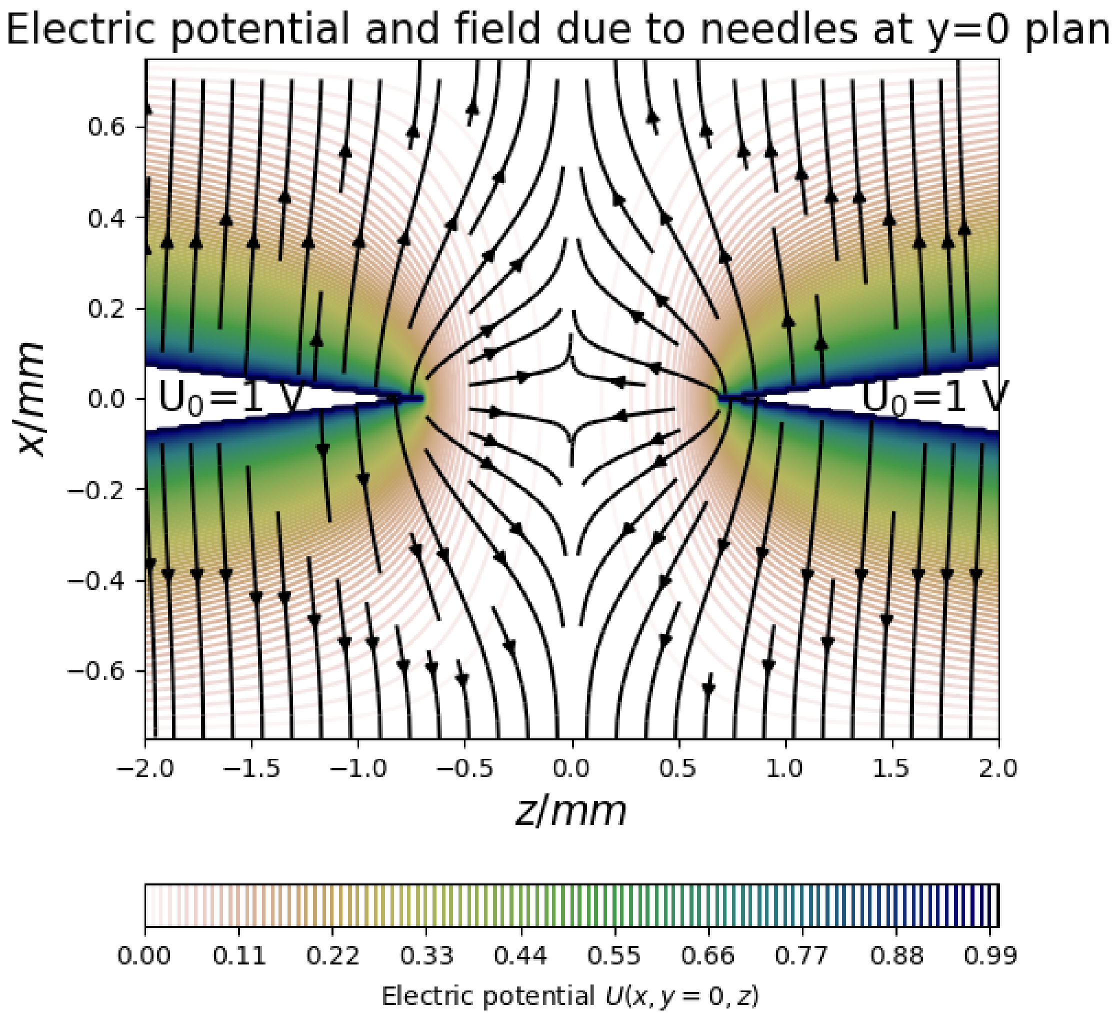

Figure 3.12: Simulated potential (and the electric field lines given by the gradient at each contour of the potential) generated from the needles in (x,z) plane.

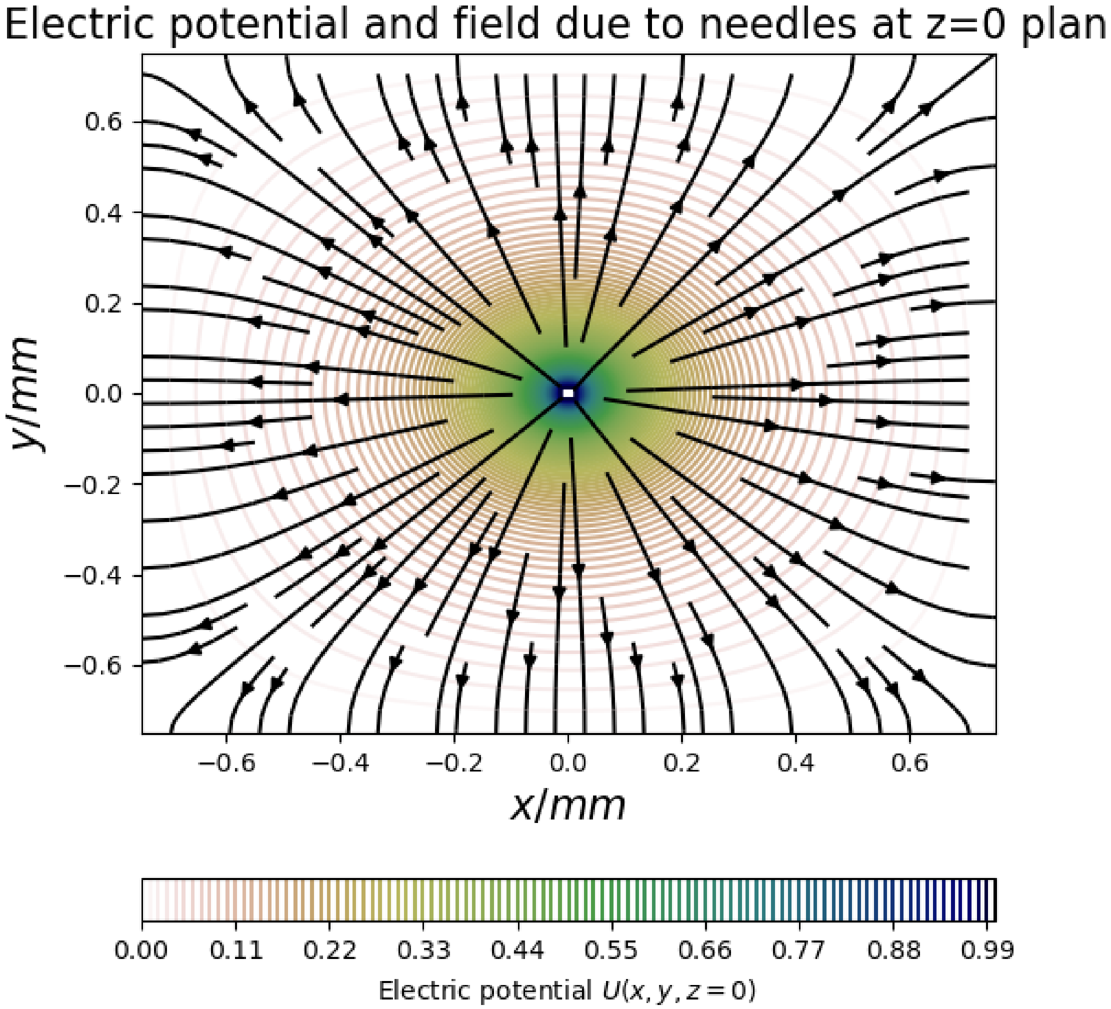

Figure 3.13: Simulated potential (and the electric field lines given by the gradient at each contour of the potential) generated from the needles in (x,y) plane.

3.9.3 Trajectories of ion

In this section we discuss the simulation results of the ion motion under the combined effect of the potential due to rods and needles as discussed in previous sections. The combined potential is

$$V_{total} = V_{\mathrm{needles}}(x', y', z) + V_{\mathrm{rods}}(x', y', z, t) = V_0\kappa \mathrm{Cos}(\Omega^0_{\mathrm{RF}}\mathrm{t})(\frac{\mathrm{x}'^2 - \mathrm{y}'^2}{\mathrm{r}_0^2}) + \mathrm{U}_0(\frac{\mathrm{z}^2}{\mathrm{z}_0^2} - \frac{\mathrm{x}'^2 + \mathrm{y}'^2}{2\mathrm{z}_0^2}) \tag{3.16}$$

Fig.3.14 displays such a trajectory along the x' direction as a function of time. The slower frequency dynamics is due to the trapping frequency (called secular frequency)[78, 43, 46, 79, 69, 41] and the faster ripples are due to unwanted micromotion at the RF drive. The parameters of $(\mathrm{V}_0, \mathrm{U}_0, \Omega^0_{\mathrm{RF}})$ are mentioned in figure itself. $r_0 = 0.5$ mm and $2z_0 = 2.8$ mm. Note that since the actual profile of the rods and needles as used in our simulation has been used, the structure factor κ is already accounted for internally. The trajectory is obtained by solving the equation of motion (EOM) for the coupled x and y-motion using fourth order Runga-Kutta method (commonly known as RK4) . Similar equation exists for y'. Initial condition is such that the ion is at the $x'_0, y'_0 = (-0.005, -0.005)$mm with Kinetic energy (KE) $= 6\mathrm{V}_{\mathrm{total}}(\mathrm{x}'_0, \mathrm{y}'_0, \mathrm{z} = 0)$. The excursion of the ion from the mean position and the amplitude of the ripples can be increased by increasing KE i.e. making the ions hot. For direction z, the motion is uncomplicated simple-harmonic[41] due to the potential in Fig.3.12 and hence is not discussed here further. Fig.3.15 studies the motion in Fourier space (i.e. the Fourier transform of x' (t) is taken). We see that apart from the secular frequency at near 2 MHz, there are two subsidiary peaks near 20.2 MHz due to micromotion caused by the driving RF frequency.

An analytical expression of the secular frequency along x-direction can be deduced from the pondermotive potential[78, 43, 46, 79, 69, 41] which is as follows

$$\omega_x = \frac{q\kappa \mathrm{V}_0}{2\mathrm{m}\mathrm{r}_0^2\Omega^0_{\mathrm{RF}}} - (\frac{U_0^{1/2}}{m^{1/2}z_0})$$

where the last term is due to the anti-confinement by the needle potential in Fig.3.12. The expression shows the secular frequency ω_x is linear in V_0, in $\frac{1}{\Omega^0_{\mathrm{RF}}}$ and in $\frac{1}{\mathrm{m}}$. Fig.3.16, Fig.3.17, Fig3.18 establishes these behavior for the secular frequency obtained from simulation. All our simulation results are for $^{171}\mathrm{Yb}^+$ ion except in Fig.3.18 wherein the mass of the ion is varied.

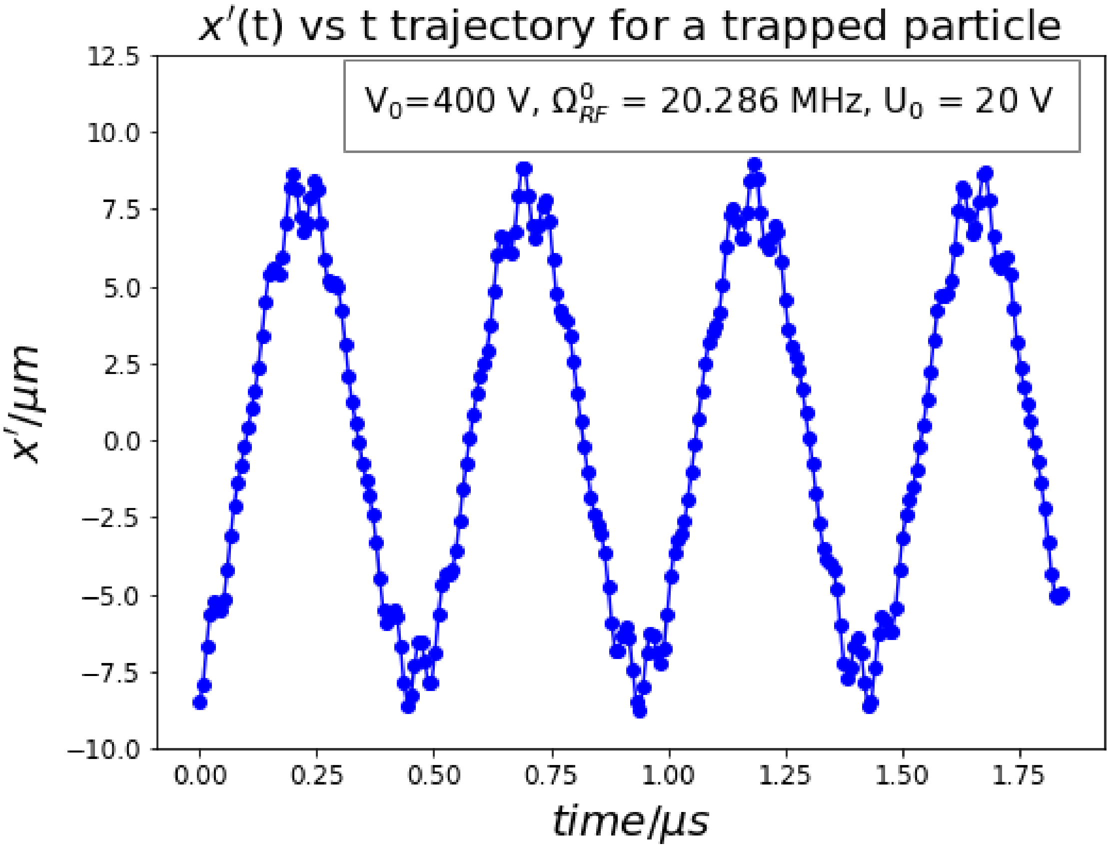

Figure 3.14: The simulated trajectory for the ion along the x'-direction vs time.

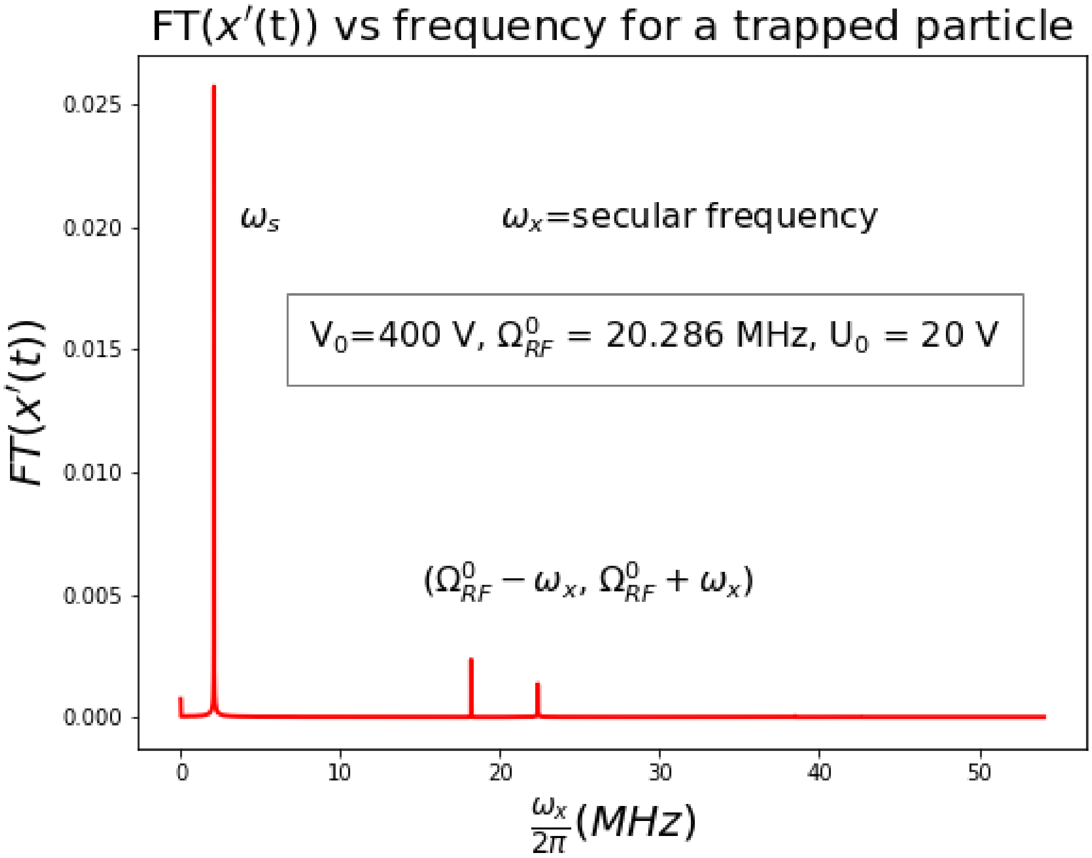

Figure 3.15: The Fast Fourier transform of the plot in Fig.3.14. The secular/trapping frequency $\frac{\omega_x}{2\pi}$ is identified to be the dominant peak at 2 MHz whereas the micromotion sidebands at $\Omega_{RF}^0 + \omega_x$ and $\Omega_{RF}^0 - \omega_x$ are apparent. The amplitude of these sideband peaks increases with increasing initial KE (kinetic energy) i.e. making the ions hot.

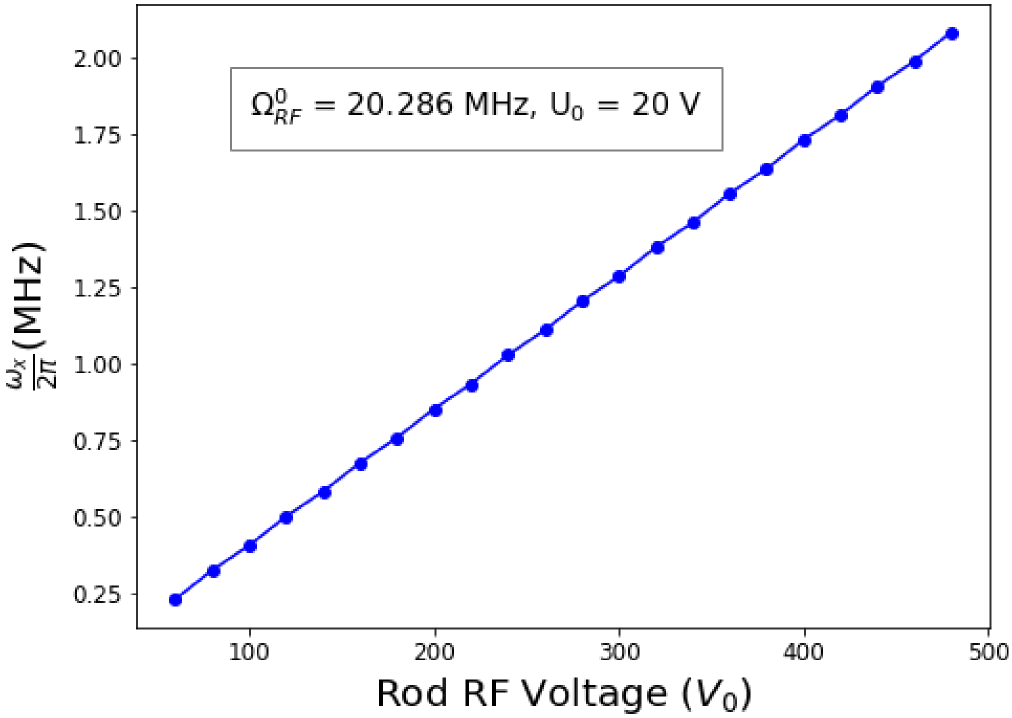

Figure 3.16: The variation of the secular frequency for x-motion or trapping frequency as a function of the input potential (V_0). All relevant parameters are defined within the figure and $r_0 = 0.5$ mm and $2z_0 = 2.8$ mm. Note that since the actual rod parameters were used in the simulation, so structure factor κ is inbuilt and already accounted for. This plot can be used to determine what is the actual potential at the rods if the secular/trapping frequency is experimentally determined. Initially the secular frequency achieved along the x-direction was approximately $2\pi \times 0.4 - 0.43$ MHz which corresponds to a rod voltage of 100-140 V as per the above figure. However the secular frequency along the x-direction was later modified to $2\pi \times 1.0$ MHz with a rod voltage of nearly 230-250 V.

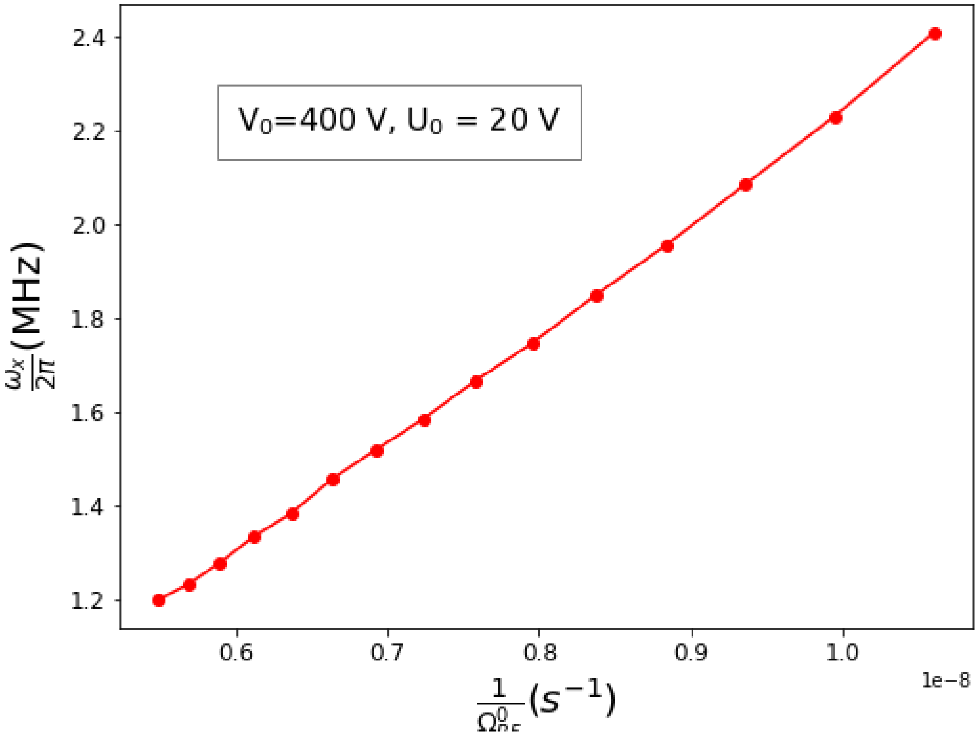

Figure 3.17: The variation of the secular frequency for x-motion or trapping frequency as a function of the inverse of the input RF driving frequency ($\frac{1}{\Omega^0_{\mathrm{RF}}}$). All relevant parameters are defined within the figure and $r_0 = 0.5$ mm and $2z_0 = 2.8$ mm. Note that since the actual rod parameters were used in the simulation, so structure factor κ is inbuilt and already accounted for. This plot can be used to determine the secular/trapping frequency at other values of RF drive.

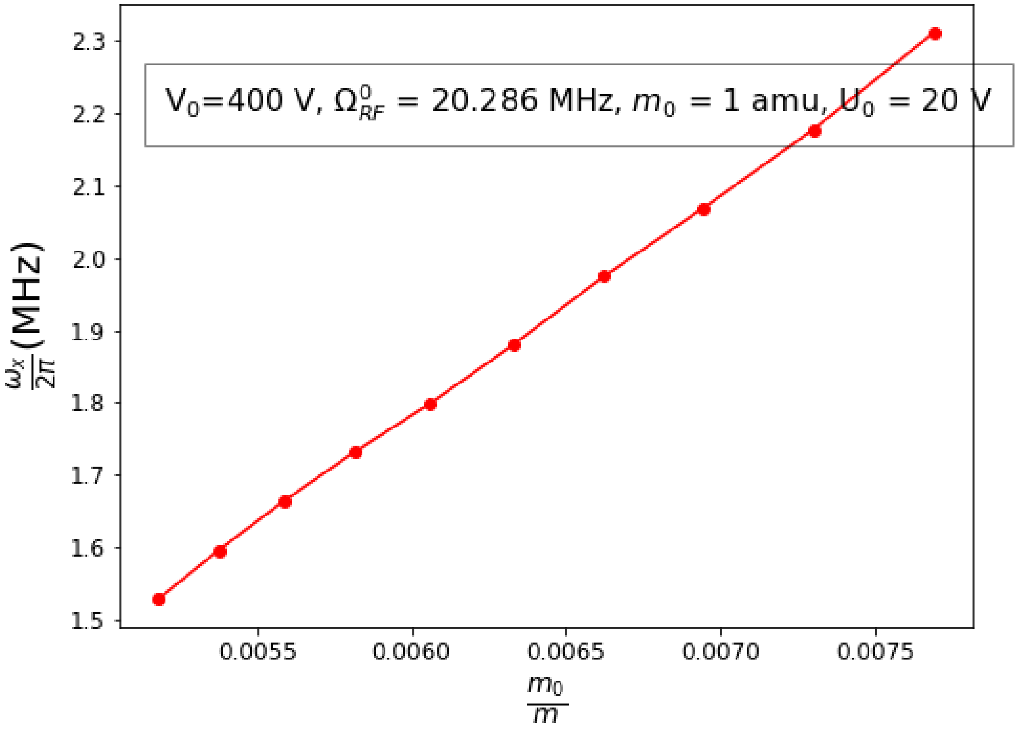

Figure 3.18: The variation of the secular frequency for x-motion or trapping frequency as a function of the inverse of the mass of the ion used ($\frac{1}{\mathrm{m}}$). All relevant parameters are defined within the figure and $r_0 = 0.5$ mm and $2z_0 = 2.8$ mm. Note that since the actual rod parameters were used in the simulation, so structure factor κ is inbuilt and already accounted for. This plot can be used to determine the secular/trapping frequency experienced by other ions within the same trap i.e. for a given rod and needle potential.

3.10 Conclusion

In this chapter we discussed how the helical coil balanced RF resonator is built in the ion-trapping apparatus and what kind of potential it generates at the rod electrodes. An overview of the setup with the resonator is shown in Fig.3.19.

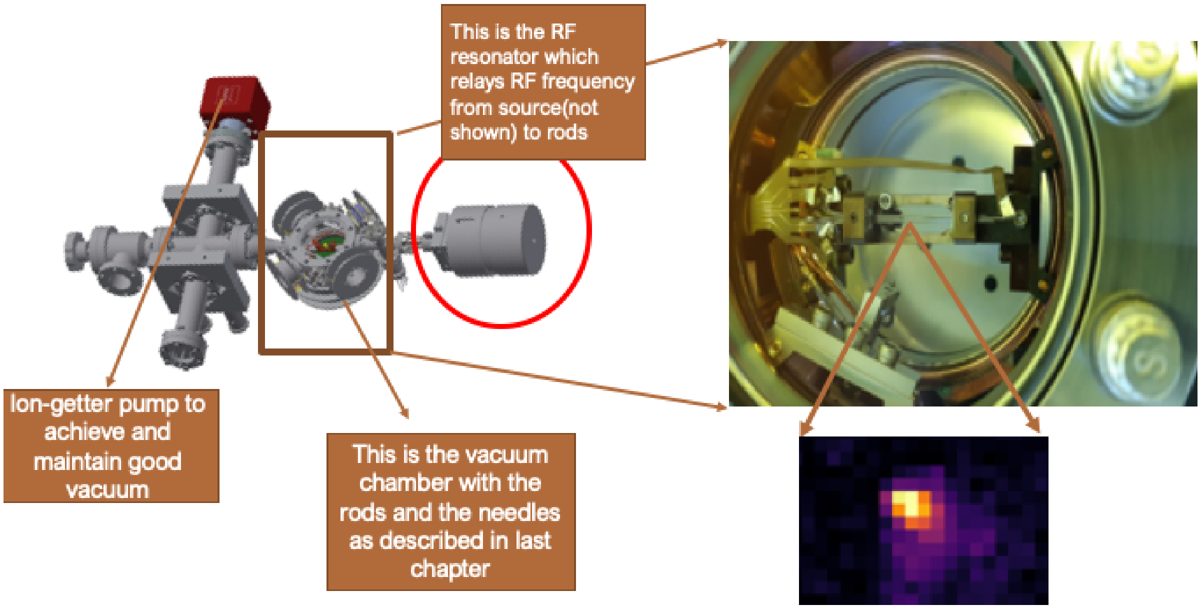

Figure 3.19: The picture of the ion-trapping apparatus used constructed in the group for trapping Yb^{+} ions (both $^{174}\mathrm{Yb}^{+}$ and $^{171}\mathrm{Yb}^{+}$). The main components which involves the vacuum chamber containing the trapping electrodes described in previous chapter, the ion-getter pump for maintaining good vacuum, a helical coil RF resonator (marked within red circle) is shown along with an enlarged view of the inside of the vacuum chamber and location of a single trapped $^{174}\mathrm{Yb}^{+}$ion (illustrated with a picture taken in the group). We detailed the construction of the helical-coil RF resonator (encircled in red) and the circuitry that powers it in this chapter. We also showed the simulation results of potential generated by the RF field and trajectories of ion in it.

Apart from this the setup has been successful in trapping even multiple ions many times. A representative picture of 8 $^{174}\mathrm{Yb}^{+}$ions is shown in Fig.3.20. Similarly multiple $^{171}\mathrm{Yb}^{+}$ions have also been trapped successfully very often. It is needless to emphasize the role played by the RF/DC circuitry in creating a trapping potential for these ions which highlights the importance of this chapter. In the next chapter we shall see how to manipulate the trapping potential externally using optical field.

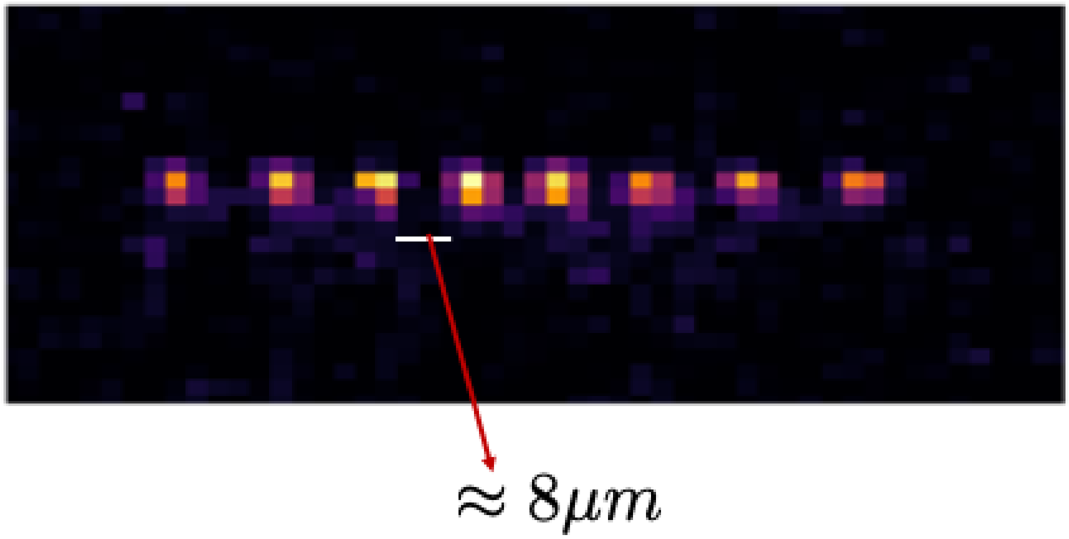

Figure 3.20: The picture of 8 $^{174}\mathrm{Yb}^{+}$ ions trapped using our setup. This picture has been also used in Ref.[83]

Chapter 4

Manipulating the trapping potential using optical tweezers

4.1 Chapter at a glance

In the last chapter we saw how the oscillating potential at RF is created on the rod electrodes and what kind of potential it can generate. We saw that one of the principal component of the RF circuitry as used in our ion-trapping apparatus is a helical coil RF resonator. In this chapter we shall see how to manipulate and control this trapping potential using localized external field like an optical tweezer(ions have been optically trapped before using a global beam as in[84],[85] but cold atoms have been trapped with a localized tweezers as in Ref.[86]). Specifically we will seek answers to the following questions

- What is the effect of an optical tweezer on a single trapped ion ? We shall discuss its effect on the electronic structure of the ion as well as its motional modes separately.
- Can we harness the effect to obtain interesting physical quantities? We shall develop a scheme to realize a quantum thermodynamic protocol wherein dynamically changing the optical power of the tweezer can provide a window into thermal properties of different ion species even without having to trap them in the first place. Results in this chapter from this protocol is being developed as a part of a publication.

4.2 Effect of external optical field on the atomic structure of a single $^{171}\mathrm{Yb}^{+}$ ion

We consider only two of the internal electronic levels of the ion in this treatment. Let them be denoted as $|g\rangle$ with an energy of $-h\omega_0/2$ and $|e\rangle$ with an energy of $h\omega_0/2$. For Yb-171, the choice of $|g\rangle$ could be $|g\rangle = |S_{1/2}, F = 1, m_F = 0, \pm 1\rangle$ and choice of $|e\rangle$ could be $|e\rangle = |P_{1/2}, F = 0, m_F = 0\rangle$ as the transitions are dipole allowed. Let us consider a single mode of a quantized optical field for simplicity with a frequency ω_L which is shone on the ion with a spatial intensity profile as discussed in the previous section. The interaction between this single mode and the two level ion can be expressed using the Jaynes Cummings Hamiltonian[87] as follows:

$$\begin{aligned} \mathrm{H(r)} &= \hbar\frac{\omega_0}{2}\sigma_z + \hbar\omega_L a^\dagger a - \hbar\frac{\langle\mu(r)\rangle.E(r)}{\hbar}(a + a^\dagger)(\sigma^+ + \sigma^-) && (4.1)\\ &= \hbar\frac{\omega_0}{2}\sigma_z + \hbar\omega_L a^\dagger a - \hbar\kappa(r)(a + a^\dagger)(\sigma^+ + \sigma^-) && (4.2) \end{aligned}$$

where

$$\begin{aligned} \sigma_z &= |g\rangle\langle g| - |e\rangle\langle e| \\ \sigma^+ &= |g\rangle\langle e| \\ \sigma^- &= (\sigma^+)^\dagger \\ a = (a^\dagger)^\dagger &= \sum_n \sqrt{n}|n-1\rangle\langle n| \\ \kappa(r) &= \frac{\langle\mu(r)\rangle.E(r)}{\hbar} \end{aligned}$$

where $|n\rangle$ are the Fock states for the photon field with frequency ω_L. Let us consider solution of this system on a case by case basis.

4.2.1 $\kappa(r)$=0

In this case, Eq.4.2 reduces to a sum of two non-interacting Hamiltonian as

$$\mathrm{H(r)}_{\kappa=0} = \hbar\frac{\omega_0}{2}\sigma_\mathrm{z} + \hbar\omega_\mathrm{L}\mathrm{a}^\dagger\mathrm{a} \qquad (4.3)$$

Using the Hamiltonian in 4.3, we see that any product state of the kind $|g, n\rangle$ is an energy eigenstate of the Hamiltonian. Let us compute the energies of of some of these states.

$$\begin{aligned}
\mathrm{E(g,n)} &= \langle \mathrm{g,n|H(r)_{\kappa=0}|g,n}\rangle = \mathrm{n}\hbar\omega_{\mathrm{L}} - \frac{\hbar\omega_0}{2} \\
&= -\frac{\hbar\delta}{2} + (n-\frac{1}{2})\hbar\omega_L \qquad (4.4) \\
\mathrm{E(g,n+1)} &= \langle \mathrm{g,n+1|H(r)_{\kappa=0}|g,n+1}\rangle = \mathrm{(n+1)}\hbar\omega_{\mathrm{L}} - \frac{\hbar\omega_0}{2} \\
&= -\frac{\hbar\delta}{2} + (n+\frac{1}{2})\hbar\omega_L \qquad (4.5) \\
\mathrm{E(e,n-1)} &= \langle \mathrm{e,n-1|H(r)_{\kappa=0}|e,n-1}\rangle = \mathrm{(n-1)}\hbar\omega_{\mathrm{L}} + \frac{\hbar\omega_0}{2} \\
&= \frac{\hbar\delta}{2} + (n-\frac{1}{2})\hbar\omega_L \qquad (4.6) \\
\mathrm{E(e,n)} &= \langle \mathrm{e,n|H(r)_{\kappa=0}|e,n}\rangle = \mathrm{n}\hbar\omega_{\mathrm{L}} + \frac{\hbar\omega_0}{2} \\
&= \frac{\hbar\delta}{2} + (n+\frac{1}{2})\hbar\omega_L \qquad (4.7)
\end{aligned}$$

where we have introduced $\delta = \omega_0 - \omega_L$. With these definition (Eq.3.4-3.7), we immediately see that the energy space will be lumped in 2D manifolds of $|g,n\rangle$ and $|e,n-1\rangle$. This is under the assumption that $\delta \ll \omega_L, \omega_0$. Each such manifold has a mean energy difference of $\hbar\omega_{\mathrm{L}}$ as can be seen from above equations. The spacing between the energy levels of a given manifold is $\hbar\delta$. The pictorial description of the levels is given in Fig.4.1.

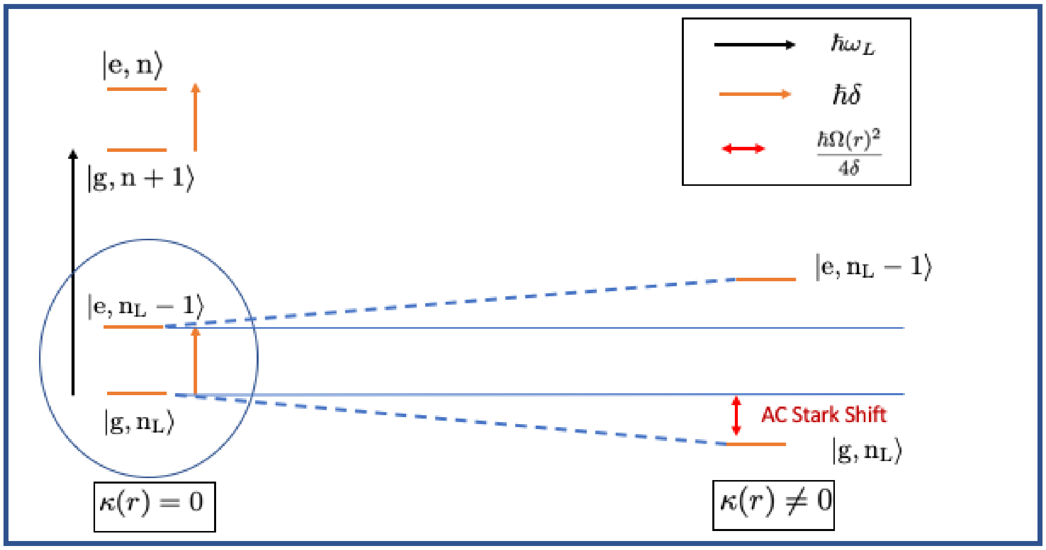

Figure 4.1: The 2D manifold formed from the Fock states of light (such states are labelled with n) and the two energy levels $|e\rangle$ and $g\rangle$ of a two level atom is shown on the extreme left ($\kappa(r) = 0$ case). Each pair of states within the 2D manifold (say state $|e, n-1\rangle$ and $|g, n\rangle$ are inter-separated by $\hbar\delta$ with δ being the detuning is defined as $\omega_0 - \omega_L$. ω_0 is the atomic transition frequency and ω_L is the laser frequency. The states $|g, n\rangle$ and $|g, n+1\rangle$ of two subsequent manifold is separated by $\hbar\omega_L$. The right hand figure shows the case when such pair of states within the 2D manifold is coupled ($\kappa(r) \neq 0$). Since we are considering the case of red-detuning ($\delta \geq 0$) we see that the state $|g, n\rangle$ decreases in energy and the state $|e, n-1\rangle$ increases in energy. This shift is called as AC Stark shift (induced by oscillating electric field of applied laser with frequency ω_L) and is equal to $\frac{\hbar\Omega(r)^2}{4\delta}$

4.2.2 $\kappa(r) \neq 0$

In this case we have to use the entire Hamiltonian in Eq.4.2. To get rid of the cross-terms in Eq.4.2 we make the following transformation

$$\begin{aligned}\tilde{\mathrm{H}}(\mathrm{r},\mathrm{t}) &= \exp(-i\mathrm{H}(\mathrm{r})_{\kappa=0}\mathrm{t})\mathrm{H}(\mathrm{r})\exp(\mathrm{i}\mathrm{H}(\mathrm{r})_{\kappa=0}\mathrm{t}) \\ &= \exp(-i\hbar\frac{\omega_0}{2}\sigma_\mathrm{z}\mathrm{t} - \mathrm{i}\hbar\omega_\mathrm{L}\mathrm{a}^\dagger\mathrm{a}\mathrm{t})\mathrm{H}(\mathrm{r})\exp(\mathrm{i}\hbar\frac{\omega_0}{2}\sigma_\mathrm{z}\mathrm{t} + \mathrm{i}\hbar\omega_\mathrm{L}\mathrm{a}^\dagger\mathrm{a}\mathrm{t}) \qquad (4.8)\end{aligned}$$

To proceed further it will be instructive to have the following:

$$\begin{aligned}\mathrm{a}(\mathrm{t}) &= \exp(-i\hbar\frac{\omega_0}{2}\sigma_\mathrm{z}\mathrm{t} - \mathrm{i}\hbar\omega_\mathrm{L}\mathrm{a}^\dagger\mathrm{a}\mathrm{t})\mathrm{a}\exp(\mathrm{i}\hbar\frac{\omega_0}{2}\sigma_\mathrm{z}\mathrm{t} + \mathrm{i}\hbar\omega_\mathrm{L}\mathrm{a}^\dagger\mathrm{a}\mathrm{t}) \\ &= \exp(-i\hbar\omega_\mathrm{L}\mathrm{a}^\dagger\mathrm{a}\mathrm{t})\mathrm{a}\exp(\mathrm{i}\hbar\omega_\mathrm{L}\mathrm{a}^\dagger\mathrm{a}\mathrm{t}) \\ \frac{\mathrm{d}\mathrm{a}(\mathrm{t})}{\mathrm{d}\mathrm{t}} &= -i\omega_L\exp(-i\hbar\omega_\mathrm{L}\mathrm{a}^\dagger\mathrm{a}\mathrm{t})(\mathrm{a}^\dagger\mathrm{a})(\mathrm{a})\exp(\mathrm{i}\hbar\omega_\mathrm{L}\mathrm{a}^\dagger\mathrm{a}\mathrm{t}) \qquad (4.9) \\ &\quad + i\omega_L\exp(-i\hbar\omega_\mathrm{L}\mathrm{a}^\dagger\mathrm{a}\mathrm{t})(\mathrm{a})(\mathrm{a}^\dagger\mathrm{a})\exp(\mathrm{i}\hbar\omega_\mathrm{L}\mathrm{a}^\dagger\mathrm{a}\mathrm{t}) \\ &= i\omega_L\exp(-i\hbar\omega_\mathrm{L}\mathrm{a}^\dagger\mathrm{a}\mathrm{t})[\mathrm{a},(\mathrm{a}^\dagger\mathrm{a})]\exp(\mathrm{i}\hbar\omega_\mathrm{L}\mathrm{a}^\dagger\mathrm{a}\mathrm{t}) \\ &= -i\omega_L\mathrm{a}(\mathrm{t}) \\ \mathrm{a}(\mathrm{t}) &= \mathrm{a}\exp(-\mathrm{i}\omega_\mathrm{L}\mathrm{t}) \qquad (4.10) \\ \mathrm{a}^\dagger(\mathrm{t}) &= \mathrm{a}^\dagger\exp(\mathrm{i}\omega_\mathrm{L}\mathrm{t}) \qquad (4.11)\end{aligned}$$

Similarly for the spin-space, one can also establish

$$\begin{aligned}\sigma^-(\mathrm{t}) &= \sigma^-\exp(-\mathrm{i}\omega_0\mathrm{t}) \qquad (4.12) \\ \sigma^+(\mathrm{t}) &= \sigma^+\exp(\mathrm{i}\omega_0\mathrm{t}) \qquad (4.13)\end{aligned}$$

With these relations and using Eq.4.8, Eq.4.10, Eq.4.11, Eq.4.12, Eq.4.13 one can write

$$\begin{aligned}\tilde{\mathrm{H}}(\mathrm{r},\mathrm{t}) = \hbar\frac{\omega_0}{2}\sigma_z + \hbar\omega_L a^\dagger a - \hbar\kappa(r)(a\sigma^+\exp(-i(\omega_L-\omega_0)t) + a^\dagger\sigma^+\exp(i(\omega_L+\omega_0)t) \\ + a\sigma^-\exp(i(\omega_L+\omega_0)t) + a^\dagger\sigma^-\exp(i(\omega_L-\omega_0)t)) \qquad (4.14)\end{aligned}$$

Now for our case the, detuning $\delta = \omega_L - \omega_0$ will be in GHz but the term $\omega_L + \omega_0$ will be THz, so it is safe to discard the terms oscillating with such fast frequencies. We will mainly be interested in the dynamics at the frequency scale $\delta = \omega_L - \omega_0$ and terms moving significantly faster can thus be disregarded (Rotating wave approximation or RWA). If we drop those terms from Eq.4.14 then we get a simplified Hamiltonian $\tilde{\mathrm{H}}(\mathrm{r},\mathrm{t})$

$$\tilde{\mathrm{H}}(\mathrm{r},\mathrm{t}) = \hbar\frac{\omega_0}{2}\sigma_z + \hbar\omega_L a^\dagger a - \hbar\kappa(r)(a\sigma^+\exp(-i(\omega_L-\omega_0)t) + a^\dagger\sigma^-\exp(i(\omega_L-\omega_0)t)) \qquad (4.15)$$

If we transform back i.e. invert the unitary back and do the following transformation then we get

$$\begin{aligned}
\mathrm{H(r)} &= \exp(i\mathrm{H(r)}_{\kappa=0}\mathrm{t})\tilde{\mathrm{H}}(\mathrm{r,t})\exp(-\mathrm{iH(r)}_{\kappa=0}\mathrm{t}) \\
&= \exp(i\hbar\frac{\omega_0}{2}\sigma_{\mathrm{z}}\mathrm{t} + \mathrm{i}\hbar\omega_{\mathrm{L}}\mathrm{a}^\dagger\mathrm{at})(\hbar\frac{\omega_0}{2}\sigma_{\mathrm{z}} + \hbar\omega_{\mathrm{L}}\mathrm{a}^\dagger\mathrm{a} - \hbar\kappa(\mathrm{r})(\mathrm{a}\sigma^+\exp(-\mathrm{i}(\omega_{\mathrm{L}} - \omega_0)\mathrm{t}) \\
&+ a^\dagger\sigma^-\exp(i(\omega_L - \omega_0)t)))\exp(-i\hbar\frac{\omega_0}{2}\sigma_{\mathrm{z}}\mathrm{t} - \mathrm{i}\hbar\omega_{\mathrm{L}}\mathrm{a}^\dagger\mathrm{at}) \\
&= \hbar\frac{\omega_0}{2}\sigma_{\mathrm{z}} + \hbar\omega_{\mathrm{L}}\mathrm{a}^\dagger\mathrm{a} - \hbar\kappa(\mathrm{r})(\mathrm{a}\sigma^+ + \mathrm{a}^\dagger\sigma^-) \qquad (4.16)
\end{aligned}$$

We shall use Eq.4.16 for further analysis only. We can express this Hamiltonian in the basis of $|g,n\rangle$ and $|e,n-1\rangle$ which are the uncoupled states of the initial 2D manifold.

$$\langle \mathrm{g,n}|\mathrm{H(r)}|\mathrm{g,n}\rangle = -\frac{\hbar\delta}{2} + (n-\frac{1}{2})\hbar\omega_L \qquad (4.17)$$

$$\langle \mathrm{e,n-1}|\mathrm{H(r)}|\mathrm{e,n-1}\rangle = \frac{\hbar\delta}{2} + (n-\frac{1}{2})\hbar\omega_L \qquad (4.18)$$

$$\langle \mathrm{g,n}|\mathrm{H(r)}|\mathrm{e,n-1}\rangle = -\hbar\kappa(\mathrm{r})^*\sqrt{\mathrm{n}}/\hbar \qquad (4.19)$$

$$\langle \mathrm{e,n-1}|\mathrm{H(r)}|\mathrm{g,n}\rangle = -\hbar\kappa(\mathrm{r})\sqrt{\mathrm{n}}/\hbar \qquad (4.20)$$

Let us make the substitution $\hbar\kappa(\mathrm{r})\sqrt{\mathrm{n}}/\hbar = -\frac{\hbar\Omega(\mathrm{r})\exp(\mathrm{i}\phi(\mathrm{r}))}{2}$. This substitution is valid because in general the quantity $\hbar\kappa(\mathrm{r})\sqrt{\mathrm{n}}/\hbar$ would be a complex number i.e. $\in$ C. Thus it should be expressible both as an amplitude and a phase. In this substitution $\hbar\Omega(r)$ acts as the amplitude and $\phi(r)$ acts as the phase of the term $\hbar\kappa(\mathrm{r})\sqrt{\mathrm{n}}/\hbar$. Since the Hamiltonian is hermitian , the phase $\phi(r)$ only appears in the two off-diagonal elements. The eigenvalues of the 2×2 matrix being entirely controlled by the trace and determinant of the matrix is insensitive to the phase $\phi(r)$. However the eigenvectors will depend on it. Since for our further discussion we will focus only on the eigenvalues and not on the eigenvectors, to see the effect of the amplitude $\hbar\Omega(r)$ or the phase $\phi(r)$ on the eigenvectors one can refer to Ref[87]. The matrix form of the above equations due to this substitution are:

$\begin{pmatrix} -\frac{\hbar\delta}{2} + (n-\frac{1}{2})\hbar\omega_L & -\frac{\hbar\Omega(r)\exp(-i\phi(r))}{2} \\ -\frac{\hbar\Omega(r)\exp(i\phi(r))}{2} & \frac{\hbar\delta}{2} + (n-\frac{1}{2})\hbar\omega_L \end{pmatrix}$ The eigenvalues of this matrix are

$$E_1(r) = (n-\frac{1}{2})\hbar\omega_L - \frac{\hbar\sqrt{\delta^2 + \Omega(r)^2}}{2} \qquad (4.21)$$

$$E_2(r) = (n-\frac{1}{2})\hbar\omega_L + \frac{\hbar\sqrt{\delta^2 + \Omega(r)^2}}{2} \qquad (4.22)$$

For most calculations below, we work in the limit of $\delta \gg \Omega(r)$ to prevent exciting the target transition. In this limit the eigenvalues in above equation reduces to

$$\begin{aligned} E_1(r) &= (n - \frac{1}{2})\hbar\omega_L - \frac{\hbar\delta}{2} - \frac{\hbar\Omega(r)^2}{4\delta} \\ &= \mathrm{E(g, n)} - \frac{\hbar\Omega(\mathrm{r})^2}{4\delta} \end{aligned} \tag{4.23}$$

$$\begin{aligned} E_2(r) &= (n - \frac{1}{2})\hbar\omega_L + \frac{\hbar\delta}{2} + \frac{\hbar\Omega(r)^2}{4\delta} \\ &= \mathrm{E(e, n-1)} + \frac{\hbar\Omega(\mathrm{r})^2}{4\delta} \end{aligned} \tag{4.24}$$

Fig.4.1 has the AC Stark shift created by the optical potential for $\kappa(r) \neq 0$ case shown on extreme right. We specifically show the example of a red-detuned laser beam for a two-level atom with electronic energy states denoted as $|g\rangle$ and $|e\rangle$.

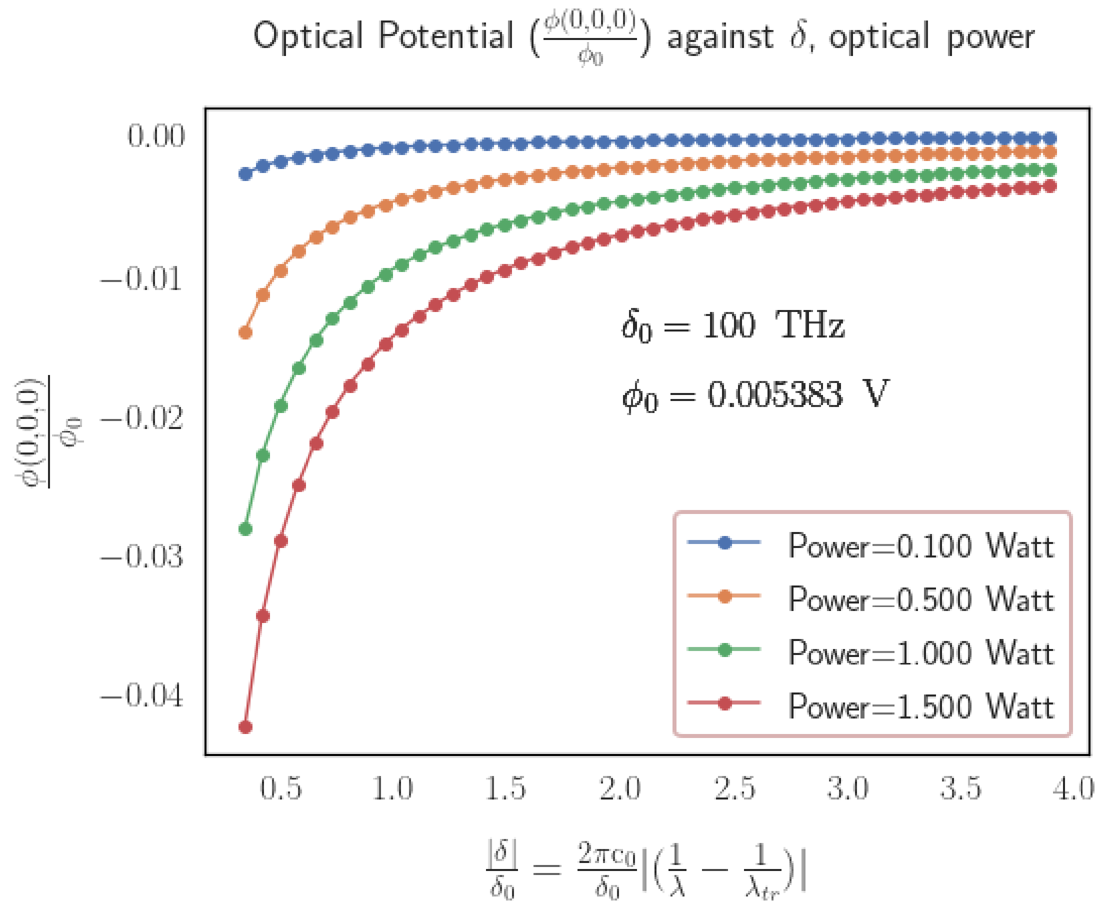

Figure 4.2: The optical potential (denoted here as $\Phi(x, y, z)$ is plotted as a function of δ and intensity ($\Omega(r)$). We focus on the red-detuned case ($\delta \geq 0$) where the potential is confining for the state $|\mathrm{g}, \mathrm{n}\rangle$ as seen in Eq.4.23. The focal point of the Gaussian beam used is at (0,0,0) which is also the location of maximum magnitude of the optical potential. The ion $^{171}\mathrm{Yb}^{+}$ is considered to be located at the focal point and hence $\Phi(0, 0, 0)$ is used for the analysis. The beam waist ($_0$) of the Gaussian beam propagating along x direction is 1 μm

4.3 Effect of external optical field on motional modes of a single $^{171}\mathrm{Yb}^+$ ion

In this section we analyze the $\mathrm{H}_{\mathrm{ext}}(\mathrm{r})$ that was neglected in the discussion for the previous section. This $\mathrm{H}_{\mathrm{ext}}(\mathrm{r})$ has the following form in the ground state of ion+field combined system i.e. when the internal electronic state of the ion is $|g\rangle$ and that of the field is the Fock state $|n\rangle$. The Hamiltonian reads

$$\begin{aligned}\mathrm{H}_{\mathrm{ext}}(\mathrm{r}) &= \sum_{r=x,y,z}\frac{p_r^2}{2m} + \sum_{r=x,y,z}\frac{m\omega_r^2(r-r_0)^2}{2} - \frac{\hbar\Omega(r)^2}{4\delta} \\ &= \sum_{r=x,y,z}\frac{p_r^2}{2m} + \sum_{r=x,y,z}\frac{m\omega_r^2(r-r_0)^2}{2} - \underbrace{\frac{\hbar\tilde{\Omega}^2}{4\delta}\mathrm{I}(\mathrm{r})}_{\mathrm{V}_{\mathrm{opt}}}\end{aligned} \tag{4.25}$$

where we have defined $\tilde{\Omega} = \frac{\Omega}{\sqrt{I(r)}}$ and r_0 denotes the equilibrium position of the ion in absence of optical field i.e. in presence of only the RF and DC potential (discussed in last chapter) from the trap electrodes. It is reasonable to assume that the mean position of the ion along all three directions in presence of the optical field would be different. Let us call this new set of equilibrium co-ordinates as r_{eq} to signify that they are different from r_0. Now for small displacements of the trapped ion about this new equilibrium position r_{eq} we will only retain till the 2nd-order term in the Taylor expansion of the optical potential (optical). To do this let us compute the following

$$\begin{gathered}\mathrm{V}_{\mathrm{opt}}(\mathrm{r}) = \mathrm{V}_{\mathrm{opt}}(\mathrm{r}=\mathrm{r}_{\mathrm{eq}}) + \nabla\mathrm{V}_{\mathrm{opt}}|_{\mathrm{r}=\mathrm{r}_{\mathrm{eq}}}(\mathrm{r}-\mathrm{r}_{\mathrm{eq}}) + \nabla^2\mathrm{V}_{\mathrm{opt}}|_{\mathrm{r}=\mathrm{r}_{\mathrm{eq}}}(\mathrm{r}-\mathrm{r}_{\mathrm{eq}})^2 + \mathcal{O}((\mathrm{r}-\mathrm{r}_{\mathrm{eq}})^3) \\ \frac{\hbar\tilde{\Omega}^2}{4\delta}\mathrm{I}(\mathrm{r}) = \frac{\hbar\tilde{\Omega}^2}{4\delta}\mathrm{I}(\mathrm{r}_{\mathrm{eq}}) + \frac{\hbar\tilde{\Omega}^2}{4\delta}\nabla\mathrm{I}(\mathrm{r})|_{\mathrm{r}_{\mathrm{eq}}}(\mathrm{r}-\mathrm{r}_{\mathrm{eq}}) + \frac{\hbar\tilde{\Omega}^2}{4\delta}\nabla^2\mathrm{I}(\mathrm{r})|_{\mathrm{r}=\mathrm{r}_{\mathrm{eq}}}(\mathrm{r}-\mathrm{r}_{\mathrm{eq}})^2 + \mathcal{O}((\mathrm{r}-\mathrm{r}_{\mathrm{eq}})^3)\end{gathered} \tag{4.26}$$

$$\begin{aligned}&\forall\ \ \mathrm{r}\ \epsilon\ \ \{\mathrm{x},\mathrm{y},\mathrm{z}\} \\ &\forall\ \ \mathrm{r}_{\mathrm{eq}}\ \epsilon\ \ \{\mathrm{x}_{\mathrm{eq}},\mathrm{y}_{\mathrm{eq}},\mathrm{z}_{\mathrm{eq}}\}\end{aligned}$$

We shall now use Eq.4.26 to perform certain simplications on the optical potential. Henceforth we shall disregard the $\mathcal{O}((r-r_{eq})^3)$ term completely and focus only on the 1st three terms which entails the quadratic expansion.

Using Eq.4.26 in Eq.4.25 and defining $\tilde{\mathrm{H}}_{\mathrm{ext}}(\mathrm{r}) = \mathrm{H}_{\mathrm{ext}}(\mathrm{r}) - \sum_{\mathrm{r}=\mathrm{x},\mathrm{y},\mathrm{z}}\frac{\mathrm{p}_{\mathrm{r}}^2}{2\mathrm{m}}$ we get

$$
\begin{aligned}
\tilde{\mathrm{H}}_{\mathrm{ext}}(\mathrm{r}) &= \sum_{r=x,y,z} \frac{m\omega_r^2(r-r_0)^2}{2} - \frac{\hbar\Omega(r)^2}{4\delta} \qquad \text{See Eq.4.25} \\
&= \sum_{r=x,y,z} \frac{m\omega_r^2(r-r_0)^2}{2} - \sum_{r=x,y,z} \frac{\hbar\tilde{\Omega}^2}{4\delta}\mathrm{I}(\mathrm{r_{eq}}) \qquad \text{See Eq.4.26} \\
&- \sum_{r=x,y,z} \frac{\hbar\tilde{\Omega}^2}{4\delta}\nabla\mathrm{I}(\mathrm{r})|_{\mathrm{r_{eq}}}(\mathrm{r}-\mathrm{r_{eq}}) - \sum_{\mathrm{r=x,y,z}} \frac{\hbar\tilde{\Omega}^2}{4\delta}\nabla^2\mathrm{I}(\mathrm{r})|_{\mathrm{r=r_{eq}}}(\mathrm{r}-\mathrm{r_{eq}})^2 \\
&= \sum_{r=x,y,z} \frac{m\omega_r^2(r-r_{eq})^2}{2} + \sum_{r=x,y,z} \frac{m\omega_r^2(r_{eq}-r_0)^2}{2} \\
&+ \sum_{r=x,y,z} m\omega_r^2(r_{eq}-r_0)(r-r_{eq}) - \sum_{r=x,y,z} \frac{\hbar\tilde{\Omega}^2}{4\delta}\mathrm{I}(\mathrm{r_{eq}}) \\
&+ \sum_{r=x,y,z} -\frac{\hbar\tilde{\Omega}^2}{4\delta}\nabla\mathrm{I}(\mathrm{r})|_{\mathrm{r_{eq}}}(\mathrm{r}-\mathrm{r_{eq}}) - \sum_{r=x,y,z} \frac{\hbar\tilde{\Omega}^2}{4\delta}\nabla^2\mathrm{I}(\mathrm{r})|_{\mathrm{r=r_{eq}}}(\mathrm{r}-\mathrm{r_{eq}})^2 \\
&= \sum_{r=x,y,z} \frac{m\omega_r^2(r-r_{eq})^2}{2} + \sum_{r=x,y,z} \frac{m\omega_r^2(r_{eq}-r_0)^2}{2} - \sum_{r=x,y,z} \frac{\hbar\tilde{\Omega}^2}{4\delta}\mathrm{I}(\mathrm{r_{eq}}) \\
&- \sum_{r=x,y,z} \frac{\hbar\tilde{\Omega}^2}{4\delta}\nabla^2\mathrm{I}(\mathrm{r})|_{\mathrm{r=r_{eq}}}(\mathrm{r}-\mathrm{r_{eq}})^2 \qquad (4.27)
\end{aligned}
$$

where in the last line we have used the fact that the sum of the terms in red vanishes for each r as it defines the gradient of the overall potential. The overall potential is the sum of optical and conventional trapping potential generated by RF and DC as discussed in previous chapter. This conventional trapping potential engenders the initial trapping frequency ω_r as used above. The overall potential is minimized to obtain the equilibrium position of the ion which requires setting the gradient of the overall potential to zero. The gradient of the overall potential is defined as

$$
\nabla\left(-\frac{\hbar\tilde{\Omega}^2}{4\delta}\mathrm{I}(\mathrm{r}) + \frac{m\omega_r^2(r-r_0)^2}{2}\right)\Big|_{r-r_{eq}} \qquad (4.28)
$$

Setting Eq.4.28 to zero we get

$$
\begin{aligned}
\nabla(-\frac{\hbar\tilde{\Omega}^2}{4\delta}\mathrm{I(r)} + \frac{m\omega_r^2(r-r_0)^2}{2})|_{r-r_{eq}} &= 0 \\
-\frac{\hbar\tilde{\Omega}^2}{4\delta}\nabla\mathrm{I(r)}|_{\mathrm{r_{eq}}} + \mathrm{m}\omega_{\mathrm{r}}^2(\mathrm{r_{eq}}-\mathrm{r_0}) &= 0 \quad \forall \;\; \mathrm{r} \;\epsilon\; \{\mathrm{x,y,z}\} \\
m\omega_r^2(r_{eq}-r_0)(r-r_{eq}) - \frac{\hbar\tilde{\Omega}^2}{4\delta}\nabla\mathrm{I(r)}|_{\mathrm{r_{eq}}}(\mathrm{r}-\mathrm{r_{eq}}) &= 0 \quad \forall \;\; \mathrm{r} \;\epsilon\; \{\mathrm{x,y,z}\} \\
\sum_{r=x,y,z} m\omega_r^2(r_{eq}-r_0)(r-r_{eq}) - \frac{\hbar\tilde{\Omega}^2}{4\delta}\nabla\mathrm{I(r)}|_{\mathrm{r_{eq}}}(\mathrm{r}-\mathrm{r_{eq}}) &= 0 \qquad (4.29)
\end{aligned}
$$

The Eq.4.29 explains why the sum of the terms in red vanishes. Now if we disregard the constant terms in blue i.e set the scale of energy to zero at the sum of these constant terms then the final external Hamiltonian we get

$$
\begin{aligned}
\mathrm{H_{ext}(r)} - \sum_{\mathrm{r=x,y,z}}\frac{\mathrm{p_r^2}}{\mathrm{2m}} &= \sum_{r=x,y,z}\frac{m\omega_r^2(r-r_{eq})^2}{2} - \sum_{r=x,y,z}\frac{\hbar\tilde{\Omega}^2}{4\delta}\nabla^2\mathrm{I(r)}|_{\mathrm{r=r_{eq}}}(\mathrm{r}-\mathrm{r_{eq}})^2 \\
\tilde{\mathrm{H}}_{\mathrm{ext}}(\mathrm{r}) &= \sum_{r=x,y,z}\frac{m}{2}(\omega_r^2 - \frac{\hbar\tilde{\Omega}^2}{2\delta m}\nabla^2\mathrm{I(r)}|_{\mathrm{r=r_{eq}}})(\mathrm{r}-\mathrm{r_{eq}})^2 \\
&= \sum_{r=x,y,z}\frac{m}{2}\tilde{\omega}_r^2(r-r_{eq})^2 \qquad (4.30) \\
\mathrm{H_{ext}(r)} &= \sum_{r=x,y,z}\frac{p_r^2}{2m} + \sum_{r=x,y,z}\frac{m}{2}\tilde{\omega}_r^2(r-r_{eq})^2
\end{aligned}
$$

Eq.4.30 indicates that the effective trap frequency is

$$
\tilde{\omega_r}^2 = \omega_r^2(1 - \frac{\hbar\tilde{\Omega}^2}{2\delta\mathrm{m}\omega_{\mathrm{r}}^2}\nabla^2\mathrm{I(r)}|_{\mathrm{r=r_{eq}}}) \qquad \forall \;\; \mathrm{r} \;\epsilon\; \{\mathrm{x,y,z}\} \tag{4.31}
$$

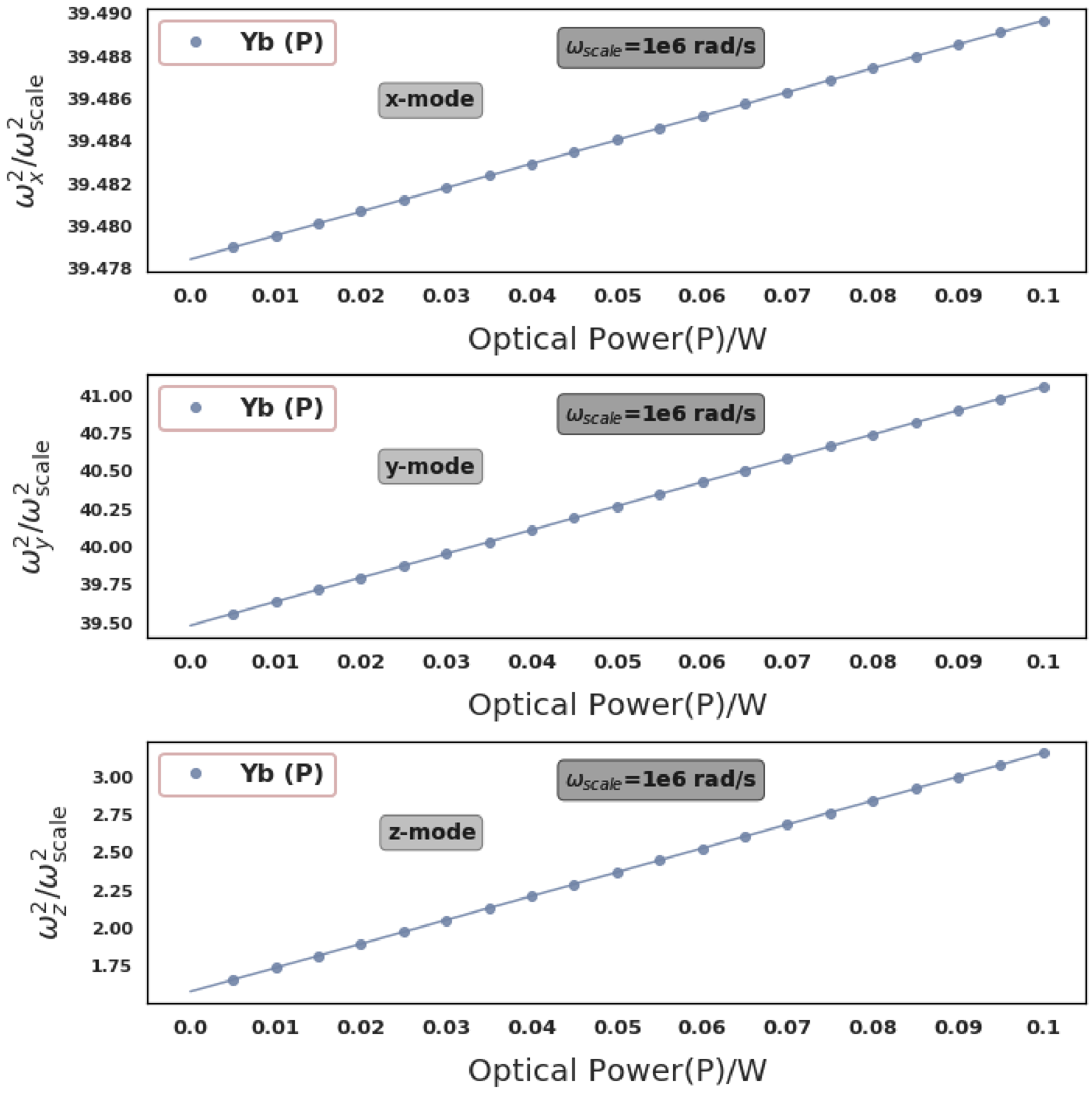

Figure 4.3: The change in the square of the trapping frequency of the motional mode along all three directions for a single $^{171}\text{Yb}^{+}$ ion. The diagram is constructed using a red-detuned beam of wavelength = 375 nm (the detuning in frequency space δ is non-negative as defined for the red-detuned beam but the detuning in wavelength space is negative and for this case is -5.5 nm.) We use a Gaussian beam focused to a beam waist(defined as the distance from the focal point over which the Gaussian beam intensity falls to $\frac{1}{e^2}$ of its maximum value) of 1μm. We see while the transverse (y,z) mode changes by equal amount from their respective initial trapping frequencies, the change in the trapping strength for x mode is very little.

Few points are apparent from Fig.4.3 which can be summarized as follows

- The plot for ω^2 vs Power is linear in conformity with Eq.4.30.
- While the change in ω^2 for the y and z mode happens to be with equal extent , the ω^2 for the x-mode does not change much. This is a consequence of the fact that we used a Gaussian beam propagating along the x-direction to generate the optical potential. It is a well-known fact that for a Gaussian mode of EM field, the beam intensity along the two transverse directions (directions perpendicular to direction of propagation of the beam) diminishes exponentially radially from the centre of the beam which is the focal point. For the axial direction (along the of propagation of the beam) beam intensity changes quadratically from the focal point. As a result, the curvature of the intensity along the transverse direction is high as the beam intensity is concentrated and squeezed over a shorter length scale. We see that Eq.4.30 indicates that the change in trapping frequency happens due to the curvature of the intensity hence for the transverse mode (y,z) the change in trapping frequency in our case would be higher than the axial mode (x).

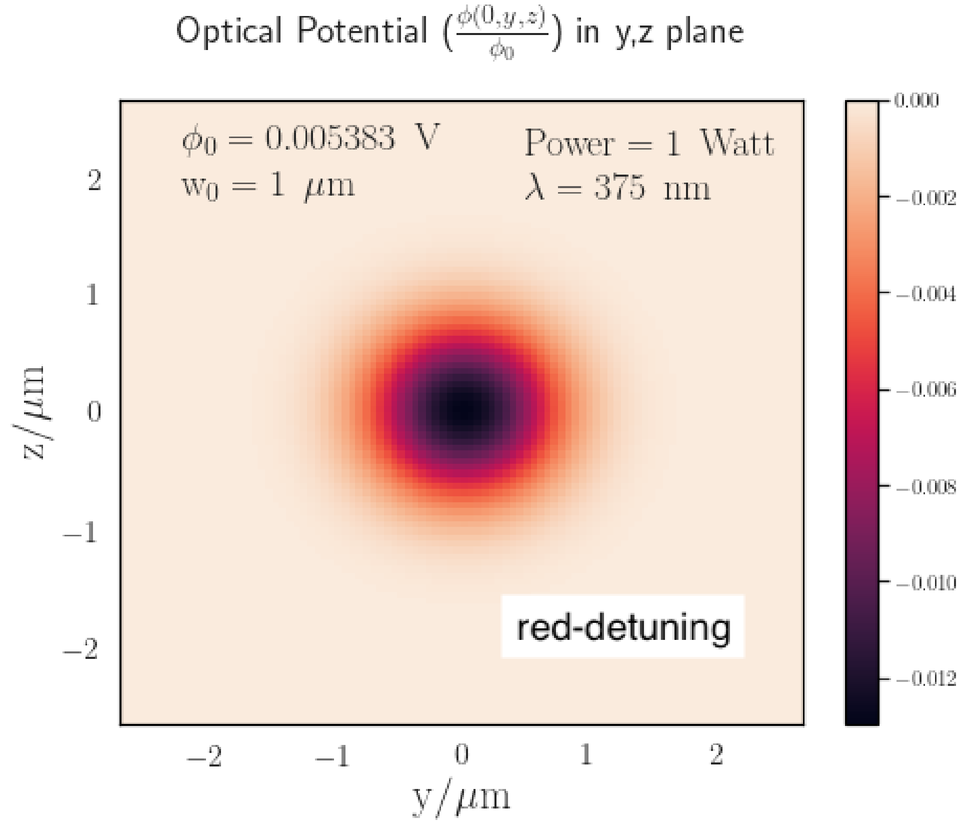

Figure 4.4: The optical potential (denoted here as $\Phi(x, y, z)$ is plotted as a function of y and z for x=0. We focus on the red-detuned case ($\delta \geq 0$) where the potential is confining for the state $|g, n\rangle$ as seen in Eq.4.23 which explains the negative sign of the $\Phi(x = 0, y, z)$ scale .A Gaussian beam of λ = 375 nm (propagating along x direction) is used for the calculation with a beam waist(w_0) of 1 μm. The location of the ^{171}Yb$^+$ ion is at the centre of the beam i.e. at (0,0,0). We see that the potential $\Phi(x = 0, y, z)$ nearly drops by 100% within a span of ± 1 μm in either axis.

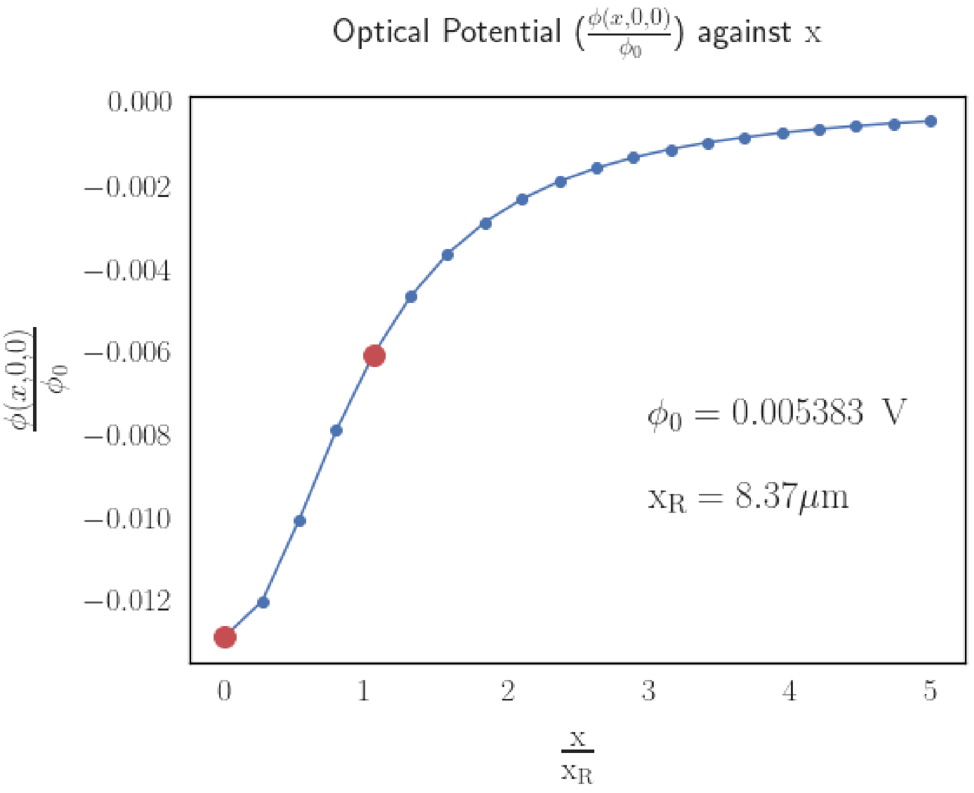

Figure 4.5: The optical potential (denoted here as $\Phi(x, y, z)$ is plotted as a function of x only for y=z=0. We focus on the red-detuned case ($\delta \geq 0$) where the potential is confining for the state $|\text{g}, \text{n}\rangle$ as seen in Eq.4.23 which explains the negative sign of the $\Phi(x = 0, y, z)$ scale .A Gaussian beam of λ = 375 nm (propagating along x direction) is used for the calculation with a beam waist(w_0) of 1 μm. The location of the ^{171}Yb$^+$ ion is at the centre of the beam i.e. at (0,0,0). We see that the potential $\Phi(x, y = 0, z = 0)$ drops only by 50% within a span of 1 x_R (Rayleigh range) which for this wavelength is 8.37 μm. Thus the change in the potential along x (the direction of propagation of the beam) is weaker than in y and z which explains why the x-mode is affected less.

4.4 Quantum Thermodynamics with Trapped Ions

Quantum description of thermal properties of matter have garnered attention in recent years due to its ability to unravel the origin of irreversibility from a microscopic lens[88], in designing devices for heatronics and thermal transport [89, 90, 91, 92, 93], in construction of measurement driven thermal engines[94, 95] or in resource-theoretic formulation of thermodynamics[96, 97]. In the next few section we shall develop a quantum thermodynamic protocol to extract free energy and other thermal properties of mixed-ion chain using optical tweezer on single-species ion chains. But before we move into the proposal, let us define the necessary terms and a prove a key theorem due to Jarynski[98] which will be the centre piece of our scheme.

4.4.1 Definition of heat, work and Free energy

Let us consider an arbitrary transformation in which the Hamiltonian of the system is changing as a function of time. The energy of the system at any time t is obtainable from the state as

$$\langle \mathrm{E(t)} \rangle = \mathrm{Tr}(\rho(\mathrm{t})\mathrm{H(t)})$$

The derivative of the energy $\langle E(t) \rangle$ is then given by

$$\frac{d\langle \mathrm{E(t)} \rangle}{dt} = \mathrm{Tr}(\frac{\mathrm{d}\rho(\mathrm{t})}{\mathrm{dt}}\mathrm{H(t)}) + \mathrm{Tr}(\frac{\mathrm{dH(t)}}{\mathrm{dt}}\rho(\mathrm{t})) \tag{4.32}$$

Then the nett change in energy of the system is

$$\Delta \mathrm{E(t)} = \int \frac{d\langle \mathrm{E(t)} \rangle}{dt} dt \tag{4.33}$$

$$= \int \mathrm{Tr}(\frac{\mathrm{d}\rho(\mathrm{t})}{\mathrm{dt}}\mathrm{H(t)})\mathrm{dt} + \int \mathrm{Tr}(\frac{\mathrm{dH(t)}}{\mathrm{dt}}\rho(\mathrm{t}))\mathrm{dt} \tag{4.34}$$

Ref.[99] defines work and heat as the following

$$W = \int \mathrm{Tr}(\frac{\mathrm{dH(t)}}{\mathrm{dt}}\rho(\mathrm{t}))\mathrm{dt} \tag{4.35}$$

$$Q = \int \mathrm{Tr}(\frac{\mathrm{d}\rho(\mathrm{t})}{\mathrm{dt}}\mathrm{H(t)})\mathrm{dt} \tag{4.36}$$

It is easy to see that for conservative, unitary evolution wherein equation of motion of the state is

$$\frac{d\rho(t)}{dt} = i[\mathrm{H(t)}, \rho(\mathrm{t})] \tag{4.37}$$

Q=0 which we can see from the following

$$
\begin{aligned}
Q &= \int \mathrm{Tr}(\frac{\mathrm{d}\rho(\mathrm{t})}{\mathrm{dt}}\mathrm{H}(\mathrm{t}))\mathrm{dt} && (4.38)\\
&= \int \mathrm{Tr}(\mathrm{i}[\mathrm{H}(\mathrm{t}),\rho(\mathrm{t})]\mathrm{H}(\mathrm{t}))\mathrm{dt} && (4.39)\\
&= \int \mathrm{Tr}(\mathrm{i}[\mathrm{H}(\mathrm{t}),\mathrm{H}(\mathrm{t})]\rho(\mathrm{t}))\mathrm{dt} && (4.40)\\
&= 0 && (4.41)
\end{aligned}
$$

Thus from Eq.4.35 and Eq.4.34 we have from simple conservation of energy $\mathrm{W} = \Delta\langle \mathrm{E}\rangle(\mathrm{t})$. Also by free energy in this work, we will always refer to the Helmholtz free energy which for a thermal state at inverse temperature β is defined as

$$\mathrm{F}(\beta) = -\beta^{-1}\ln(\mathrm{Z}(\beta)) \tag{4.42}$$

where $Z(\beta)$ is the partition function of the system. As we shall see in the next couple of sections that there exists interesting relations between W and $\mathrm{F}(\beta)$ even for non-equilibrium processes through a specific Fluctuation theorem called Jarynski's equality[98].

4.4.2 Jarynski's equality

The statement of the equality[98] is the following:

$$\langle \exp(-\beta\mathrm{W})\rangle = \exp(-\beta\Delta\mathrm{F}(\beta)) \tag{4.43}$$

Several different ways of proving the equality exists[100, 101, 102, 103, 104] however we shall follow the version outlined in Ref.[42] due to Talkner etal. We shall reconstruct the arguments from Ref.[42] herein. The proof uses the following scenario. Let us consider a situation in which the initial density matrix of the system is a thermal state characterized by

$$\rho(0) = \frac{\exp(-\beta\mathrm{H}(0))}{Z(0)} \tag{4.44}$$

where H(0) denotes the Hamiltonian of the system of interest at t=0 and Z(0) is the associated partition function. Let us consider another generalized Hamiltonian dependant on a parameter say $\lambda(t)$ which can be tuned dynamically to attain the following.

$$
\begin{aligned}
\mathrm{H}(\lambda(\mathrm{t}=0)) &= \mathrm{H}(0) && (4.45)\\
\mathrm{H}(\lambda(\mathrm{t}=\tau_{\mathrm{f}})) &= \mathrm{H}(\tau_{\mathrm{f}}) && (4.46)
\end{aligned}
$$

We shall envision the process in which the parameter $\lambda(t)$ is tuned from t=0 to t=τ_f. At t=0 when the initial system was in a thermal state a projective measurement in the eigenbasis of H(0) was made and then let the projected state be $|n\rangle\langle n|$. This state is obtained with probability $\mathrm{P(n,}\beta)$ sampled from the initial thermal distribution. Similarly after the protocol terminates, when the final Hamiltonian is $\mathrm{H(\tau_f)}$, another projective measurement is made which results in the final state say $|m\rangle\langle m|$. Considering the evolution is unitary, then from the definition of work done in the previous section, it is easy to see that

$$\mathrm{W = E_m - E_n} \tag{4.47}$$

$$\mathrm{P(W)} = \sum_{m,n} \delta\mathrm{(W - (E_m - E_n))P(m|n;\tau_f)P(n, beta)} \tag{4.48}$$

where W is the work done on the system and P(W) is the probability of obtaining that value of work. We shall return to Eq.4.48 again (say for example Eq.4.81 with slight modification of the definition of work to make it dimensionless). The meaning of Eq.4.48 is clear. $\mathrm{P(m|n;\tau_f)}$ is the transition probability of collapsing in state $|m\rangle\langle m|$ starting at state $|n\rangle\langle n|$ and P(n, beta) is the probability for sampling that state $|n\rangle\langle n|$ from the thermal distribution. Now for conservative unitary evolution $\mathrm{P(m|n;\tau_f)}$ is given by

$$\begin{aligned}\mathrm{P(m|n;\tau_f)} &= \mathrm{Tr(|m\rangle\langle m|U(\tau_f)|n\rangle\langle n|U(\tau_f)^\dagger)} \\ &= |\langle m|\mathrm{U(\tau_f)|n}\rangle|^2 \end{aligned} \tag{4.49}$$

We will also return to this expression time and again (say Eq.4.76). Now Talkner etal defined a new function G(u) which is the fourier transform of the work distribution as follows

$$\mathrm{G(u)} = \int \mathrm{P(W)\exp(iuW)dW} \tag{4.50}$$

Using Eq.4.50 and Eq.4.47, Eq.4.48 one can arrive at the following

$$\begin{aligned}
\mathrm{G(u)} &= \sum_{m,n} \exp(i(\mathrm{E_m}-\mathrm{E_n})\mathrm{u})\mathrm{P(m|n;\tau_f)P(n,\beta)} \qquad (4.51)\\
&= \sum_{m,n} \exp(i(\mathrm{E_m}-\mathrm{E_n})\mathrm{u})|\langle \mathrm{m}|\mathrm{U}(\tau_\mathrm{f})|\mathrm{n}\rangle|^2\mathrm{P(n,\beta)}\\
&= \sum_{m,n} \exp(i(\mathrm{E_m}-\mathrm{E_n})\mathrm{u})|\langle \mathrm{m}|\mathrm{U}(\tau_\mathrm{f})|\mathrm{n}\rangle|^2\frac{\exp(-\beta\mathrm{E_n})}{\mathrm{Z(0)}} \qquad \because \text{Eq.4.44}\\
&= \sum_{m,n} \exp(i(\mathrm{E_m}-\mathrm{E_n})\mathrm{u})\langle \mathrm{m}|\mathrm{U}(\tau_\mathrm{f})|\mathrm{n}\rangle\langle \mathrm{n}|\mathrm{U}(\tau_\mathrm{f})^\dagger|\mathrm{m}\rangle\frac{\exp(-\beta\mathrm{E_n})}{\mathrm{Z(0)}}\\
&= \sum_{m,n} \langle m|\mathrm{U}(\tau_\mathrm{f})\exp(-\mathrm{iuH(0)})\rho(0)|\mathrm{n}\rangle\langle \mathrm{n}|\mathrm{U}(\tau_\mathrm{f})^\dagger\exp(\mathrm{iuH}(\tau_\mathrm{f}))|\mathrm{m}\rangle\\
&= \sum_{n} \langle n|\mathrm{U}(\tau_\mathrm{f})^\dagger\exp(\mathrm{iuH}(\tau_\mathrm{f}))\mathrm{U}(\tau_\mathrm{f})\exp(-\mathrm{iuH(0)})\rho(0)|\mathrm{n}\rangle \qquad (4.52)\\
&= \mathrm{Tr}(\mathrm{U}(\tau_\mathrm{f})^\dagger\exp(\mathrm{iuH}(\tau_\mathrm{f}))\mathrm{U}(\tau_\mathrm{f})\exp(-\mathrm{iuH(0)}\rho(0))) \qquad (4.53)
\end{aligned}$$

Now from Eq.4.50 if we substitute $u = i\beta$ then

$$\begin{aligned}
\mathrm{G(u=i\beta)} &= \int \mathrm{P(W)}\exp(-\beta\mathrm{W})\mathrm{dW}\\
&= \langle\exp(-\beta\mathrm{W})\rangle \qquad (4.54)
\end{aligned}$$

From Eq.4.53 with $u = i\beta$ we get

$$\begin{aligned}
\mathrm{G(u=i\beta)} &= \mathrm{Tr}(\mathrm{U}(\tau_\mathrm{f})^\dagger\exp(-\beta\mathrm{H}(\tau_\mathrm{f}))\mathrm{U}(\tau_\mathrm{f})\exp(\beta\mathrm{H(0)}\rho(0)))\\
&= \frac{1}{Z(0)}\mathrm{Tr}(\exp(-\beta\mathrm{H}(\tau_\mathrm{f}))\mathrm{U}(\tau_\mathrm{f})\mathrm{U}(\tau_\mathrm{f})^\dagger) \qquad \text{Eq.4.44}\\
&= \frac{Z(\tau_f)}{Z(0)}\\
&= \exp(-\beta(\mathrm{F}(\beta,\tau_\mathrm{f})-\mathrm{F}(\beta,0)))\\
&= \exp(-\beta\Delta\mathrm{F}(\beta)) \qquad (4.55)
\end{aligned}$$

Using Eq.4.54 and Eq.4.55 we complete the proof of the theorem. The theorem has been extended to open systems [105] and to generalized observables too [106, 107].

4.4.3 Central Idea of the Proposal

We propose here an experiment that can allow us to determine the thermal free energy of a crystallized mixed species ion chain, hitherto unexplored, by the application of optical tweezer on a single-species chain alone at various temperatures. At the heart of it, our proposal thus obviates the need to trap a mixed-ion crystal for analyzing its concomitant mechanical properties. The choice of the property to be free energy is motivated by its central character in equilibrium statistical mechanics[108] from which other characteristic features of the system can be evaluated as will be elaborated shortly. The scheme opens up plethora of opportunities for engineering and simulating novel mechanical degrees of freedom that are inaccessible to un-modulated conventional single-species ion chains.

4.4.4 Newness and Utility of the Proposal

The use of optical tweezer in our scheme has many-fold advantage. First the effect of the tweezer can be made to be localized on a single ion on which the beam is being focused. This allows individual control without disturbing neighboring ions. One application of this local control is illustrated in Fig.4.6 wherein we have a chain of 3 ^{171}Yb^{+} ions in an RF/DC induced trapping potential on the extreme left. Use of an optical tweezer on the central ion changes the local trapping strength such that the 3 ^{171}Yb^{+} ion crystal is now mechanically equivalent to a mixed ion crystal of 2 terminal ^{171}Yb^{+} ions and one central ^{133}Ba^{+} ion (shown on extreme right). For such a mixed ion crystal, the central Ba ion anyway feels an enhanced trapping strength due to its higher effective mass even in absence of any optical potential. To replicate this effect using just 3 Yb ions, one can 'pin' the central Yb with an optical tweezer (red-detuned hence trapping in ground state). We shall see that this idea is the cornerstone of our scheme and shall return to it shortly. Also, the potential created by the optical tweezer is dependant on the internal electronic state of the ion unlike in the case of RF/DC. This essentially means that if the ion is excited to other state other than the ground state, the effect of the potential will be different (the potential can even become anti-trapping). The use of optical field for creating a trapping frequency also essentially means better dynamic control and free from RF induced micromotion as discussed in previous chapters. Now let us specifically talk about our scheme. Our protocol relies on the Jarynski's equality[98] for extracting the Free energy change of the target ion specie in its corresponding thermal state at a given temperature. The newness of our proposal is many-fold. Unlike previous experimental work [109] which required changing the mean position of the trapping potential electronically using RF field, ours involves changing the frequency of the trapping potential using an optical tweezer that affords individual local control as discussed. Besides, other proposals were mainly concerned with verification of the Jarynski's equality[109, 110] on a single-specie trapped ion platform. Our proposal on the other hand uses the Jarynski's equality on a conventionally trapped single-specie ion (^{171}Yb^{+} in this case) to compute thermal properties of ion of some other specie (^{133}Ba^{+} in this case) by compensating for the residual trapping strength using optical tweezer. The protocol is useful to the experimental physicists in the ion-trapping community as it can be extended to multiple ions of both single and mixed species too to obtain mode-specific properties. One specific example would be in evaluating mode-specific thermal capacity experimentally. This insight is necessary so as to know the contribution of the various normal modes to motional heating i.e. how much energy is stored within each mode for a given change in their thermal occupation within a time δ_t. With this information it should be possible to specifically target and cool certain modes so that their average occupation stays low.

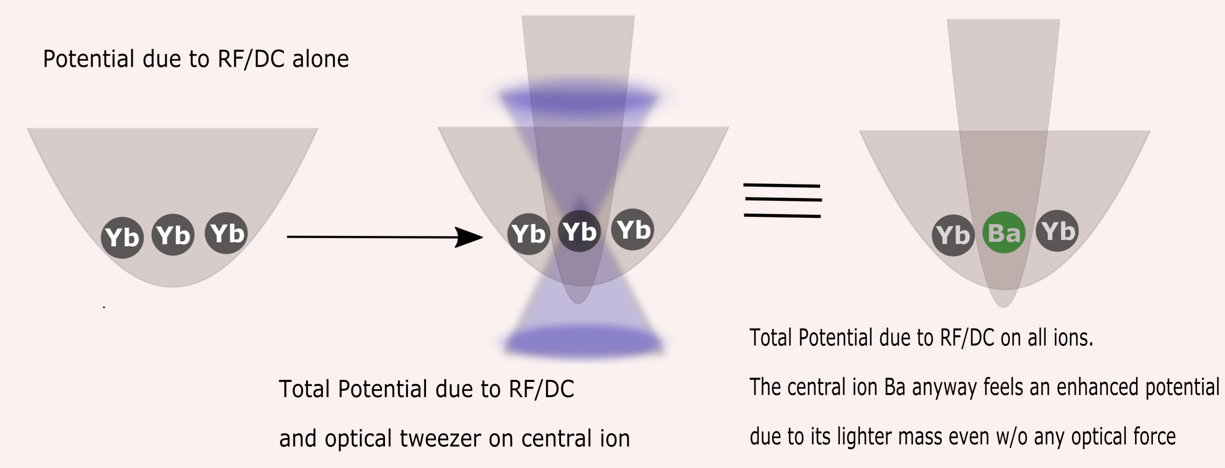

Figure 4.6: The extreme left shows a crystal of 3 ^{171}Yb^{+} ions. Using a red-detuned optical tweezer on the central Yb ion (red-detuned so as to create a confining potential) we can pin the Yb ion and modify the effective potential seen or experienced by this ion. Use of optical tweezer guarantees this local control unlike DC/RF discussed in previous chapter which changes the effective potential experienced by all the ions. It is thus possible to an establish an equivalence (in terms of mechanical frequency dependant properties) between a crystal of 3 ^{171}Yb^{+} ions and between a mixed specie crystal of 2 terminal ^{171}Yb^{+} ions and a central ^{133}Ba^{+} ion (shown on extreme right). The central Ba ion in such a mixed specie crystal anyways feels an enhanced trapping potential even in absence of an optical tweezer due to its mass difference.

4.4.5 Protocol for extracting Free energy for mixed species using single-specie

Using optical tweezers of specific intensity on target ions, the scheme entails modifying the local potential of a single-ion chain so as to compensate for the different effective masses of a mixed-ion chain. As mentioned in the previous two sections, our goal is to compute the mechanical properties of mixed-ion crystals in its thermal state with a single ion crystal alone. The best property to choose from as mentioned before is the free energy as every other equilibrium property of the system (like heat capacity, entropy etc) can be directly obtained from it. A specific example to convert the free energy changes in our scheme to mode-specific equilibrium properties was mentioned in the previous section. Since work done and free energy are intimately related by the Jarynski's equality[98] as proven in a previous section, here we shall thereby elaborate how to obtain the work done in 'converting' (establishing mechanical equivalence only) a single $^{171}\text{Yb}^{+}$ ion into a single $^{133}\text{Ba}^{+}$. The choice of single ion is as a proof of concept demonstration of the idea (note that the thermodynamic protocol is on the phonon distribution which in a given mode can still many even for a single ion) and the choice of 'converting' single-ion crystals to mixed ion crystals is due to the fact that this is achievable only with local control (unlike global controls like DC and RF discussed in previous chapter) and hence have never been attempted in literature before. The following scheme can be experimentally adopted for computing the work done (hence the free energies) for mixed species using single-species trapped ion crystals.

- We use the axial normal mode (labelled as the z-mode) of a single $^{171}\text{Yb}^{+}$ ion for illustration and show how application of optical tweezer can allow us to calculate the properties of the axial-mode of single $^{133}\text{Ba}^{+}$ ion in its thermal state without even trapping the latter. Fig4.7 illustrates the scheme. We start with a conventionally trapped $^{171}\text{Yb}^{+}$ ion using a transverse trapping strength of $\frac{\omega_{x/y}}{2\pi} = 1\text{MHz}$ and an axial trapping strength of $\frac{\omega_z}{2\pi} = \omega_0 = 0.2\text{MHz}$. For electrodynamically trapped ion-apparatus, the trapping frequencies (ω) have an inverse power-law dependance ($\frac{1}{m^s}$) on the inertial mass of the species being trapped[78]. For the transverse mode (along x and y) the pseudopotential created by the radio-frequency is inverse-linear (s=1) whereas for the axial-mode (z), the DC confinement is such that s=0.5. This would mean that the above trapping strengths would be intensified if the $^{171}\text{Yb}^{+}$ ion centre was replaced by a $^{133}\text{Ba}^{+}$ ion by a factor of 1.13 in the axial-direction (z) and 1.28 in the transverse directions (x or y). To modify the curvature of the $^{171}\text{Yb}^{+}$ ion so as to compensate for this differing mass, one can use a red-detuned trapping laser field as has been discussed in the previous sections. The choice of axial-mode (z) for our protocol is justified as its sub-inverse linear dependence mandates lesser optical power to attain the target frequency which in turn minimizes the chance for motional heating due to off-resonant scattering. For the specific case being discussed, we see from Fig4.7 that the intersection with the curve for $\omega_{z,Ba}$ happens for a power P= 0.028 W achieved for a detuning $\delta = 5.8$ nm (red-detuned) created using $\lambda = 375$ nm targeting the $6^2\mathrm{S}_{1/2}$ to $6^2\mathrm{P}_{1/2}$ transition in $^{171}\mathrm{Yb}^+$ ion. The beam spot size used is 1 μm which is conveniently achievable using a NA ≤ 0.5 in a focusing lens system.

- The first step of the protocol involves creation of a Fock-state (labelled by index n henceforth) in the said motional direction in the initially trapped $^{171}\mathrm{Yb}^+$ ion. To achieve this, one can use the scheme in [109]. The idea is to create a thermal state of phonons in the initial trapping potential in the hyperfine ground state $|\mathrm{S}_{1/2}, \mathrm{F}=0, \mathrm{m_F}=0\rangle$. One then performs a carrier transition (defined below) with a Π pulse followed by a blue-side band transition (defined below) with another Π pulse . These transitions are going to shuttle the population of the ion between the hyperfine qubit levels $|\mathrm{S}_{1/2}, \mathrm{F}=0, \mathrm{m_F}=0\rangle$ and $|\mathrm{S}_{1/2}, \mathrm{F}=1, \mathrm{m_F}=0\rangle$ back and forth. Such transitions can be induced by a two-photon Raman process (using the intermediary $\mathrm{P}_{1/2}$ manifold) or by using direct microwave transitions. A carrier transition and a blue-sideband transitions for $^{171}\mathrm{Yb}^+$ ion is defined as the following

$$\begin{aligned}\mathrm{Carrier\ \ \Pi\ \ pulse}: |\mathrm{S}_{1/2}, \mathrm{F}=0, \mathrm{m_F}=0, \mathrm{n}\rangle &\rightarrow |\mathrm{S}_{1/2}, \mathrm{F}=1, \mathrm{m_F}=0, \mathrm{n}\rangle \\ \mathrm{Blue-sideband\ \ \Pi\ \ pulse}: |\mathrm{S}_{1/2}, \mathrm{F}=1, \mathrm{m_F}=0, \mathrm{n}\rangle &\rightarrow |\mathrm{S}_{1/2}, \mathrm{F}=0, \mathrm{m_F}=0, \mathrm{n}-1\rangle \\ &\mathrm{where\ \ n} \in \mathcal{Z}^+\end{aligned}$$

The blue-sideband transition thus would only return the ion to the ground state $|\mathrm{S}_{1/2}, \mathrm{F}=0, \mathrm{m_F}=0\rangle$ and kill a phonon in the process provided there is atleast one phonon to kill in the initial/starting state. In other words if the initial state is $|\mathrm{S}_{1/2}, \mathrm{F}=0, \mathrm{m_F}=0, 0\rangle$ it would be unaffected by the blue-sideband Π pulse and hence would be locked in state $|\mathrm{S}_{1/2}, \mathrm{F}=1, \mathrm{m_F}=0, 0\rangle$ after the initial carrier pulse. Now one can use the detection sequence wherein one turn on a resonant 369.5 nm beam to make the state $|\mathrm{S}_{1/2}, \mathrm{F}=1, \mathrm{m_F}=0\rangle$ transition to state $|\mathrm{P}_{1/2}, \mathrm{F}=1, \mathrm{m_F}=0, \pm 1\rangle$. Since the lifetime of the state $|\mathrm{P}_{1/2}, \mathrm{F}=1, \mathrm{m_F}=0, \pm 1\rangle$ would be of the order of nanoseconds. The ion would decay and in the process fluoresce[83]. The population in state $|\mathrm{S}_{1/2}, \mathrm{F}=0, \mathrm{m_F}=0\rangle$ would not participate in fluorescence due to detuning of 12.6 GHz from the initial exciting beam[83]. Thus detection of fluorescence indicates that the initial state before the starting carrier Π pulse was $|\mathrm{S}_{1/2}, \mathrm{F}=0, \mathrm{m_F}=0, 0\rangle$. If the state from the thermal state projected is an arbitrary Fock state like $|\mathrm{S}_{1/2}, \mathrm{F}=0, \mathrm{m_F}=0, \mathrm{n}\rangle$ then it would take n cycles of carrier

+ blue-sideband pulses to kill all phonons in it and make the ion reside in state $|\mathrm{S}_{1/2}, \mathrm{F} = 0, \mathrm{m_F} = 0, 0\rangle$. At the n+1 th step fluorescence will be detected. After knowing this value of n one can now deterministically prepare the state $|\mathrm{S}_{1/2}, \mathrm{F} = 0, \mathrm{m_F} = 0, \mathrm{n}\rangle$ by repeated application of blue-sideband + carrier transition (note reversal in order which actually now creates a phonon in the ground hyperfine state) n times. This will be the beginning Fock state of the protocol. The entire protocol is described in detail in [109] (see Fig. 3 in the reference)

- Starting with the Fock state in the initial trapping potential we raise the optical power using a red-detuned optical tweezer ($\delta = 5.8$ nm, red-detuned) on the ion until the target strength is reached. In our case to achieve the trapping strength of a single $^{133}\mathrm{Ba}^{+}$ we will have to change the optical power from P=0 to P=0.028 W within a switching time τ_f. Thereafter following the same protocol of state-determination as discussed in the previous point [109] on the final Hamiltonian attained one can project the final state on a Fock state (hereafter indexed by m).
- Work (W) performed on the system will be difference of the energy of the finally projected state and the initial starting state $(\mathrm{E_m} - \mathrm{E_n})$.
- To construct the probability distribution of attaining this value of work, the entire experiment will have to be repeated many times with different switching times τ_f (relative to ω_{τ_f}) and sampling different initial states $|n\rangle\langle n|$ from the thermal distribution characteristic of β. Due to quantum fluctuation the projected state of the final Hamiltonian may be different. The entire sequence of experiment will have to repeated now for various initial inverse temperatures β which will affect the sampling distribution for the initial state.

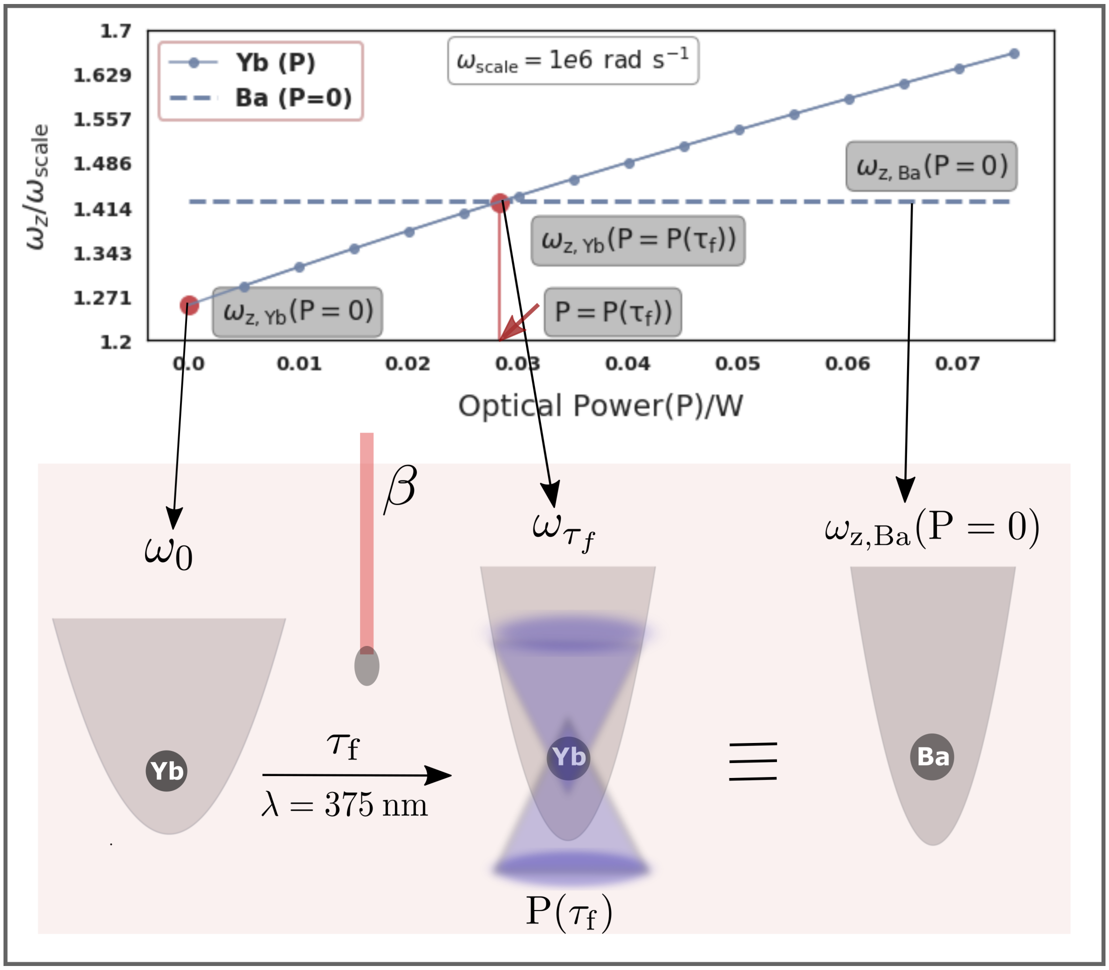

Figure 4.7: The scheme explaining the protocol for obtaining the thermal free energy change $\Delta F(\beta)$ as a function of inverse temperature β. We start with a trapped ^{171}Yb$^+$ ion trapped conventionally by using a combination of DC and RF field as described in previous chapter. Let the trapping frequencies in the transverse directions (x,y) be $\frac{\omega_{x,Yb}}{2\pi}$ = 1 MHz, $\frac{\omega_{y,Yb}}{2\pi}$ = 1 MHz whereas the trapping strength in the axial z-direction $\frac{\omega_{x,Yb}}{2\pi} = 0.2$ MHz. For us the axial trapping strength is important. In the same trap is if ^{133}Ba$^+$ were to be trapped the corresponding trapping frequencies would be $\frac{\omega_{x,Yb}}{2\pi} = 1.28$ MHz , $\frac{\omega_{y,Yb}}{2\pi} = 1.28$ MHz and $\frac{\omega_{y,Yb}}{2\pi} = 0.226$ MHz due to the differing mass. The figure shows that for an optical tweezer of power $\text{P}(\tau_f) = 0.028$ W on the ^{171}Yb$^+$ ion one can compensate for the residual trapping strength and make the trapped ^{171}Yb$^+$ ion 'behave' equivalent to that of a ^{133}Ba$^+$ ion in terms of mechanical properties along z-direction. Turning the optical tweezer on to the said power dynamically at a variable switching rate τ_f and temperature β can allow us to compute thermal properties of ^{133}Ba$^+$ ion without even trapping it in the first place (see protocol). Note that the figure displays the z-trapping strength in rad/s with the 2π factor built in.

4.4.6 Results of Simulation

4.4.6.1 Simulation of the Hamiltonian- generator of the time translation for the dynamics

As described above, we start with the axial (z) directional motional mode of a single-trapped $^{171}\mathrm{Yb}^{+}$ ion. We shall then change the motional-frequency of that mode by using the optical tweezer as described in the previous section. Our protocol thus requires the simulation of dynamics generated by the undermentioned Hamiltonian.

$$\mathrm{H(t)} = \frac{\mathrm{p_z^2}}{2\mathrm{m}} + \frac{\mathrm{m}\omega_{\mathrm{z}}(\mathrm{t})^2(\mathrm{z}-\mathrm{z_0})^2}{2} \tag{4.56}$$

In the above equation, m is the mass of the trapped $^{171}\mathrm{Yb}^{+}$ ion, $\mathrm{p_z}$ is its linear momentum, $(\mathrm{z}-\mathrm{z_0})$ is the displacement of the ion relative to the mean-position $\mathrm{z_0}$ and $\omega_z(t)$ is the time-dependant z-directional motional trapping frequency which is varied using the optical tweezer. $\omega_z(t)$ will have to satisfy the following properties.

$$\omega_z(t) = \omega_0 = \omega_{z\mathrm{Yb}}(\mathrm{P}=0) \qquad \mathrm{t}=0$$

$$\begin{aligned}\omega_z(t) = \omega_{\tau_f} &= \omega_{z\mathrm{Yb}}(\mathrm{P}=\mathrm{P}(\tau_{\mathrm{f}}))\\ &= \omega_{z\mathrm{Ba}}(\mathrm{P}=0) \qquad\qquad \mathrm{t}=\tau_{\mathrm{f}}\end{aligned}$$

To express the Hamiltonian in Eq.4.56 in second-quantization, let us define the following operators

$$\begin{aligned}\mathrm{b} &= \sqrt{\frac{m\omega_0}{2\hbar}}(\mathrm{z}-\mathrm{z_0}) + \frac{\mathrm{ip_z}}{\sqrt{2\mathrm{m}\omega_0\hbar}}\\ \mathrm{b}^\dagger &= \sqrt{\frac{m\omega_0}{2\hbar}}(\mathrm{z}-\mathrm{z_0}) - \frac{\mathrm{ip_z}}{\sqrt{2\mathrm{m}\omega_0\hbar}}\end{aligned}$$

Note that the operators b, $\mathrm{b}^\dagger$ are defined in terms of ω_0 and not any $\omega(t)$. Substituting the operators p_z, $\mathrm{z_{z0}}$ in terms of operators b, $\mathrm{b}^\dagger$ into Eq.4.56 we get the following expression.

$$\mathrm{H(t)} = \frac{\hbar\omega(\mathrm{t})}{2}\left(\frac{\omega(\mathrm{t})}{\omega_0} - \frac{\omega_0}{\omega(\mathrm{t})}\right)(\mathrm{b}^2 + \mathrm{b}^{\dagger 2}) + \frac{\hbar\omega(\mathrm{t})}{2}\left(\frac{\omega(\mathrm{t})}{\omega_0} + \frac{\omega_0}{\omega(\mathrm{t})}\right)(\mathrm{bb}^\dagger + \mathrm{b}^\dagger\mathrm{b}) \tag{4.57}$$

To tidy Eq.4.57 one can define,

$$\mathrm{r(t)} = \frac{\ln(\frac{\omega(\mathrm{t})}{\omega_0})}{2} \tag{4.58}$$

With this definition we get

$$
\begin{aligned}
\mathrm{Cosh}(2\mathrm{r}(\mathrm{t})) &= \frac{\exp(2r(t)) + \exp(-2r(t))}{2} \\
&= \frac{1}{2}(\frac{\omega(t)}{\omega_0} + \frac{\omega_0}{\omega(t)}) \\
\mathrm{Sinh}(2\mathrm{r}(\mathrm{t})) &= \frac{\exp(2r(t)) - \exp(-2r(t))}{2} \\
&= \frac{1}{2}(\frac{\omega(t)}{\omega_0} - \frac{\omega_0}{\omega(t)})
\end{aligned}
$$

Thus the Hamiltonian in Eq.4.57 simplifies to

$$\mathrm{H}(\mathrm{t}) = \hbar\omega(\mathrm{t})\mathrm{Sinh}(2\mathrm{r}(\mathrm{t}))(\mathrm{b}^2 + \mathrm{b}^{\dagger 2}) + \hbar\omega(\mathrm{t})\mathrm{Cosh}(2\mathrm{r}(\mathrm{t}))(\mathrm{b}\mathrm{b}^\dagger + \mathrm{b}^\dagger\mathrm{b}) \tag{4.59}$$

Note that the Hamiltonian in Eq.4.59 is expressed entirely in terms of operators b and $\mathrm{b}^\dagger$ and hence can be resolved in the eigenbasis of the initial Hamiltonian at t=0. Let the two specific eigenvectors of this Hamiltonian at t=0 be labelled as $|\mathrm{n}\rangle$ and $|\mathrm{n}'\rangle$. Then using Eq.4.59, the Hamiltonian matrix elements used in the simulation is

$$\langle n'|\mathrm{H}(\mathrm{t})|\mathrm{n}\rangle = \sqrt{\mathrm{n}(\mathrm{n}-1)}\delta_{\mathrm{n}',\mathrm{n}-2} + \sqrt{(\mathrm{n}+1)(\mathrm{n}+2)}\delta_{\mathrm{n}',\mathrm{n}+2} + 2(\mathrm{n} + \frac{1}{2})\delta_{\mathrm{n}',\mathrm{n}} \tag{4.60}$$

The only thing which needs to be explicated at this point is what should be the upper limit to $|\mathrm{n}\rangle$. Theoretically n is lower bounded to 0 but there is no strict upper bound. However in a numerical simulation one has to construct finite-dimensional matrices and hence one needs to chose an upper bound to n. We choose an upper bound of $\mathrm{n}_{\mathrm{max}} = 67$. This choice is 10 times the $\langle \mathrm{n}\rangle_{\mathrm{act}}$ at the highest temperature used for our simulation at the initial frequency (ω_0) which is lowest of all frequencies encountered during time evolution. The highest temperature chosen in our simulation is 0.3 mK and the lowest is 0.1 mK. With $\mathrm{n}_{\mathrm{max}} = 67$, $\langle n\rangle_{sim}$ matches the $\langle n\rangle_{act}$ to 5 decimal places at all temperatures.

4.4.6.2 Simulation of the dynamics

We use the expression for H(t) given in Eq.4.59, to simulate the dynamics of the system using the following channel for the density matrix.

$$\rho(t) = \mathrm{U}(\mathrm{t}, 0; \tau_{\mathrm{f}})\rho(0)\mathrm{U}(\mathrm{t}, 0; \tau_{\mathrm{f}})^\dagger \tag{4.61}$$

One can choose $\rho(0)$ to be a Fock state in the initial Hamiltonian designated as $|n\rangle\langle n|$. In Eq.4.61 the equation of motion for U(t,0;τ_f) is

$$\frac{d\mathrm{U}(\mathrm{t},0,;\tau_\mathrm{f})}{dt} = -i\mathrm{H}(\mathrm{t})\mathrm{U}(\mathrm{t},0,;\tau_\mathrm{f}) \tag{4.62}$$

U(0,0;τ_f) $= \mathcal{I}$. The following quantities are then computed from the dynamics.

- Motional excitations and conditional probability P(m|n, τ_f). To compute this quantity one projects the expression for the final state in Eq.4.61 in the eigenbasis of the final Hamiltonian. Let the projector for the eigenbasis for the finally attained Hamiltonian be $|m\rangle\langle m|$, then the probability for cross excitation P(m|n, τ_f) is defined as

  $$\mathrm{P}(\mathrm{m}|\mathrm{n},\tau_\mathrm{f}) = \mathrm{Tr}(|\mathrm{m}\rangle\langle\mathrm{m}|\rho(\mathrm{t})) \tag{4.63}$$

  One has to now repeat the calculation for many different choices of initial and final states and for different choices of τ_f

- The work done in the process will be counted from the energy change as

  $$\begin{aligned}\mathrm{W} = \frac{\tilde{\mathrm{E}}_\mathrm{m} - \mathrm{E}_\mathrm{n}}{\hbar\omega_0} &= (m+0.5)\frac{\omega_{\tau_f}}{\omega_0} - (n+0.5) \\ &= \frac{\omega_{\tau_f}}{\omega_0}\mathrm{m} - \mathrm{n} + 0.5(\frac{\omega_{\tau_\mathrm{f}}}{\omega_0} - 1)\end{aligned} \tag{4.64}$$

- The work distribution P(W) is then computed from P(m|n, τ_f) using the following expression

  $$\mathrm{P}(\mathrm{W};\tau_\mathrm{f}) = \sum_{\mathrm{m,n}} \mathrm{P}(\mathrm{m}|\mathrm{n},\tau_\mathrm{f})\mathrm{P}(\mathrm{n},\beta)\ \delta(\mathrm{W} - (\frac{\tilde{\mathrm{E}}_\mathrm{m} - \mathrm{E}_\mathrm{n}}{\hbar\omega_0})) \tag{4.65}$$

where $\mathrm{P}(\mathrm{n},\beta)$ is the probability for sampling an initial state characteristic of an inverse temperature β. In next few sections, we shall elaborate on each of these quantities and show computational results.

4.4.6.3 Motional excitations and conditional probability P(m|n,τ_f)

Figure4.8 shows the scheme for cross-excitation starting from a given initial state (say n=2) in the starting Hamiltonian with frequency ω_0 to various nearby states of the final Hamiltonian indexed by m=n, m=n+2, m=n-2 etc. These transition probabilties are P(m|n;τ_f). This probability is parametrically dependant on the switching time τ_f. Transitions to m$\neq$n are more for a switching event with smaller τ_f but low otherwise. To appreciate this point, we have to resort to adiabatic theorem [111, 112, 113]. This can also be established semi-classically. From Hamiltonian dynamics one can easily recall that the action integral ($\oint$ pdq) is an adiabatic invariant quantity if the temporal rate of change of the parameters within the Hamiltonian is slower than the time scale of the internal dynamics of the system[112]. From the phase-space representation of the dynamics, it is easy to see that $\oint$ pdq is the overall area under the $\mathrm{p-q}$ curve representing the trajectory of the system. Since, the phase space trajectory of a harmonic oscillator is an ellipse the overall area under the ellipse is proportional to the energy (E(t)/ω(t)) directly. Hence adiabatic invariance of the area implies (E(t)/ω(t)) would be a constant of motion for all times 't'. The semi-classical part kicks in if we replace E(t) with $\hbar\omega(t)$(n$+$0.5), then we immediately see that n is a constant of motion for $\forall$ t i.e. the final state of the system under these conditions would be m=n after t = $\mathrm{\tau_f}$. However, a more rigorous quantum version of the proof would be instructive and we will follow the treatment given in Ref [111].

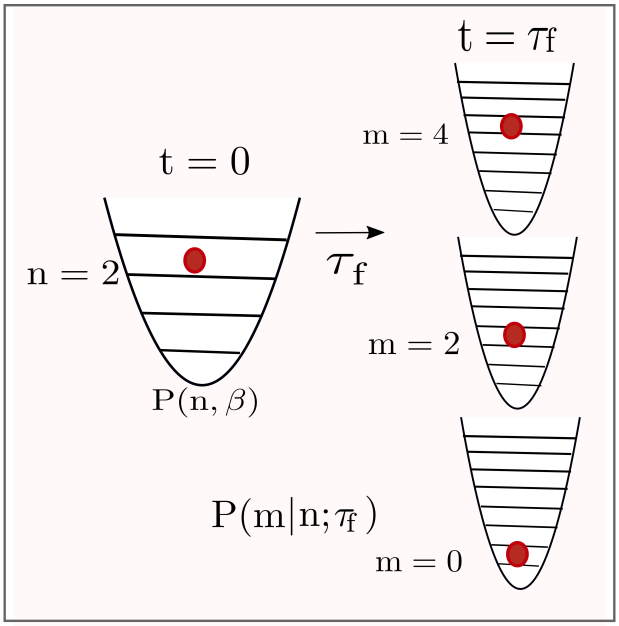

Figure 4.8: The scheme for cross-excitation starting with an initial motional frequency ($\frac{\omega_0}{2\pi}$ = 0.2 MHz) and terminating the protocol at a final frequency ($\frac{\omega_{\tau_f}}{2\pi}$ = 0.226 MHz). P(m|n; τ_f) denotes the cross-excitation for the phonon (marked in red circle) from an initial state of n=2 to a final state of m=0,2,4. The text describes why the switching time τ_f is important in ascertaining which final state will be attained. It also explains the selection rule for a transition from an even-valued n to an even-valued m exclusively.

Let us consider a situation in which we interpolate between a series of generalized Hamiltonians defined by the set σ_{H} characterized by $s = \mathrm{t}/\tau_{\mathrm{f}}$

$$\sigma_{\mathrm{H}} = \{\mathrm{H(s)} \mid \mathrm{H(s)} \ \epsilon \ \mathcal{H}_{\mathrm{n}}, \mathrm{s} \ \epsilon \ [0,1]\} \tag{4.66}$$

Since $\mathcal{H}_n$ corresponds to the space of Hermitian matrices, each of the operators in the set σ_{H} is diagonalizable and hence has an associated spectrum.

$$\mathrm{H(s)}\tilde{\rho}^{\alpha}(\mathrm{s}) = \mathrm{E}_{\alpha}\tilde{\rho}^{\alpha}(\mathrm{s}) \tag{4.67}$$

where $\tilde{\rho}^{\alpha}(s)$ is the eigen-projector onto state indexed by α and E_{α} is the associated energy. The central goal of adiabatic theorem is to express $||\rho(s) - \tilde{\rho}^{\alpha}(s)||$ where $\rho(s)$ is the instantaneous state of the system obtained during the time evolution with the initial condition that $\rho(0) = \tilde{\rho}^{\alpha}(0)$ and determine under what conditions is this L2 norm minimal. We shall compute the cross-excitations between state $\tilde{\rho}^{\alpha}(s)$ and $\tilde{\rho}^{\alpha\prime}(s)$ as a function of switching rate $1/\tau_f$. In our model where the initial and final states are labelled by n and m respectively, this will be P(m|n; τ_f). We shall see what the switching rate $1/\tau_f$ should be to reduce/amplify these cross-excitations. The (i,j)th element of the density operator ($\rho_{ij}(s)$) specifying the instantaneous state evolves according to Liouville Von-Neumann equation as follows.

$$\begin{aligned}\frac{d\rho_{ij}(s)}{ds} &= i\tau_f \sum_k (H(s)_{ik}\delta_{lj} - \delta_{ik}H(s)_{lj})\rho_{kl}(s) \\ &= i\tau_f \sum_{k,l} L_{ij,kl}\rho_{kl}(s) \end{aligned} \tag{4.68}$$

Let us the dimension of the system be N i.e. $\rho(s)$ is an $N \times N$ matrix. One can vectorize this matrix and consider $\rho(s)_{ij}$ to be a component of a vector of dimension N^2. Note in Eq.4.68 , $L_{ij,kl}$ is a $N^2 \times N^2$ matrix as each of the four indices (i,j,k,l) characterizing it runs from 1,2....N. Thus in the language of exterior algebra $L = H \wedge \mathcal{I}$. Now let us consider the diagonal form of the matrix $L_{ij,kl}$

$$\sum_{k,l} L_{ij,kl}\rho^{\alpha}_{kl}(s) = l(s)\rho^{\alpha}_{ij}(s) \tag{4.69}$$

Ref[111] (and Ref[18] in Ref[111]) clarifies that if $L_{ij,kl}$ is a normal matrix (matrix commuting with its adjoint) then its corresponding eigenvectors can be orthogonalized. The $L_{ij,kl}$ from Eq.4.68 is normal as its wedge product of two normal matrices (H and $\mathcal{I}$ respectively). Since the number of eigenvectors will be N^2 (as the matrix is $N^2 \times N^2$ dimensional) so together with orthogonality it forms a complete set and hence it is possible to express the (i,j) th element of an arbitrary density matrix $\rho(s)$ in terms of the i,j the element eigenmode set ρ^{α}_{ij} of $L_{ij,kl}$ as an ansatz as follows

Eq.4.67 as follows:

$$\rho_{ij}(s) = \sum_{\alpha} C^{\alpha}(s)\rho^{\alpha}_{ij}(s)\exp(\tau_f \int^1 \mathrm{E}_{\alpha}(\mathrm{s})\mathrm{ds}) \tag{4.70}$$

Using the arguments in Ref.[111], we appear at the following equation for the time-evolution of $C^{\alpha}(s)$ which is the reason for the cross-excitations in the first place.

$$\frac{dC^{\beta}(s)}{ds} = \sum_{\alpha} C^{\alpha}(s)\frac{\langle \rho^{\beta}(s)|\partial_s L|\rho^{\beta}(s)\rangle}{\tau_f(\mathrm{E}_{\beta}(\mathrm{s}) - \mathrm{E}_{\alpha}(\mathrm{s}))}\exp(\tau_f \int^1 \mathrm{E}_{\alpha}(\mathrm{s}) - \mathrm{E}_{\beta}(\mathrm{s})\ \mathrm{ds}) \tag{4.71}$$

Several points are apparent from Eq.4.71. They are

- We see from the Eq.4.71, that the time-evolution of $C^{\alpha}(s)$ can be reduced to zero if the term $\frac{\langle\rho^{\beta}(s)|\partial_s L|\rho^{\beta}(s)\rangle}{\tau_f(\mathrm{E}_{\beta}(\mathrm{s})-\mathrm{E}_{\alpha}(\mathrm{s}))}$ kept very small. In that scenario $\frac{dC^{\beta}(s)}{ds} \approx 0$ and hence $C^{\alpha}(s) \approx C^{\alpha}(0)\ \forall\ \alpha$. So we see that quantum index of the state would remain a constant of motion (like the semi-classical treatment above).

- Since from Eq.4.70, the absolute magnitude of $C^{\alpha}(s)$ is $\mathcal{O}(1)$ to preserve normalization of the instantaneous density matrices, we can assume that a safe metric for the term would be $\frac{\langle\rho^{\beta}(s)|\partial_s L|\rho^{\beta}(s)\rangle}{\tau_f(\mathrm{E}_{\beta}(\mathrm{s})-\mathrm{E}_{\alpha}(\mathrm{s}))} \leq 1$ [112]. This automatically gives us a restriction on the switching time as

$$\begin{aligned}\frac{\langle\rho^{\beta}(s)|\partial_s L|\rho^{\beta}(s)\rangle}{\tau_f(\mathrm{E}_{\beta}(\mathrm{s})-\mathrm{E}_{\alpha}(\mathrm{s}))} &\leq 1 \\ \tau_f \geq \frac{\langle\rho^{\beta}(s)|\partial_s L|\rho^{\beta}(s)\rangle}{\mathrm{E}_{\beta}(\mathrm{s})-\mathrm{E}_{\alpha}(\mathrm{s})} & \qquad (4.72)\end{aligned}$$

- It is easy to see why maximizing the switching time τ_f (minimizing switching rate) might pose an issue for H(s) wherein the spectral gap between the states may be zero (degeneracy) $\mathrm{E}_{\beta}(\mathrm{s})-\mathrm{E}_{\alpha}(\mathrm{s}) \approx 0$. Indeed the breakdown of the adiabatic approximation under such cases has been discussed at length in [112].

- This also stands to reason why our choice of switching time (τ_f) to be $\geq \frac{1}{\omega_0}$ would expected to mimic the adiabatic transition closely. This is because in the transformation proposed ω_t is increasing continuously with time. So the smallest energy gap would be when $t = 0$ i.e. for the initial state for which $\omega_t = \omega_0$. So choosing a switching time bigger than inverse of ω_0 would be slower than the slowest dynamics in the whole trajectory.

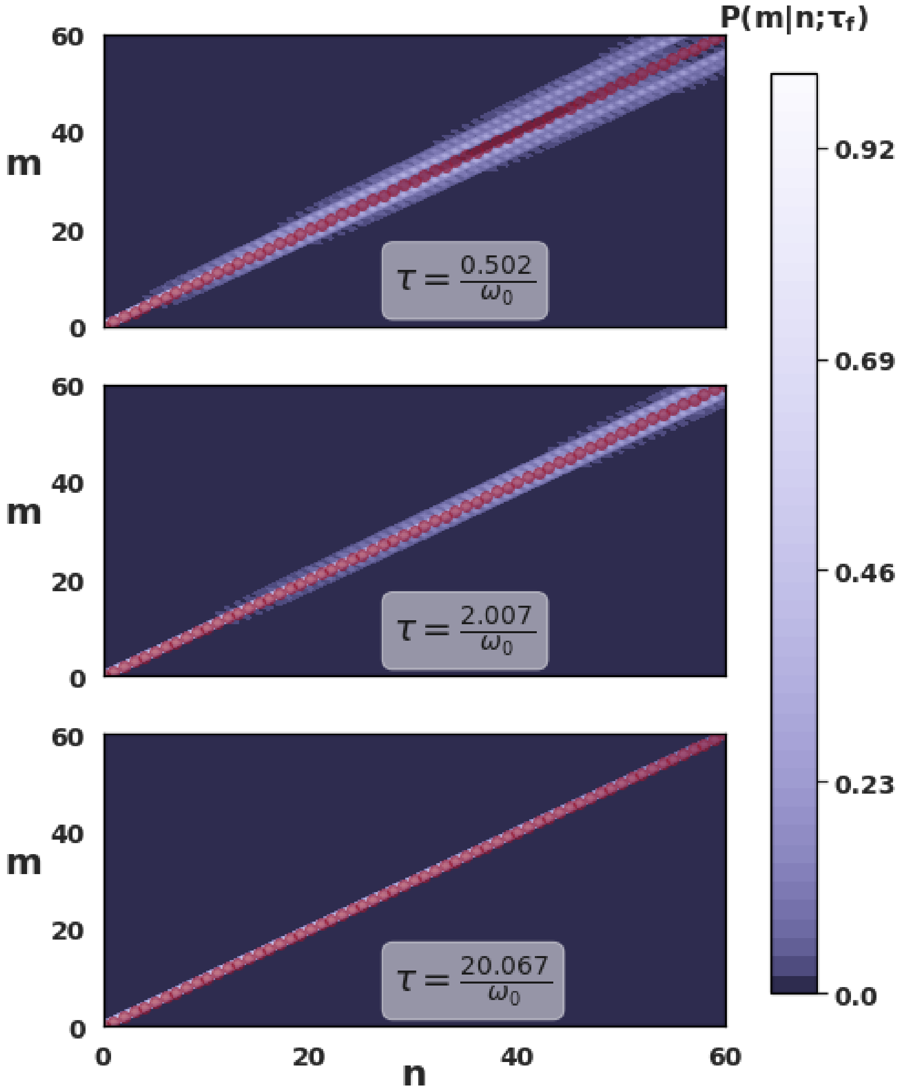

)

Figure 4.9: The P(m|n; τ_f) distribution for all values of (m,n) ($(n_{max}, m_{max}) \leq 60$) . The distribution is plotted for three different values of τ_f. $\tau_f = 0.5/\omega_0$ corresponds to the non-adiabatic limit wherein cross-excitations are predominant i.e. excitation into m near n along the diagonal are seen. $\tau_f = 20/\omega_0$ is the adiabatic limit wherein the transition probability is non-zero for m=n only along the diagonal. $\tau_f = 2/\omega_0$ is a point in between showing continuity of the transition. The diagonal elements are marked in red. The initial frequency is $\frac{\omega_0}{2\pi} = 0.200$ MHz and final terminal frequency is $\frac{\omega_{\tau_f}}{2\pi} = 0.226$ MHz

Fig.4.9 shows the plot of these transition amplitudes (P(m|n; τ_f) against all values of m and n for m,n $\leq$ 60. We see this plotted for two different switching times (τ_f). We see that for $\tau_f \leq \frac{1}{\omega_0}$, P(m|n; τ_f) for a given n is also non-zero for values of m near that n i.e. close to diagonal. In line with our expectation, the values of P(m| n) for case of $\tau_f \geq \frac{1}{\omega_0}$ has appreciable value only along the diagonal and is nearly zero elsewhere. A second more important observation can be made from Fig.4.10 and seen more clearly from Fig.4.11 is that for a given n, the transition occurs to only values of m which are of the same parity. In other words, P(m|n; τ_f) is non-zero for a given n iff m+n=2k $\forall\ \ k \in \{0, 1, 2, 3...\}$ i.e. both m and n are either even or both are odd. This can be best appreciated from the fact that parity is a conserved quantity of the transformation as proven below.
Let us define an operator Π such that

$$\Pi|n\rangle = (-1)^n|n\rangle \tag{4.73}$$

Using Eq.4.73 the following properties about bosonic-creation and anihilation operators can be verified easily

$$\begin{aligned} \Pi \mathrm{b} \Pi^\dagger &= -\mathrm{b} \\ \Pi \mathrm{b}^\dagger \Pi^\dagger &= -\mathrm{b}^\dagger \end{aligned} \tag{4.74}$$

Using Eq.4.74 and Eq.4.59 one can deduce the following

$$\begin{aligned} \Pi \mathrm{H(t)} \Pi^\dagger &= \Pi(\hbar\omega(t)\mathrm{Sinh(2r(t))(b^2 + b^{\dagger 2})} + \hbar\omega\mathrm{(t)Cosh(2r(t))(bb^\dagger + b^\dagger b))}\Pi^\dagger \\ &= \hbar\omega(t)\mathrm{Sinh(2r(t))}(\Pi \mathrm{b}^2\Pi^\dagger + \Pi \mathrm{b}^{\dagger 2}\Pi^\dagger) + \hbar\omega\mathrm{(t)Cosh(2r(t))}(\Pi \mathrm{bb}^\dagger\Pi^\dagger + \Pi \mathrm{b}^\dagger \mathrm{b}\Pi^\dagger) \\ &= \hbar\omega(t)\mathrm{Sinh(2r(t))}(\Pi \mathrm{b}\Pi^\dagger\Pi \mathrm{b}\Pi^\dagger + \Pi \mathrm{b}^\dagger\Pi^\dagger\Pi \mathrm{b}^\dagger\Pi^\dagger) \\ &+ \hbar\omega(t)\mathrm{Cosh(2r(t))}(\Pi \mathrm{b}\Pi^\dagger\Pi \mathrm{b}^\dagger\Pi^\dagger + \Pi \mathrm{b}^\dagger\Pi^\dagger\Pi \mathrm{b}\Pi^\dagger) \\ &= \hbar\omega(t)\mathrm{Sinh(2r(t))(b^2 + b^{\dagger 2})} + \hbar\omega\mathrm{(t)Cosh(2r(t))(bb^\dagger + b^\dagger b)} \qquad \because \text{Eq.4.74} \\ &= \mathrm{H(t)} \end{aligned} \tag{4.75}$$

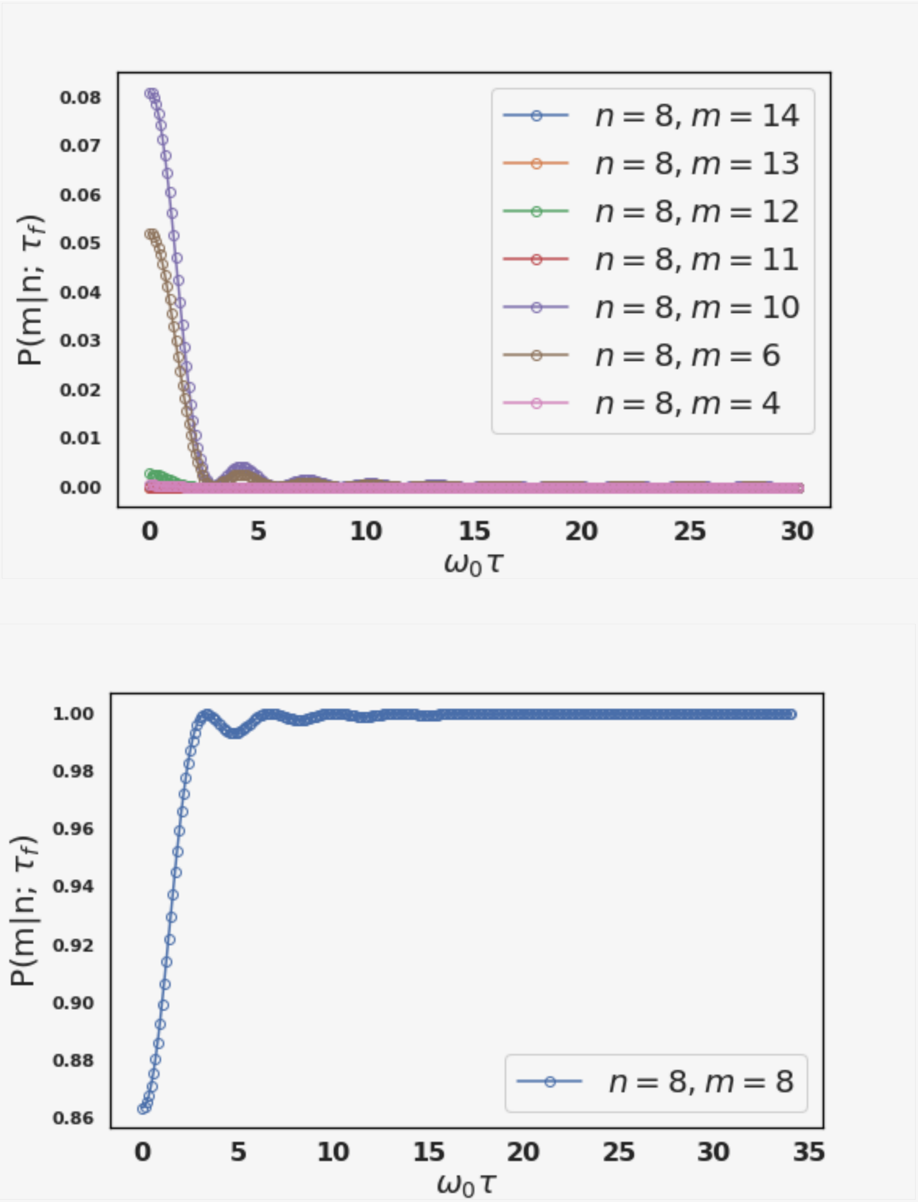

Figure 4.10: The P(m|n; τ_f) distribution for all values of switching time τ_f for different (n,m) pairs. Apart from transition to m$\neq$ n for non-adiabatic switching at low τ_f, the plot also demonstrates that $\mathrm{P(m|n;\tau_f) = 0}$ if $\mathrm{(m+n)} \neq 2\mathrm{k}\ \forall \mathrm{k} \in \{0,1,2,3...\}$. At high τ_f transition to n=m=8 is absolutely certain. The initial frequency is $\frac{\omega_0}{2\pi} = 0.200$ MHz and final terminal frequency is $\frac{\omega_{\tau_f}}{2\pi} = 0.226$ MHz

$$
\begin{aligned}
\mathrm{P(m|n,\tau_f)} &= \mathrm{Tr(|m\rangle\langle m|U(t,0;\tau_f)\rho(0)U(t,0;\tau_f)^\dagger)} && (4.76)\\
&= \mathrm{Tr(|m\rangle\langle m|U(t,0;\tau_f)|n\rangle\langle n|U(t,0;\tau_f)^\dagger)}\\
&= \mathrm{Tr(|m\rangle\langle m|U(t,0;\tau_f)|n\rangle\langle n|U(t,0;\tau_f)^\dagger)}\\
&= \mathrm{Tr(|m\rangle\langle m|f(H(t),t)|n\rangle\langle n|f(H(t),t)^\dagger)} \qquad \because \mathrm{U(t,0;\tau_f) = f(H(t),t;\tau_f)} \text{ as evolution is unitary}\\
&= \mathrm{\langle m|f(H(t),t)|n\rangle\langle n|f(H(t),t)^\dagger|m\rangle}\\
&= \mathrm{|\langle m|f(H(t),t)|n\rangle|^2} && (4.77)
\end{aligned}
$$

Now that we have explicitly written $\mathrm{P(m|n,\tau_f)}$ in Eq.4.77, let us see what Eq.4.75 can tell us about the magnitude of this quantity.

$$
\begin{aligned}
\mathrm{\langle m|f(H(t),t)|n\rangle} &= \mathrm{\langle m|\Pi f(H(t),t)\Pi^\dagger|n\rangle} \qquad \because \text{Eq.4.75}\\
&= \mathrm{\langle m|\Pi f(H(t),t)\Pi|n\rangle} \qquad \because \Pi^\dagger = \Pi\\
&= \mathrm{(-1)^{m+n}\langle m|f(H(t),t)|n\rangle} && (4.78)
\end{aligned}
$$

From Eq.4.78, it is apparent that

$$\mathrm{\langle m|f(H(t),t)|n\rangle = 0 \quad if \ (m+n) \ \neq 2k \ \forall k \ \in \ \{0,1,2,3...\}} \tag{4.79}$$

Thus combining Eq.4.79 and Eq.4.77 it is clear that

$$\mathrm{P(m|n;\tau_f) = 0 \quad if \ (m+n) \ \neq 2k \ \forall k \ \in \ \{0,1,2,3...\}} \tag{4.80}$$

This establishes that the dynamic evolution of our Hamiltonian has parity allowed selection rules i.e. transitions of particular parity are only allowed. If one starts with an n which is even(odd), then one can only get an m which is also even(odd) at the end of the protocol.

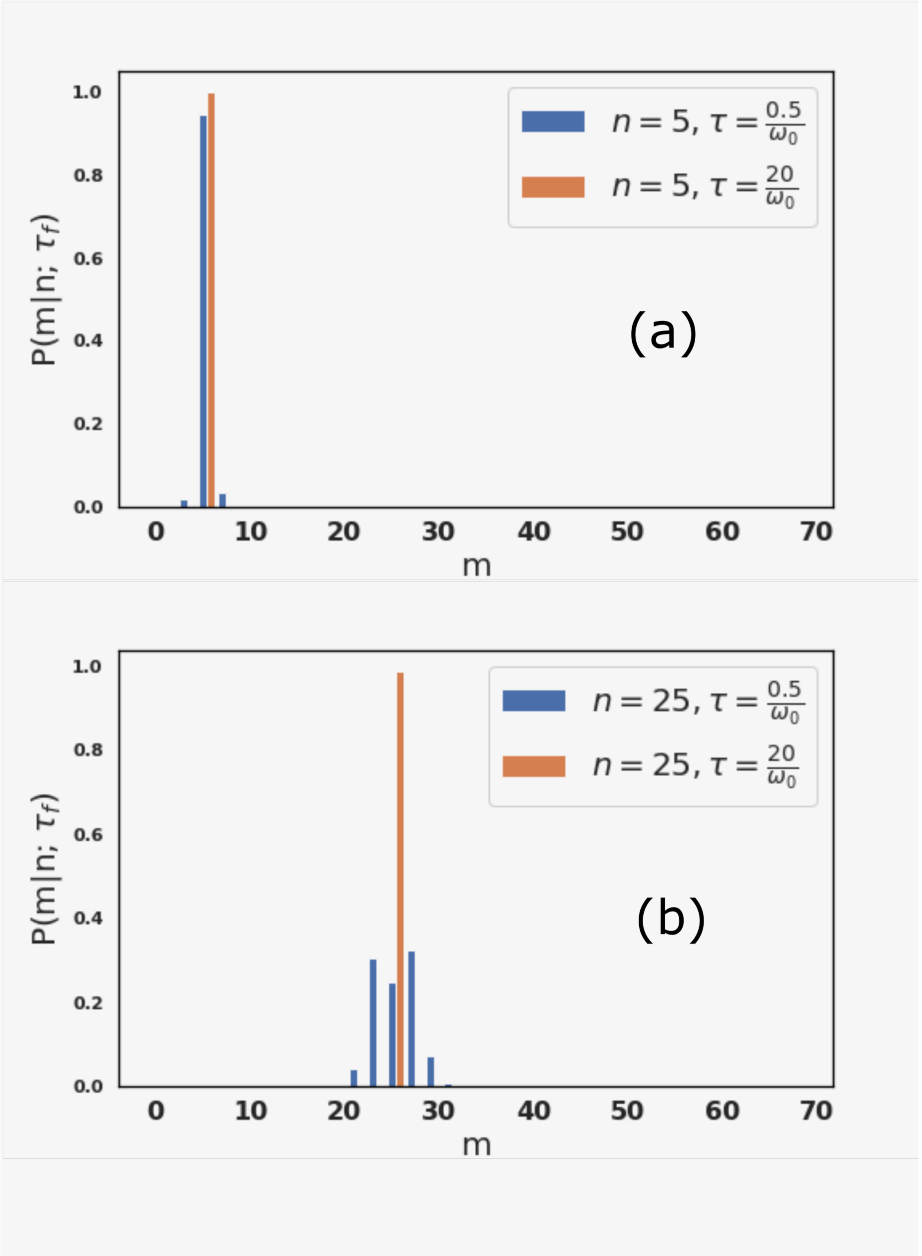

Figure 4.11: The P(m|n; τ_f) distribution for all values of m ($m_{max} < 67$) for (a) n=5, (b) n=25. The bars(blue) corresponds to transition in non-adiabatic limit and the bars(orange) corresponds to the case in the adiabatic limit. The orange bars are shifted by 1.00 for better visualization. The plot also shows $\mathrm{P(m|n;}\tau_\mathrm{f}) = 0 \quad \text{if} \ (\mathrm{m+n}) \neq 2\mathrm{k} \ \forall \mathrm{k} \in \{0, 1, 2, 3...\}$ and also highlights that in the non-adiabatic case the transitions are more pronounced for higher n than starting at a low n. The initial frequency is $\frac{\omega_0}{2\pi} = 0.200$ MHz and final terminal frequency is $\frac{\omega_{\tau_f}}{2\pi} = 0.226$ MHz

The last point which needs to be stressed based on Fig.4.11 is that for 'fast switching' i.e. at $\tau_f = \frac{0.5}{\omega_0}$ we see that starting with an initial state of high value of n, the chances of cross-excitation is higher compared to starting for a lower value of n . This is due to the fact that in the regime of higher n, the wavefunction for the initial and final harmonic well sharply peaks towards the end of the well and hence differences between m, $m+2$, $m-2$ are washed away and they become alike.

4.4.6.4 Work probability distribution P(W,τ_f)

Let us now discuss the work distribution that is obtained by repeating the protocol many time and collecting statistics. For a conservative evolution like being treated here, the work probability distribution is obtainable directly from the conditional probability distribution (P(m|n; τ_f) introduced in the previous section. It is defined as

$$\mathrm{P}(\mathrm{W}, \tau_{\mathrm{f}}) = \sum_{\mathrm{m,n}} \mathrm{P}(\mathrm{m}|\mathrm{n}; \tau_{\mathrm{f}})\mathrm{P}(\mathrm{n}, \beta)\ \delta(\mathrm{W} - (\frac{\tilde{\mathrm{E}}_{\mathrm{m}} - \mathrm{E}_{\mathrm{n}}}{\hbar\omega_0})) \tag{4.81}$$

The quantity 'W' defined in Eq.4.81 is the work done defined in Eq.4.64. In Eq.4.81, $\mathrm{P}(\mathrm{n}, \beta)$ is the probability of sampling the initial state with a quantum index 'n'. Since, we start with an initial thermal distribution at inverse temperature β, $\mathrm{P}(\mathrm{n}, \beta)$ is

$$\mathrm{P}(\mathrm{n}, \beta) = \frac{\exp(-\beta \mathrm{E}_{\mathrm{n}})}{\sum_{\mathrm{n}} \exp(-\beta \mathrm{E}_{\mathrm{n}})} \tag{4.82}$$

P(m|n) has been defined in previous section in Eq.4.76.

4.4.6.5 <u>W > 0</u>

From Eq.4.64, we see that this case is achieved if m $\geq \frac{n\omega_0}{\omega_{\tau_f}} - 0.5$ (subject to constraints m+n= 2k $\forall k \in \{0, 1, 2, 3...\}$. We see from Fig.4.12 that the likelihood or the probability associated with transitions of this kind is higher than in the reverse case (to be discussed below) as in Fig.4.12. There are two categories of work for which this condition is true. The first being the case when $n = m$ This case is represented as blue bars in the central top region of Fig.4.12 and in the four panels of Fig.4.13. We see from Fig.4.13, the blue bars decreases exponentially in height for higher n in congruence with the property of the sampling thermal distribution. This is also evident from the fact that when temperature is raised the distribution becomes shallower(left vs right panel in Fig.4.13). Substituting m=n in Eq.4.64 and using the ratio of $\frac{\omega_0}{\omega_{\tau_f}}$ to be $\frac{1.2566}{1.4199}$, we see that for n=10, W$\approx$ 1.2395 and for n=15 , W$\approx$ 1.8298. However, the highest temperature used in the simulation is 0.3 mK for which the probability for sampling an initial state indexed by n where n$\geq$ 15 is $\leq$ 6 % of the ground state population (n=0). This explains why P(W,τ_f) which is sensitive to P(n,β) drops sharply for large positive values of work. Also with switching time the distribution is practically unchanged as $P(m|n,\tau_f)$ of such processes is close to 1 anyway (see Fig.4.9. We also see from the same figure that the gap $\Delta = \frac{\mathrm{W}-\Delta\mathrm{F}_{\mathrm{act}}}{\hbar\omega_{\tau_f}}$ decreases with increasing temperature and switching time. Let us now move onto the next case ($n \leq m$) as discussed in Fig.4.14. The green bars in Fig.4.14 decreases in amplitude when we move to the adiabatic limit (see y-scale of top left vs bottom left panel in the same figure) in agreement with Fig.4.9. Also with temperature we see the very blue bars as seen in Fig.4.13 starts to appear for large values of n.

4.4.6.6 W $<$ 0

From Eq.4.64, we see that if m $< \frac{n\omega_0}{\omega_{\tau_f}} - 0.5$ (subject to constraints m+n= 2k $\forall k \in \{0, 1, 2, 3...\}$. Coupled with the fact that 'm' needs to be a non-negative integer, this places a restriction on the accessible value of n especially for an initial state indexed by low n. The latter is true because the range of temperature accessible in the simulation is 0.1 mK-0.3 mK for which only low values of n are likely to be sampled. We thus see from right bottom most panel in Fig.4.12 that the likelihood or the probability associated with transitions of this kind is very lower than for $W \geq 0$. In Fig.4.15, we plot the red bars showing such transitions in detail. We see just like with the green bars in the previous case, the red bars decreases in amplitude with increasing switching time (See y-scale of top left and bottom left panel of Fig.4.15. The sensitivity to temperature is mild as it only changes the sampling probability of the starting state n

4.4.6.7 Variation with switching time and temperature

In Fig.4.12 we see the plot of P(W,τ_f) wherein several important regions are highlighted. The details of each region along with their respective dependancies on switching time and temperature are plotted in Fig.4.13, Fig.4.14 and Fig.4.15. From these plots, two observations are imminent.

- For 'fast' switching times i.e. when $\tau_f < \frac{1}{\omega_0}$ we are in the non-adiabatic regime. We see that in such cases, the probability of obtaining 'high' magnitudes of W for W $>$

0 and $m \neq n$ and as well as W $<$ 0 and $m \neq n$ are both high. These probabilities slowly decline as we approach the adiabatic limit as discussed before

- At a given switching time, on decreasing temperature (or increasing inverse temperature β), the distribution attains the same feature as that for moving to the adiabatic limit. In other words, probability for attaining higher magnitudes of work (W) becomes negligeble. This is due to the fact, that at lower temperature , the probability of sampling an initial state indexed by a high value of n exponentially decreases (characteristic of thermal distribution). We have already seen before in Fig.4.11 that P(m|n; τ_f) for high n is higher compared to for lower n, so chances of cross-excitation (which if happened could have created a higher W in absolute magnitude) decreases with decreasing temperature.

In the next section we shall discuss few moments of this distribution. Note that in this section we have identified the (n, m) pairs of only the dominant transitions (n=m and $n = m \pm 2$) in all the plots. There are other transitions (like the kind $n = m \pm 4, 6, 8$....etc) which are present but smaller in amplitude and farther away in the x-scale (work axis). They can also be identified and analyzed similarly. However while computing the moments in the next section, the full distribution including such transitions are taken into account so as to preserve normalization of probability to high decimal places.

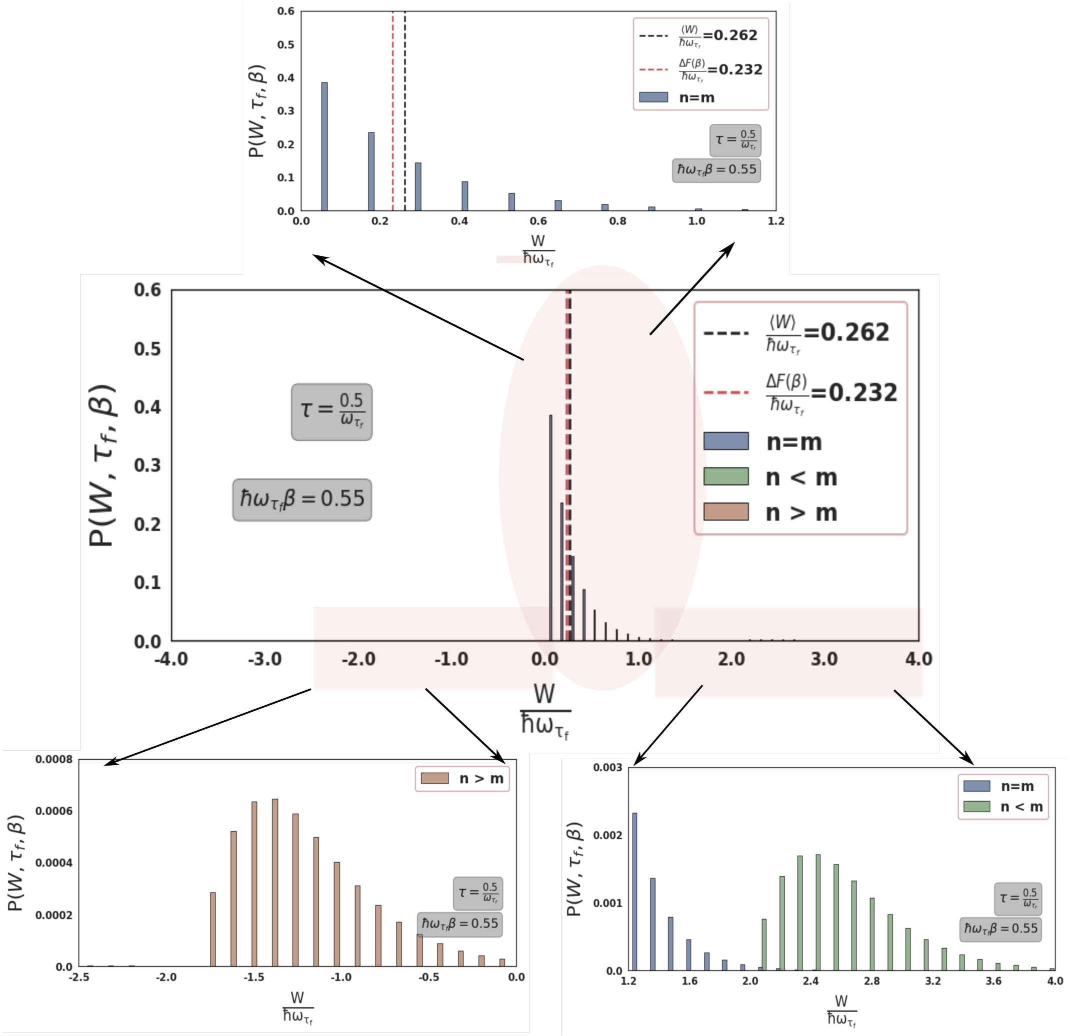

Figure 4.12: The full work distribution $\mathrm{P}(\mathrm{W}, \tau_\mathrm{f})$ computed for a specific value of temperature and switching time as indicated in the plot. The important regions of the plot are blown up to account for the differing scale. The central region (blown up in the top panel corresponds to transitions of the kind $n = m$ (see Fig.4.13). The lower left panel ($\frac{W}{\hbar\omega_{\tau_f}} < 0$) corresponds to transitions of the kind $n > m$ (see Fig.4.15) and the lower right panel corresponds to transition of the kind $n < m$ (see Fig.4.14). To be specific as is evident from Fig.4.15 and Fig.4.14 we consider transitions of the kind $n = m \pm 2$ only. Apart from this there are other transitions (regimes in the plot) too on either side ($n = m \pm 2k \, \forall \, k \in 2, 3, \ldots$) but they have not been discussed due to insignificant probability of occurrence. However while computing the moments as in the next section, the full distribution is taken into account. The initial frequency is $\frac{\omega_0}{2\pi} = 0.200$ MHz and final terminal frequency is $\frac{\omega_{\tau_f}}{2\pi} = 0.226$ MHz

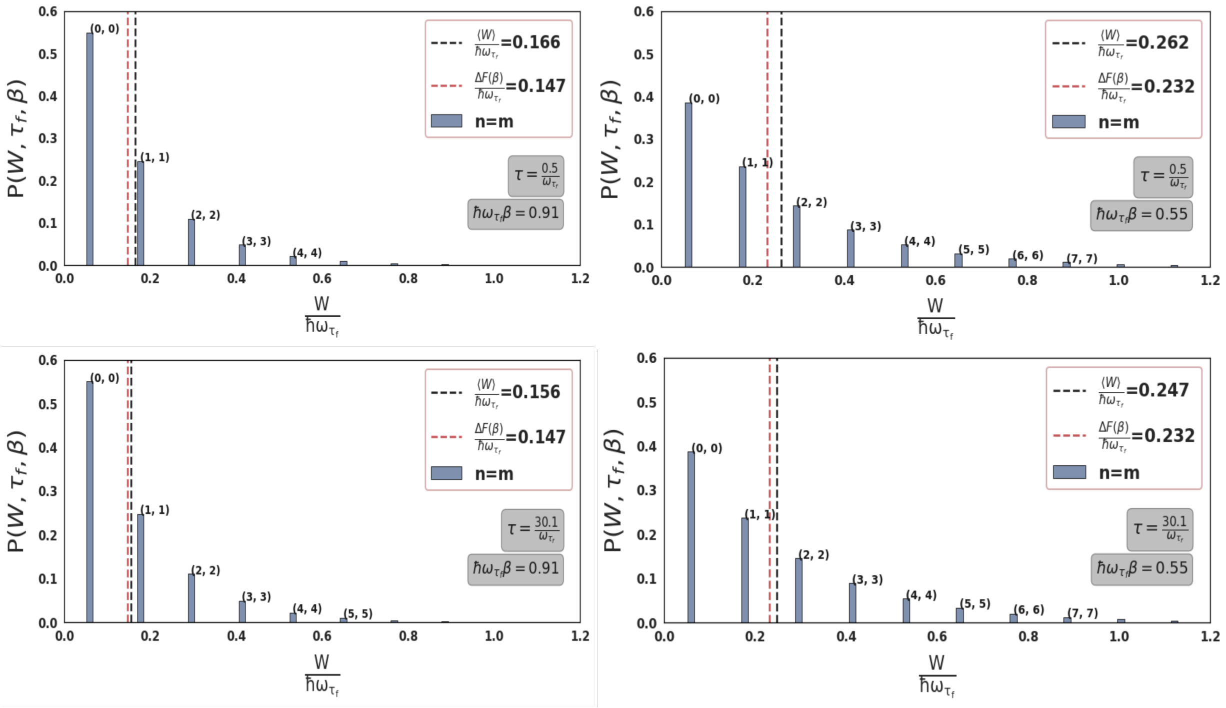

Figure 4.13: The work distribution $\mathrm{P(W, \tau_f)}$ computed for different values of temperature and switching time as indicated in the plot for values of $0.0 \leq \frac{W}{\hbar\omega_{\tau_f}} \leq 1.2$. Thus the central region in Fig.4.12 which corresponds to $n = m$ type transitions are focused and discussed in this plot only as is evident from the x-scale. The (n, m) pairs responsible for creating the corresponding transition for centre of each bar is highlighted on top of the bar. The exponential fall for higher n is attributable to the fact that the initial state is sampled from a thermal distribution of characteristic inverse temperature $\hbar\omega_{\tau_f}\beta$. For higher temperature $\hbar\omega_{\tau_f}\beta = 0.55$, the distribution is thus shallower as is seen from the right panels of the plot. The plots are 'nearly' insensitive to the switching time τ_f as for transitions of the kind $\mathrm{P(m|n, \tau_f)}$ will be very close to 1 anyway as is seen in Fig.4.9. The average work value (computed from the full distribution) and the $\frac{\Delta F_{act}}{\hbar\omega_{\tau_f}}$ values are also indicated. We see the gap $\Delta = \frac{\mathrm{W - \Delta F_{act}}}{\hbar\omega_{\tau_f}}$ is always non-negative (more on this later) and decreases when switching time is increased (adiabatic limit) and also decreases with temperature.The initial frequency is $\frac{\omega_0}{2\pi} = 0.200$ MHz and final terminal frequency is $\frac{\omega_{\tau_f}}{2\pi}$ $= 0.226$ MHz

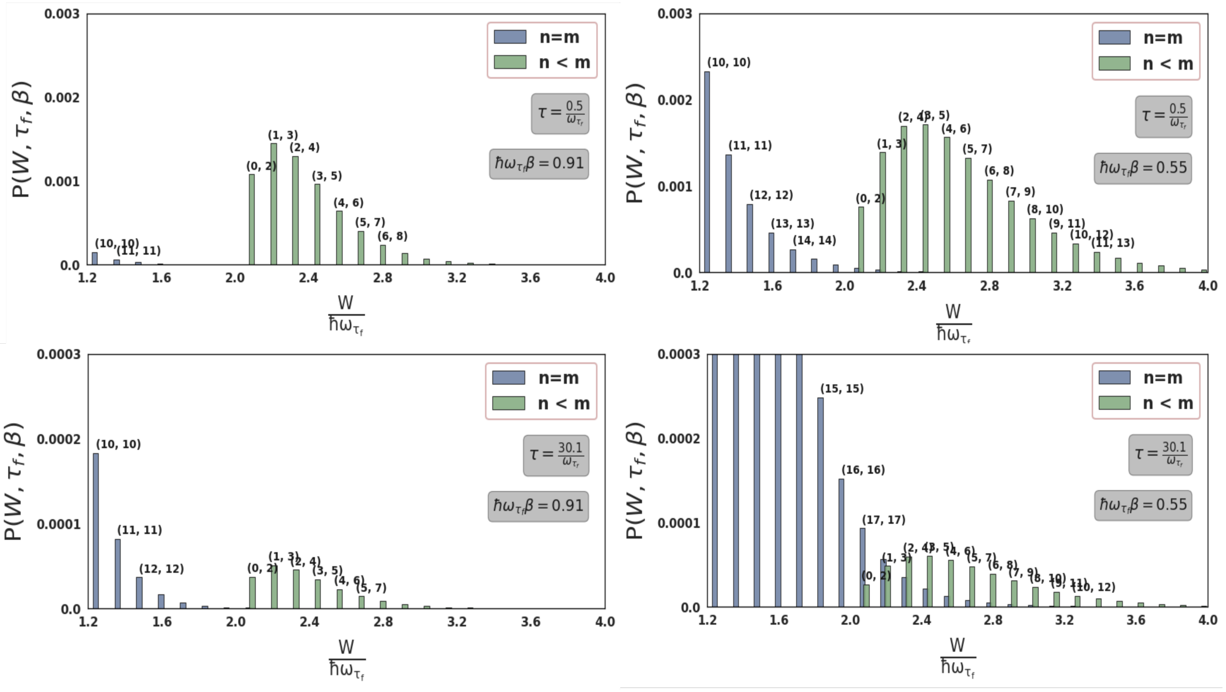

Figure 4.14: The work distribution $\mathrm{P(W, \tau_f)}$ computed for different values of temperature and switching time as indicated in the plot for values of $1.2 \leq \frac{W}{\hbar\omega_{\tau_f}} \leq 4.0$. Thus the bottom rightmost region in Fig.4.12 which corresponds to $n < m$ and also $n = m$ type transitions are focused and discussed in this plot only as is evident from the x-scale. The (n, m) pairs responsible for creating the corresponding transition for centre of each bar is highlighted on top of the bar. The transitions shown in green corresponds to $n < m$ specifically n=m-2 here. The transitions shown in blue are the $n = m$ discussed in Fig.4.13 for very high values of n. For higher switching time (adiabatic limit), we see the transitions in green decreases in amplitude (see y-scale of bottom left panel vs top left panel) in consequence with Fig.4.9. On increasing temperature, we see the blue transitions $(n = m)$ increases in amplitude as the high values of n becomes accessible(see top left and right panel). The green transitions also increases slightly as the probability of the starting value of n increases with temperature too. The exponential fall of the green transitions towards $\frac{W}{\hbar\omega_{\tau_f}} \to 4.0$ is due to the property of thermal distribution for accessing higher values of n. The initial frequency is $\frac{\omega_0}{2\pi} = 0.200$ MHz and final terminal frequency is $\frac{\omega_{\tau_f}}{2\pi} = 0.226$ MHz

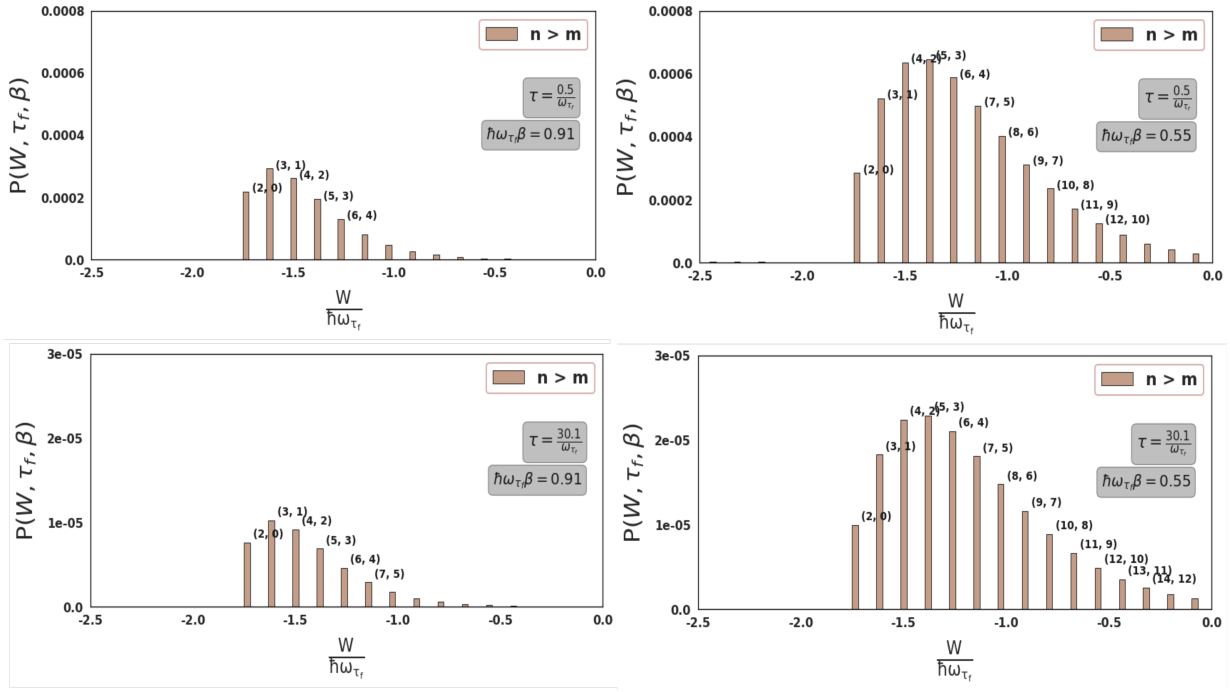

Figure 4.15: The work distribution $\mathrm{P(W,\tau_f)}$ computed for different values of temperature and switching time as indicated in the plot for values of $-2.5 \leq \frac{W}{\hbar\omega_{\tau_f}} \leq 0.0$. Thus the bottom leftmost region in Fig.4.12 which corresponds to $n > m$ type transitions are focused and discussed in this plot only as is evident from the x-scale. The (n, m) pairs responsible for creating the corresponding transition for centre of each bar is highlighted on top of the bar. The transitions shown in red corresponds to $n > m$ specifically n=m+2 here. For higher switching time (adiabatic limit), we see the transitions in red decreases in amplitude (see scale of bottom left panel vs top left panel) in consequence with Fig.4.9. On increasing temperature, we see the red transitions $(n = m)$ increases slightly in amplitude as the high values of n becomes accessible(see top left and right panel). The exponential fall of the red transitions towards $\frac{W}{\hbar\omega_{\tau_f}} \to 0$ is due to the property of thermal distribution for accessing higher values of n. The initial frequency is $\frac{\omega_0}{2\pi} = 0.200$ MHz and final terminal frequency is $\frac{\omega_{\tau_f}}{2\pi} = 0.226$ MHz

4.4.6.8 Two important moments of P(W,τ_f)

4.4.6.9 1)$\langle \exp(-\beta \mathrm{W}) \rangle$

The first moment which we shall discuss is the moment of the Jarynski's function exp($-\beta$W) computed from the probability distribution P(W,τ_f) as

$$\langle \exp(-\beta \mathrm{W}) \rangle = \int \mathrm{P}(\mathrm{W}, \tau_{\mathrm{f}}) \exp(-\beta \mathrm{W}) \mathrm{dW} \tag{4.83}$$

Fig.4.16(b) plots the RHS of Eq.4.83 as a function of switching time (τ_f). We see that this moment is independent of switching rate. This result is powerful as it gives an important route to compute thermodynamic properties like ΔF(β) i.e. Free energy change even by performing the protocol elaborated in section4.4.5 without resorting to the adiabatic limit. In other words, one can initiate the experimental protocol and vary the Hamiltonian arbitrarily fast yet we can get the quantity of interest. Fast switching has a couple of advantages, the most important of which is that during the execution of the protocol, the ion is exposed to optical tweezer for a very short span of time only and hence it is less vulnerable to decoherence induced by motional heating and/or photon back-scattering. We see that is strongly dependant on temperature.

This temperature dependance can be removed if we define a new quantity

$$\Delta = \frac{\mathrm{W} - \mathrm{W}_0}{\hbar \omega_0} \tag{4.84}$$

One can compute the average of Eq.4.84 such that the following condition is true

$$\langle \exp(-\beta \hbar \omega_0 \Delta) \rangle = 1 \tag{4.85}$$

Then from Eq.4.54 and Eq.4.55, we see that for Eq.4.85 to be true, $\mathrm{W}_0 = \Delta \mathrm{F}$ i.e. it should be equal to the thermal free energy change. In Fig.4.16(b), we see that the deviation of the RHS of Eq.4.85 from 1 with W_0 being chosen to be the free energy change at the respective temperature. The error is independent of switching time and temperature and is of the order of 10^{-11}.

4.4.6.10 (2)$\langle(\frac{\mathrm{W}-\mathrm{W}_0}{\hbar\omega_0})\rangle$ s.t. $\mathrm{W}_0 = \Delta\mathrm{F}(\beta)$ from (1)

The second moment which we shall discuss now is the following

$$\begin{aligned}\langle\Delta\rangle = \langle(\frac{\mathrm{W}-\mathrm{W}_0}{\hbar\omega_0})\rangle &= \langle(\frac{\mathrm{W}-\Delta\mathrm{F}}{\hbar\omega_0})\rangle \qquad \because \text{ obtained from Eq.4.85} \\ &= \int \mathrm{P}(\mathrm{W},\tau_\mathrm{f})(\frac{\mathrm{W}-\Delta\mathrm{F}}{\hbar\omega_0})\mathrm{dW} \end{aligned} \tag{4.86}$$

The RHS in Eq.4.86 is actually non-negative. To prove this let us consider the following situation. Let the final state of the system after the termination of the protocol be denoted by $\rho(\tau_f) = |m\rangle\langle m|$. By final state we mean the state of the system after being projected onto the eigenbasis of the final Hamiltonian. Note that our protocol consists of three steps- an initial projective measurement onto the eigenbasis of the initial Hamiltonian, a dynamical evolution to change a Hamiltonian, a final projective measurement to get any of the Fock state of the final Hamiltonian. In general after the dynamical evolution, the state of the system will be a superposition of the Fock states of the final Hamiltonian but the final projective measurement will pick out a particular Fock state. It is worth noting as has been said before, that this state is not the thermal state of the final Hamiltonian ($\mathrm{H}(\tau_\mathrm{f})$) (thermal states are incoherent superposition). Let the thermal state of this Hamiltonian be denoted by $\rho_{th}(\mathrm{H}(\tau_\mathrm{f}))$. Now let us compute the quantum relative entropy between $\rho(\tau_f)$ and $\rho_{th}(\mathrm{H}(\tau_\mathrm{f}))$.

$$S(\rho(\tau_f)||\rho_{th}(\mathrm{H}(\tau_\mathrm{f}))) = \mathrm{Tr}(\rho(\tau_\mathrm{f})\ln(\rho(\tau_\mathrm{f}))) - \mathrm{Tr}(\rho(\tau_\mathrm{f})\ln(\rho_\mathrm{th}(\mathrm{H}(\tau_\mathrm{f})))) \tag{4.87}$$

Care should be taken in defining the quantum relative entropy[114]. For any two state σ and σ', $\mathrm{S}(\sigma\ ||\sigma')$ need not be defined until the $\mathrm{supp}(\sigma) \subseteq \mathrm{supp}(\sigma')$ where

$$\mathrm{supp}(\mathrm{X}) = \{\mathrm{v}|\mathrm{Xv} \neq 0 \ \ \forall \mathrm{v} \in \mathcal{C}^\mathrm{n},\ \ \mathrm{X} \in \mathcal{L}(\mathcal{C}^\mathrm{n})\} \tag{4.88}$$

Luckily, for us since we are following the two-point measurement scheme wherein the final state of the system $\rho(\tau_f)$ is projected on to the eigenbasis of the final Hamiltonian $\mathrm{H}(\tau_\mathrm{f})$ and $[\rho_{th}(\mathrm{H}(\tau_\mathrm{f})), \mathrm{H}(\tau_\mathrm{f})]$=0 for being the state at thermal equilibrium, we immediately have

$\mathrm{supp}(\rho(\tau_\mathrm{f})) \subseteq \mathrm{supp}(\rho_\mathrm{th}(\mathrm{H}(\tau_\mathrm{f})))$. Thus continuing from Eq.4.87 we have

$$\begin{aligned}
S(\rho(\tau_f)||\rho_{th}(\mathrm{H}(\tau_\mathrm{f}))) &= \mathrm{Tr}(\rho(\tau_\mathrm{f})\mathrm{ln}(\rho(\tau_\mathrm{f}))) - \mathrm{Tr}(\rho(\tau_\mathrm{f})\mathrm{ln}(\rho_\mathrm{th}(\mathrm{H}(\tau_\mathrm{f})))) \\
&= \mathrm{Tr}(\rho(\tau_\mathrm{f})\mathrm{ln}(\rho(\tau_\mathrm{f}))) - \mathrm{Tr}(\rho(\tau_\mathrm{f})\mathrm{ln}(\exp(\beta\mathrm{F}(\tau_\mathrm{f}) - \beta\mathrm{H}(\tau_\mathrm{f})))) \\
&\because \rho_{th}(\mathrm{H}(\tau_\mathrm{f})) = \exp(\beta\mathrm{F}(\tau_\mathrm{f}) - \beta\mathrm{H}(\tau_\mathrm{f})) \\
&= \mathrm{Tr}(\rho(\tau_\mathrm{f})\mathrm{ln}(\rho(\tau_\mathrm{f}))) - \mathrm{Tr}(\rho(\tau_\mathrm{f})(\beta\mathrm{F}(\tau_\mathrm{f}) - \beta\mathrm{H}(\tau_\mathrm{f}))) \\
&= \mathrm{Tr}(\rho(\tau_\mathrm{f})\mathrm{ln}(\rho(\tau_\mathrm{f}))) - \beta\mathrm{F}(\tau_\mathrm{f})\mathrm{Tr}(\rho(\tau_\mathrm{f})) + \beta\mathrm{Tr}(\rho(\tau_\mathrm{f})\mathrm{H}(\tau_\mathrm{f})) \\
&= -\mathrm{S}(\rho(\tau_\mathrm{f})) - \beta\mathrm{F}(\tau_\mathrm{f}) + \beta\mathrm{Tr}(\rho(\tau_\mathrm{f})\mathrm{H}(\tau_\mathrm{f})) \\
&= -\mathrm{S}(\rho(0)) - \beta\mathrm{F}(\tau_\mathrm{f}) + \beta\mathrm{Tr}(\rho(\tau_\mathrm{f})\mathrm{H}(\tau_\mathrm{f})) \\
&\because \text{ evolution is unitary } \mathrm{S}(\rho(0)) = \mathrm{S}(\rho(\tau_\mathrm{f})) \\
&= -\mathrm{S}(\rho(0)) - \beta\mathrm{F}(\tau_\mathrm{f}) + \beta\mathrm{Tr}(\rho(\tau_\mathrm{f})\mathrm{H}(\tau_\mathrm{f})) + \beta\mathrm{Tr}(\rho(0)\mathrm{H}(0)) - \beta\mathrm{Tr}(\rho(0)\mathrm{H}(0)) \\
&= \beta\mathrm{F}(0) - \beta\mathrm{F}(\tau_\mathrm{f}) + \beta\mathrm{Tr}(\rho(\tau_\mathrm{f})\mathrm{H}(\tau_\mathrm{f})) - \beta\mathrm{Tr}(\rho(0)\mathrm{H}(0)) \\
&= \beta(\mathrm{F}(0) - \mathrm{F}(\tau_\mathrm{f}) + \mathrm{Tr}(\rho(\tau_\mathrm{f})\mathrm{H}(\tau_\mathrm{f})) - \mathrm{Tr}(\rho(0)\mathrm{H}(0))) \\
&= \hbar\omega_0 \frac{\beta(\mathrm{F}(0) - \mathrm{F}(\tau_\mathrm{f}) + \mathrm{Tr}(\rho(\tau_\mathrm{f})\mathrm{H}(\tau_\mathrm{f})) - \mathrm{Tr}(\rho(0)\mathrm{H}(0)))}{\hbar\omega_0} \\
&= \hbar\omega_0\beta\frac{(-\Delta\mathrm{F}(\beta) + \mathrm{W})}{\hbar\omega_0} \\
&= \hbar\omega_0\beta\frac{(\mathrm{W} - \Delta\mathrm{F}(\beta))}{\hbar\omega_0} \qquad (4.89)
\end{aligned}$$

Using Eq.4.89 and Eq.4.86, one can say the following

$$\begin{aligned}
\langle(\frac{\mathrm{W} - \Delta\mathrm{F}(\beta)}{\hbar\omega_0})\rangle &= \int \mathrm{P}(\mathrm{W}, \tau_\mathrm{f})(\frac{\mathrm{W} - \Delta\mathrm{F}(\beta)}{\hbar\omega_0})\mathrm{dW} \\
&= \frac{1}{\hbar\omega_0\beta}\int \mathrm{P}(\mathrm{W}, \tau_\mathrm{f})\mathrm{S}(\rho(\tau_\mathrm{f})||\rho_\mathrm{th}(\mathrm{H}(\tau_\mathrm{f})))\mathrm{dW} \\
&\geq 0 \qquad (4.90)
\end{aligned}$$

The last line i.e. Eq.4.89 follows from the usage of Klein's inequality [115] which can be used to prove non-negativity of quantum relative entropy. This Eq.4.90 is powerful. To appreciate this point, let us relate $\langle(\frac{\mathrm{W}-\Delta\mathrm{F}(\beta)}{\hbar\omega_0})\rangle$ to the entropy changes in the system and the surroundings during the execution of the process. Since $\hbar\omega_0$ is a non-negative constant energy scale factor, we just have to focus our discussion on $\langle(\mathrm{W} - \Delta\mathrm{F}(\beta)\rangle$

$$\begin{aligned}
\langle(\mathrm{W} - \Delta\mathrm{F}(\beta)\rangle &= \langle\mathrm{W}\rangle - \Delta\mathrm{F}(\beta) \\
&= \langle\mathrm{W}\rangle - \Delta\mathrm{E}(\beta) + \frac{\Delta\mathrm{S}(\beta)}{\beta\mathrm{k_B}} \quad (\mathrm{F} \ = \mathrm{E} \ - \ \frac{\mathrm{S}}{\beta\mathrm{k}}, \text{ process considered at fixed T or } \beta) \\
&= \langle\mathrm{W}\rangle - \langle\mathrm{Q}\rangle - \langle\mathrm{W}\rangle + \frac{\Delta\mathrm{S}(\beta)}{\beta\mathrm{k_B}} \\
&= -\langle\mathrm{Q}\rangle + \frac{\Delta\mathrm{S}(\beta)}{\beta\mathrm{k_B}} \\
&= \frac{-\beta k_B\langle\mathrm{Q}\rangle + \Delta\mathrm{S}(\beta)}{\beta k_B} \qquad (4.91)
\end{aligned}$$

$\langle\mathrm{F}(\beta)\rangle$ in the above equations pertains to the system only and is the free energy change between the thermal states of our initial and final Hamiltonian. $\langle\mathrm{W}\rangle$ pertains to the average work done on the system by the agent (henceforth called work reservoir) dynamically changing the Hamiltonian over many realization of the protocol. Care must be taken in interpreting $\langle\mathrm{Q}\rangle$ and $\Delta\mathrm{S}(\beta)$ as we have just said that our evolution is unitary and conservative and hence does not exchange any heat nor creates any entropy in the system. However as seen in set of equations both $\langle\mathrm{Q}\rangle$ and $\Delta\mathrm{S}(\beta)$ originates from the $\langle\mathrm{F}(\beta)\rangle$ term. $\langle\mathrm{Q}\rangle$ is equal to the average heat that the system 'will exchange' if after the termination of the protocol it is connected to a heat reservoir (at inverse temperature β same as the inverse temperature of the thermal state of initial Hamiltonian) and made to equilibriate to the thermal state of the final Hamiltonian. Similarly $\Delta\mathrm{S}(\beta)$ is the entropy change in the system during this final leg of equilibriation (after termination of our protocol) when it is connected to the heat reservoir. Now for a heat reservoir, the following conditions hold

$$\begin{aligned}
\Delta\mathrm{S_{res}}(\beta) &= \langle\mathrm{Q_{res}}\rangle\beta\mathrm{k_B} \\
\langle\mathrm{Q_{res}}\rangle &= -\langle\mathrm{Q}\rangle
\end{aligned}$$

The first condition is due to the large extent and infinitely many degrees of freedom of the heat reservoir. Any energy exchange with the heat reservoir is unable to change the overall energy content of the heat reservoir and hence also keeps its temperature fixed. The last condition follows due to energy conservation as after the termination of our protocol the only mode of energy exchange with the heat reservoir is heat. The work reservoir only exchanges work with the system during the protocol and hence there is no other work done when the system is equilibriating to the thermal state of the final Hamiltonian. That happens solely by exchanging heat with the heat reservoir. So using these conditions in Eq.4.91 we see the following

$$
\begin{aligned}
\langle(\mathrm{W}-\Delta\mathrm{F}(\beta)\rangle &= \frac{-\beta k_B\langle \mathrm{Q}\rangle + \Delta\mathrm{S}(\beta)}{\beta k_B} \\
&= \frac{\beta k_B\langle \mathrm{Q}_{\mathrm{res}}\rangle + \Delta\mathrm{S}(\beta)}{\beta k_B} \\
&= \frac{\Delta\mathrm{S}_{\mathrm{res}}(\beta) + \Delta\mathrm{S}(\beta)}{\beta k_B}
\end{aligned} \tag{4.92}
$$

From Eq.4.90 and from Eq.4.92 it is clear that non-negativity of $\langle(\mathrm{W}-\Delta\mathrm{F}(\beta)\rangle$ as we have proven for a conservative process under unitary evolution guarantees the following

$$
\begin{aligned}
\langle(\mathrm{W}-\Delta\mathrm{F}(\beta)\rangle &= \frac{\Delta\mathrm{S}_{\mathrm{res}}(\beta) + \Delta\mathrm{S}(\beta)}{\beta k_B} \\
&\geq 0 \\
&= \Delta\mathrm{S}_{\mathrm{res}}(\beta) + \Delta\mathrm{S}(\beta) \geq 0
\end{aligned} \tag{4.93}
$$

Eq.4.93 guarantees the non-negativity of entropy change of the universe during the operation (the operation is our protocol to perform work followed by thermal equilibriation with heat reservoir) which takes us from the thermal state of the initial to that of the final Hamiltonian. This is essentially the crux of the second law of thermodynamics and hence Eq.4.90 is basically the quantum deduction of the second law of thermodynamics[116] for systems wherein the evolution is conservative and thus will not result in change in Von-Neumann entropy. Often the quantity $\langle(\mathrm{W}-\Delta\mathrm{F}(\beta)\rangle$ is interpreted as dissipated work. This is because the amount of work which the work reservoir puts into the system is always greater than or equal to the maximum amount recoverable (free energy change). Equality is only under slow reversible conditions hence for most processes (irreversible operations) the extra work put in is always lost to create entropy in the universe as is seen from above set of equations.

In Fig.4.16(a), we plot $\langle(\frac{\mathrm{W}-\Delta\mathrm{F}(\beta)}{\hbar\omega_0})\rangle$ obtained from $\mathrm{P}(\mathrm{W},\tau_f)$ in the previous section for different values of switching time. We see the following

- Unlike $\langle\exp\left(-\beta\hbar\omega_0\Delta_W\right)\rangle$, this moment is sharply dependant on switching time τ_f and hence to use $\langle W\rangle$ as a proxy for $\Delta\mathrm{F}(\beta)$ one has to initiate the protocol at extremely low switching speed. This makes a protocol reliant on this inconvenient and unrealistic. Furthermore in our case the system for such longer exposure to optical tweezer enhances the chances of motional heating and decoherence due to photon-scattering.

- The moment is also dependant on temperature. Increasing temperature increases not only the free energy and hence W − ΔF increases but the work distribution which is parameterically dependant on temperature also changes and becomes more prominent towards the average. This only increases the value of the moment.

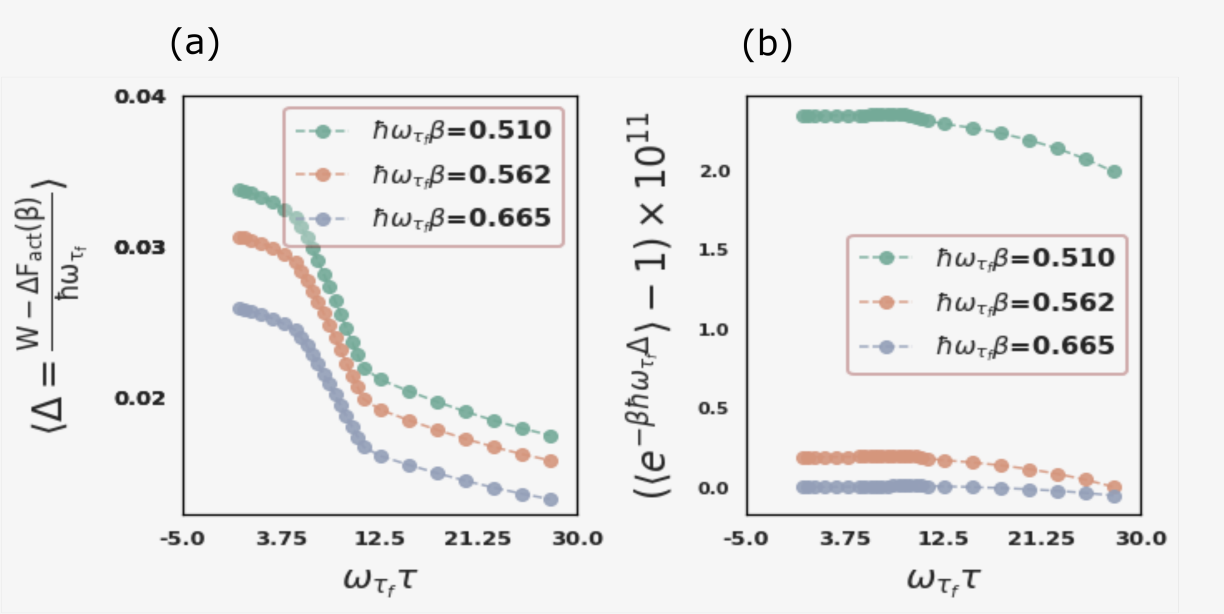

Figure 4.16: The two important moments of the work distribution P(W). (a) The mean of P(W) relative to ΔF_{act}. We see that this moment is dependant both on switching time and temperature (see text for discussion). Only way to use this moment as a proxy for $\Delta F(\beta)$ is in the true adiabatic limit when ($\omega_{\tau_f}\tau_f$ is high). For the best adiabatic switching used in the simulation wherein $\omega_{\tau_f}\tau_f$ =30, even then the error of $\langle W \rangle$ from the actual value of ΔF_{act} is about 10^{-2}. This makes a protocol reliant on this moment unrealistic and inconvenient. Furthermore for such high switching time, the ion is exposed to the optical tweezer longer which enhances its chances of motional heating due to photon scattering.(b) The Jarynski's moment which shows clearly that the function is independent of switching time and temperature with the error/deviation from true value of the order of 10^{-11}. This moment is used in the simulation/protocol for obtaining the Free energy and mode-specific property. The initial frequency is $\frac{\omega_0}{2\pi}$ = 0.200 MHz and final terminal frequency is $\frac{\omega_{\tau_f}}{2\pi}$ = 0.226 MHz

4.4.6.11 Properties of interest

4.4.6.12 1)Free energy of ^{133}Ba^{+} ion as a function of temperature

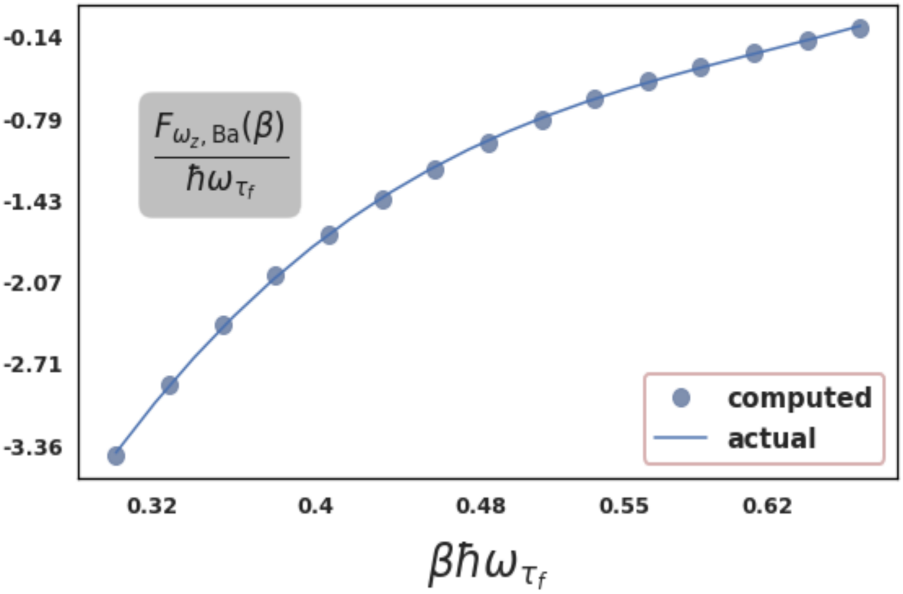

Figure 4.17: The plot of the thermal free energy ($F_{\omega_z,\mathrm{Ba}}(\beta)$) of ^{133}Ba^{+} ion as a function of temperature obtained from the protocol. The curve underneath is the actual values computed from the partition function at the respective temperatures. The initial frequency is $\frac{\omega_0}{2\pi} = 0.200$ MHz and final terminal frequency is $\frac{\omega_{\tau_f}}{2\pi} = 0.226$ MHz

4.4.6.13 2)Thermal Entropy and Internal Energy of $^{133}\mathrm{Ba}^{+}$ ion as a function of temperature

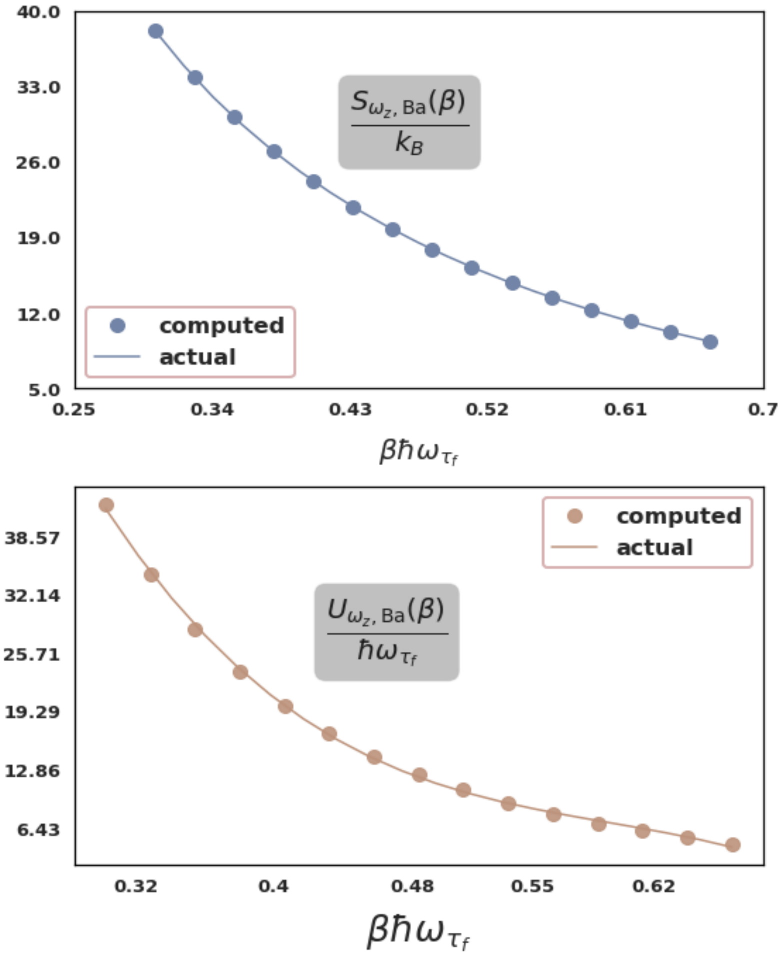

Figure 4.18: The plot of thermal entropy ($\mathrm{S}_{\omega_z,\mathrm{Ba}}(\beta)$) and thermal internal energy ($\mathrm{U}_{\omega_z,\mathrm{Ba}}(\beta)$) of $^{133}\mathrm{Ba}^{+}$ ion as a function of temperature obtained from the protocol. This information is obtainable from the thermal free energy. The curve underneath is the actual values computed from the partition function at the respective temperatures. The initial frequency is $\frac{\omega_0}{2\pi} = 0.200$ MHz and final terminal frequency is $\frac{\omega_{\tau_f}}{2\pi} = 0.226$ MHz

4.5 Conclusion

In this chapter we studied the effect of using optical tweezers on a trapped ion and developed a scheme to dynamically change the power of the optical tweezer and obtain a thermal property of a mixed/dual specie system. The protocol can be extended to multiple ions to obtain mode-specific property and is the subject of current investigation by the author.

Chapter 5

Summary and Outlook

In summary, we have illustrated in the thesis, how to fabricate the trapping electrodes - the four rods and two needles for the assembly of the four-rod trap. These electrodes have been constructed by the author by electro-etching tungsten. We revisited in detail how electro-etching happens mechanistically and also elaborated the causes of the necking behavior seen during the formation of the needles. A new recipe[40] developed by one of the co-worker in the group was used to generate the needles from the rods. The recipe as elaborated in Chapter 2 has a well-defined draw rate for withdrawal of the electrode from the solution and robust against small geometric imperfections in the alignment of the needles with respect to the solution surface. The recipe is still under development and will be a publication soon with the author of this thesis being one of the co-authors. In the following chapter (Chapter 3) we studied how these electrodes are powered. For the rods, a confining potential is generated using a RF source. We elaborated the construction of a balanced helical coil RF resonator that has been used in the currently operational ion-trapping apparatus in the group. We studied the role of each of the key components of the RF resonator and how they contribute towards its voltage amplification and frequency filtering properties. The author not only constructed the RF resonator from scratch, but also simulated the electrode potential and the trajectory of a trapped ion in the RF frequency relayed by the resonator to the rod electrodes. This simulation was done using a home-built code by the author with geometrical parameters from the electrode system actually used in our trapping apparatus. An extension of the RF resonator project is currently underway in the group wherein a sampling and stabilization circuit is being made that will stabilize a fluctuation in the resonance frequency and/or the peak voltage of signal supplied to the trap without the objective of preventing motional heating and constructing better gate sets. In Chapter 4 we study how the trapping potential generated by the RF field can be manipulated using an optical tweezer. For our specific case we target the target the $|S_{1/2}, F = 1, m_F = 0, \pm 1\rangle$ and $|P_{1/2}, F = 0, m_F = 0\rangle$ transition in $^{171}\mathrm{Yb}^+$ using a 375 nm laser beam focused to 1 μm spot size. The beam stabilizes the energy of the ground state of the $^{171}\mathrm{Yb}^+$ ion and leads to additional trapping confinement. Using the optical tweezer we demonstrate how changing the power of the optical tweezer can have a profound effect on the motional mode frequency. This can be harnessed to even compensate for the mass-dependance of the trapping frequency and make the trapping strength of $^{171}\mathrm{Yb}^+$ equivalent to that of $^{133}\mathrm{Ba}^+$. This change if done dynamically at various switching times can be used to infer the thermodynamic properties of a mixed specie ion-system starting from a single-specie ion system as we demonstrate. Using Jarynski's equality[98] we devise a protocol that allows us to infer the thermal free energy at various temperatures of the $^{133}\mathrm{Ba}^+$ ion using only information from $^{171}\mathrm{Yb}^+$ ion. This scheme can be used to even obtain mode-specific properties for multiple ion chains. For example for a 3-ion chain consisting of all $^{171}\mathrm{Yb}^+$ ions, shining the beam onto the second Yb-ion in the chain can allow us to simulate the thermal properties of 3 ion mixed species crystal consisting of two terminal $^{171}\mathrm{Yb}^+$ ions and a central $^{133}\mathrm{Ba}^+$ ion. For such systems, due to presence of many motional modes along a given direction, it would not be possible to obtain a single optical power at which all of the modes of 3 ion $^{171}\mathrm{Yb}^+$ chain (with beam on second Yb ion) come into resonance with a $^{171}\mathrm{Yb}^+$ $^{133}\mathrm{Ba}^+$ $^{171}\mathrm{Yb}^+$ ion chain. Instead one has to carry out the protocol multiple times terminating at various optical powers. Each such set of experiments would yield a Free energy function. One can then interpolate the Free energy function so as to obtain the thermal Free energy at the specific mode frequency. Using this information it is possible to obtain other thermodynamics properties. For example thermal state heat capacity can be obtained experimentally for each of the mode which will provide insight into motional heating due to fluctuating electric field within a given span of time. Such protocols would be undertaken for future extension of this project.

References

[1] I M Georgescu, S Ashhab, and Franco Nori. Quantum simulation. *Rev. Mod. Phys.*, 86(1):153–185, mar 2014.

[2] Richard P Feynman. Simulating physics with computers. *International Journal of Theoretical Physics*, 21(6):467–488, jun 1982.

[3] Seth Lloyd. Universal Quantum Simulators. *Science*, 273(5278):1073–1078, 1996.

[4] Christian Gross and Immanuel Bloch. Quantum simulations with ultracold atoms in optical lattices. *Science*, 357(6355):995–1001, 2017.

[5] R Blatt and C F Roos. Quantum simulations with trapped ions. *Nature Physics*, 8:277, 2012.

[6] Chris Sparrow, Enrique Martín-López, Nicola Maraviglia, Alex Neville, Christopher Harrold, Jacques Carolan, Yogesh N Joglekar, Toshikazu Hashimoto, Nobuyuki Matsuda, Jeremy L O'Brien, David P Tew, and Anthony Laing. Simulating the vibrational quantum dynamics of molecules using photonics. *Nature*, 557(7707):660–667, 2018.

[7] Marco Roth, Nikolaj Moll, Gian Salis, Marc Ganzhorn, Daniel J Egger, Stefan Filipp, and Sebastian Schmidt. Adiabatic quantum simulations with driven superconducting qubits. *Phys. Rev. A*, 99(2):22323, feb 2019.

[8] F. Meinert, M. J. Mark, K. Lauber, A. J. Daley, and H. C. Nägerl. Floquet Engineering of Correlated Tunneling in the Bose-Hubbard Model with Ultracold Atoms. *Physical Review Letters*, 116(20):2–9, 2016.

[9] Ulrich Schneider, Lucia Hackermüller, Jens Philipp Ronzheimer, Sebastian Will, Simon Braun, Thorsten Best, Immanuel Bloch, Eugene Demler, Stephan Mandt, David

Rasch, and Achim Rosch. Fermionic transport and out-of-equilibrium dynamics in a homogeneous Hubbard model with ultracold atoms. *Nature Physics*, 8(3):213–218, 2012.

[10] Florian Schäfer, Takeshi Fukuhara, Seiji Sugawa, Yosuke Takasu, and Yoshiro Takahashi. Tools for quantum simulation with ultracold atoms in optical lattices. *Nature Reviews Physics*, 2(8):411–425, 2020.

[11] D Porras and J I Cirac. Effective Quantum Spin Systems with Trapped Ions. *Phys. Rev. Lett.*, 92(20):207901, may 2004.

[12] L Lamata, J León, T Schätz, and E Solano. Dirac Equation and Quantum Relativistic Effects in a Single Trapped Ion. *Phys. Rev. Lett.*, 98(25):253005, jun 2007.

[13] Uwe R Fischer and Ralf Schützhold. Quantum simulation of cosmic inflation in two-component Bose-Einstein condensates. *Phys. Rev. A*, 70(6):63615, dec 2004.

[14] A M Zagoskin, S Savel'ev, and Franco Nori. Modeling an Adiabatic Quantum Computer via an Exact Map to a Gas of Particles. *Phys. Rev. Lett.*, 98(12):120503, mar 2007.

[15] R Somma, G Ortiz, J E Gubernatis, E Knill, and R Laflamme. Simulating physical phenomena by quantum networks. *Phys. Rev. A*, 65(4):42323, apr 2002.

[16] Sadegh Raeisi, Nathan Wiebe, and Barry C Sanders. Quantum-circuit design for efficient simulations of many-body quantum dynamics. *New Journal of Physics*, 14(10):103017, oct 2012.

[17] Zixuan Hu, Rongxin Xia, and Sabre Kais. A quantum algorithm for evolving open quantum dynamics on quantum computing devices. *Scientific Reports*, 10(1):3301, 2020.

[18] Daniel A Lidar and Ofer Biham. Simulating Ising spin glasses on a quantum computer. *Phys. Rev. E*, 56(3):3661–3681, sep 1997.

[19] Katherine L. Brown, William J. Munro, and Vivien M. Kendon. Using Quantum Computers for Quantum Simulation. *Entropy*, 12(11):2268–2307, 2010.

[20] R Gerritsma, G Kirchmair, F Zähringer, E Solano, R Blatt, and C F Roos. Quantum simulation of the Dirac equation. *Nature*, 463(7277):68–71, 2010.

[21] Ye Wang, Mark Um, Junhua Zhang, Shuoming An, Ming Lyu, Jing-Ning Zhang, L.-M. Duan, Dahyun Yum, and Kihwan Kim. Single-qubit quantum memory exceeding ten-minute coherence time. *Nature Photonics*, 11(10):646–650, 2017.

[22] A H Myerson, D J Szwer, S C Webster, D T C Allcock, M J Curtis, G Imreh, J A Sherman, D N Stacey, A M Steane, and D M Lucas. High-Fidelity Readout of Trapped-Ion Qubits. *Phys. Rev. Lett.*, 100(20):200502, 2008.

[23] T P Harty, D T C Allcock, C J Ballance, L Guidoni, H A Janacek, N M Linke, D N Stacey, and D M Lucas. High-Fidelity Preparation, Gates, Memory, and Readout of a Trapped-Ion Quantum Bit. *Phys. Rev. Lett.*, 113(22):220501, nov 2014.

[24] P V Klimov, J Kelly, Z Chen, M Neeley, A Megrant, B Burkett, R Barends, K Arya, B Chiaro, Yu Chen, A Dunsworth, A Fowler, B Foxen, C Gidney, M Giustina, R Graff, T Huang, E Jeffrey, Erik Lucero, J Y Mutus, O Naaman, C Neill, C Quintana, P Roushan, Daniel Sank, A Vainsencher, J Wenner, T C White, S Boixo, R Babbush, V N Smelyanskiy, H Neven, and John M Martinis. Fluctuations of Energy-Relaxation Times in Superconducting Qubits. *Phys. Rev. Lett.*, 121(9):90502, aug 2018.

[25] H Häffner, C F Roos, and R Blatt. Quantum computing with trapped ions. *Physics Reports*, 469(4):155–203, 2008.

[26] A Friedenauer, H Schmitz, J T Glueckert, D Porras, and T Schaetz. Simulating a quantum magnet with trapped ions. *Nature Physics*, 4(10):757–761, 2008.

[27] Cornelius Hempel, Christine Maier, Jonathan Romero, Jarrod McClean, Thomas Monz, Heng Shen, Petar Jurcevic, Ben P Lanyon, Peter Love, Ryan Babbush, Alán Aspuru-Guzik, Rainer Blatt, and Christian F Roos. Quantum Chemistry Calculations on a Trapped-Ion Quantum Simulator. *Phys. Rev. X*, 8(3):31022, jul 2018.

[28] Zohreh Davoudi, Mohammad Hafezi, Christopher Monroe, Guido Pagano, Alireza Seif, and Andrew Shaw. Towards analog quantum simulations of lattice gauge theories with trapped ions. *Physical Review Research*, 2(2):1–24, 2020.

[29] J Smith, A Lee, P Richerme, B Neyenhuis, P W Hess, P Hauke, M Heyl, D A Huse, and C Monroe. Many-body localization in a quantum simulator with programmable random disorder. *Nature Physics*, 12(10):907–911, 2016.

[30] Philipp Schindler, Daniel Nigg, Thomas Monz, Julio T. Barreiro, Esteban Martinez, Shannon X. Wang, Stephan Quint, Matthias F. Brandl, Volckmar Nebendahl, Christian F. Roos, Michael Chwalla, Markus Hennrich, and Rainer Blatt. A quantum information processor with trapped ions. *New Journal of Physics*, 15, 2013.

[31] S Olmschenk, K C Younge, D L Moehring, D N Matsukevich, P Maunz, and C Monroe. Manipulation and detection of a trapped ${{Yb}}ˆ{+}$ hyperfine qubit. *Phys. Rev. A*, 76(5):52314, nov 2007.

[32] C Ospelkaus, U Warring, Y Colombe, K R Brown, J M Amini, D Leibfried, and D J Wineland. Microwave quantum logic gates for trapped ions. *Nature*, 476(7359):181–184, 2011.

[33] W C Campbell, J Mizrahi, Q Quraishi, C Senko, D Hayes, D Hucul, D N Matsukevich, P Maunz, and C Monroe. Ultrafast Gates for Single Atomic Qubits. *Phys. Rev. Lett.*, 105(9):90502, aug 2010.

[34] J F Poyatos, J I Cirac, and P Zoller. Complete Characterization of a Quantum Process: The Two-Bit Quantum Gate. *Phys. Rev. Lett.*, 78(2):390–393, jan 1997.

[35] Anders S\orensen and Klaus M\olmer. Quantum Computation with Ions in Thermal Motion. *Phys. Rev. Lett.*, 82(9):1971–1974, 1999.

[36] C J Ballance, T P Harty, N M Linke, M A Sepiol, and D M Lucas. High-Fidelity Quantum Logic Gates Using Trapped-Ion Hyperfine Qubits. *Phys. Rev. Lett.*, 117(6):60504, aug 2016.

[37] P C Haljan, K.-A. Brickman, L Deslauriers, P J Lee, and C Monroe. Spin-Dependent Forces on Trapped Ions for Phase-Stable Quantum Gates and Entangled States of Spin and Motion. *Phys. Rev. Lett.*, 94(15):153602, apr 2005.

[38] Colin D Bruzewicz, John Chiaverini, Robert McConnell, and Jeremy M Sage. Trapped-ion quantum computing: Progress and challenges. *Applied Physics Reviews*, 6(2):21314, 2019.

[39] Zhao Wang, Le Luo, Karthik Thadasina, Kim Qian, Jinming Cui, and Yunfeng Huang. Fabrication of ion-trap electrodes by self-terminated electrochemical etching. *EPJ Techniques and Instrumentation*, 3(1):3, 2016.

[40] Nikhil Kotibhaskar. *Design and construction of an ion trapping apparatus for quantum simulation experiments.* Masters' thesis, University of Waterloo, 2019.

[41] Pei Jiang Low. *Tolerable Experimental Imperfections for a Quadrupole Blade Ion Trap and Practical QuditGates with Trapped Ions*. Masters' thesis, University of Waterloo, 2019.

[42] Peter Talkner, Eric Lutz, and Peter Hänggi. Fluctuation theorems: Work is not an observable. *Physical Review E - Statistical, Nonlinear, and Soft Matter Physics*, 75(5):6–7, 2007.

[43] Wolfgang Paul. Electromagnetic Traps for Charged and Neutral Particles (Nobel Lecture). *Angewandte Chemie International Edition in English*, 29(7):739–748, 1990.

[44] H G Dehmelt. Radiofrequency Spectroscopy of Stored Ions I: Storage**Part II: Spectroscopy is now scheduled to appear in Volume V of this series. volume 3 of *Advances in Atomic and Molecular Physics*, pages 53–72. Academic Press, 1968.

[45] H G Dehmelt. Radiofrequency Spectroscopy of Stored Ions II: Spectroscopy**Part I, Sections 1 and 2 of this article appear in Volume 3 of this series. volume 5 of *Advances in Atomic and Molecular Physics*, pages 109–154. Academic Press, 1969.

[46] D. J. Wineland, C. Monroe, W. M. Itano, D. Leibfried, B. E. King, and D. M. Meekhof. Experimental Issues in Coherent Quantum-State Manipulation of Trapped Atomic Ions. *Journal of Research of the National Institute of Standards and Technology*, 103(3):259–328, 1998.

[47] MatWeb Database. Tungsten Datasheet. http://www.matweb.com/search/DataSheet.aspx?MatGU 2011.

[48] Ed Inc Fagan. Datasheet. Technical report.

[49] Raymond A. Serway. *Principles of Physics*. Saunders College Division, 2nd editio edition, 1998.

[50] RF/Microwave Calculators & Conversions - Skin Depth Calculator. https://www.pasternack.com/t-calculator-skin-depth.aspx.

[51] P.J. Linstrom Mallard and W.G. Condensed phase thermochemistry data. *NIST Chemistry WebBook, NIST Standard Reference Database Number 69,National Institute of Standards and Technology, Gaithersburg MD, 20899*, 2020.

[52] Richard D. Holmes, Annie B. Kersting, and Richard J. Arculus. Standard molar Gibbs free energy of formation for Cu2O: high-resolution electrochemical measurements from 900 to 1300 K. *The Journal of Chemical Thermodynamics*, 21(4):351–361, 1989.

[53] Shao Kuan Lee, Hsiu Ching Hsu, and Wei Hsing Tuan. Oxidation behavior of copper at a temperature below 300 °c and the methodology for passivation. *Materials Research*, 19(1):51–56, 2016.

[54] Z Feng, C R Marks, and A Barkatt. Oxidation-Rate Excursions During the Oxidation of Copper in Gaseous Environments at Moderate Temperatures. *Oxidation of Metals*, 60(5):393–408, 2003.

[55] Flora M. Li, Rob Waddingham, William I. Milne, Andrew J. Flewitt, Stuart Speakman, James Dutson, Steve Wakeham, and Mike Thwaites. Low temperature (< 100 °c) deposited P-type cuprous oxide thin films: Importance of controlled oxygen and deposition energy. *Thin Solid Films*, 520(4):1278–1284, 2011.

[56] a a Ogwu. Electrical resistivity of copper oxide thin films prepared by reactive magnetron sputtering. *Manufacturing Engineering*, 24(1):172–177, 2007.

[57] Johan Wendel. Thermodynamics and Kinetics of Tungsten Oxidation and Tungsten Oxide Sublimation in the Temperature Interval 200°–1100°C. *Diploma work*, (October), 2014.

[58] andM. I. Yurchenko V. Ye.Ivanov, Ye.P. Nechiporenko, L. N. Yefimenko. *HIGH TEMPERATURE OXIDATION PROTECTION OFTUNGSTEN*, volume XXX. 1986.

[59] Toshikazu Hirose, Iwazo Kawano, and Minoru Niino. Electrical Conductivity of Tungsten Trioxide (WO3), 1972.

[60] C Davisson and L H Germer. The Thermionic Work Function of Tungsten. *Phys. Rev.*, 20(4):300–330, oct 1922.

[61] Bruce Y K Chao and Frederick A White. Work functions of rhenium and tungsten determined by thermionic and mass spectrometric measurements. *International Journal of Mass Spectrometry and Ion Physics*, 12(5):423–432, 1973.

[62] James G Potter. Temperature Dependence of the Work Function of Tungsten from Measurement of Contact Potentials by the Kelvin Method. *Phys. Rev.*, 58(7):623–632, oct 1940.

[63] C Liu, D Ryding, R W Nielsen, T L Kruy, and T M Kuzay. Cleaning and outgassing studies of machinable tungsten for beamline safety shutters. *Review of Scientific Instruments*, 67(9):3378, 1996.

[64] Wei Han and Feng-Zhou Fang. Investigation of electropolishing characteristics of tungsten in eco-friendly sodium hydroxide aqueous solution. *Advances in Manufacturing*, 2020.

[65] Maryana I. Nave. Materials Science of Electrochemical Formation of Tungsten Nanosharp Probes. (December), 2014.

[66] Anne-sophie Lucier. Preparation and Characterization of Tungsten Tips Suitable for Molecular Electronics Studies. *Thesis paper*, (February):129, 2004.

[67] Olivier L Guise, Joachim W Ahner, Moon-Chul Jung, Peter C Goughnour, and John T Yates. Reproducible Electrochemical Etching of Tungsten Probe Tips. *Nano Letters*, 2(3):191–193, mar 2002.

[68] Bing-Feng Ju, Yuan-Liu Chen, and Yaozheng Ge. The art of electrochemical etching for preparing tungsten probes with controllable tip profile and characteristic parameters. *The Review of scientific instruments*, 82:13707, 2011.

[69] D. J. Berkeland, J. D. Miller, J. C. Bergquist, W. M. Itano, and D. J. Wineland. Minimization of ion micromotion in a Paul trap. *Journal of Applied Physics*, 83(10):5025–5033, 1998.

[70] Q. A. Turchette, C. J. Myatt, B. E. King, C. A. Sackett, D. Kielpinski, W. M. Itano, C. Monroe, and D. J. Wineland. Decoherence and decay of motional quantum states of a trapped atom coupled to engineered reservoirs. *Physical Review A - Atomic, Molecular, and Optical Physics*, 62(5):053807–053801, 2000.

[71] G. Stephen Kelsey. The Anodic Oxidation of Tungsten in Aqueous Base. *Journal of The Electrochemical Society*, 124(6):814, 1977.

[72] J. P. Ibe, P. P. Bey, S. L. Brandow, R. A. Brizzolara, N. A. Burnham, D. P. DiLella, K. P. Lee, C. R. K. Marrian, and R. J. Colton. On the electrochemical etching of tips for scanning tunneling microscopy. *Journal of Vacuum Science & Technology A: Vacuum, Surfaces, and Films*, 8(4):3570–3575, 1990.

[73] A. Michaelides. Density functional theory simulations of water-metal interfaces: Waltzing waters, a novel 2D ice phase, and more. *Applied Physics A: Materials Science and Processing*, 85(4):415–425, 2006.

[74] Javier Carrasco, Andrew Hodgson, and Angelos Michaelides. A molecular perspective of water at metal interfaces. *Nature Materials*, 11(8):667–674, 2012.

[75] Mous Tatarkhanov, D. Frank Ogletree, Franck Rose, Toshiyuki Mitsui, Evgeny Fomin, Sabine Maier, Mark Rose, Jorge I. Cerdá, and Miquel Salmeron. Metal- and hydrogen-bonding competition during water adsorption on Pd(111) and Ru(0001). *Journal of the American Chemical Society*, 131(51):18425–18434, 2009.

[76] Luca Bellarosa, Rodrigo García-Muelas, Guillem Revilla-López, and Núria López. Diversity at the water-metal interface: Metal, water thickness, and confinement effects. *ACS Central Science*, 2(2):109–116, 2016.

[77] Samuel Earnshaw. On the Nature of the Molecular Forces which Regulate the Constitution of the Luminiferous Ether, 1842.

[78] D. Leibfried, R. Blatt, C. Monroe, and D. Wineland. Quantum dynamics of single trapped ions. *Reviews of Modern Physics*, 75(1):281–324, 2003.

[79] D. J. Wineland, C. Monroe, W. M. Itano, B. E. King, D. Leibfried, D. M. Meekhof, C. Myatt, and C. Wood. Experimental primer on the trapped ion quantum computer. *Fortschritte der Physik*, 46(4-5):363–390, 1998.

[80] W W Macalpine and R O Schildknecht. Coaxial Resonators with Helical Inner Conductor. *Proceedings of the IRE*, 47(12):2099–2105, dec 1959.

[81] J. D. Siverns, L. R. Simkins, S. Weidt, and W. K. Hensinger. On the application of radio frequency voltages to ion traps via helical resonators. *Applied Physics B: Lasers and Optics*, 107(4):921–934, 2012.

[82] Q A Turchette, Kielpinski, B E King, D Leibfried, D M Meekhof, C J Myatt, M A Rowe, C A Sackett, C S Wood, W M Itano, C Monroe, and D J Wineland. Heating of trapped ions from the quantum ground state. *Phys. Rev. A*, 61(6):63418, may 2000.

[83] Chung-You Shih. *Holographic Optical Manipulation of Trapped Ions for Quantum Simulation.* Masters' thesis, University of Waterloo, 2019.

[84] Ch. Schneider, M Enderlein, T Huber, and T Schaetz. Optical trapping of an ion. *Nature Photonics*, 4(11):772–775, 2010.

[85] Julian Schmidt, Alexander Lambrecht, Pascal Weckesser, Markus Debatin, Leon Karpa, and Tobias Schaetz. Optical Trapping of Ion Coulomb Crystals. *Phys. Rev. X*, 8(2):21028, may 2018.

[86] Cecilia Muldoon, Lukas Brandt, Jian Dong, Dustin Stuart, Edouard Brainis, Matthew Himsworth, and Axel Kuhn. Control and manipulation of cold atoms in optical tweezers. *New Journal of Physics*, 14(7):73051, jul 2012.

[87] J Dalibard and C Cohen-Tannoudji. Dressed-atom approach to atomic motion in laser light: the dipole force revisited. *J. Opt. Soc. Am. B*, 2(11):1707–1720, nov 1985.

[88] Philipp Strasberg, Gernot Schaller, and Tobias Brandes. Quantum and information thermodynamics: A unifying framework based on repeated interactions. *Physical Review X*, 7(2):1–33, 2017.

[89] Yue Yang, Soumyadipta Basu, and Liping Wang. Radiation-based near-field thermal rectification with phase transition materials. *Applied Physics Letters*, 103(16):163101, oct 2013.

[90] Kota Ito, Kazutaka Nishikawa, Hideo Iizuka, and Hiroshi Toshiyoshi. Experimental investigation of radiative thermal rectifier using vanadium dioxide. *Applied Physics Letters*, 105(25):253503, 2014.

[91] T Werlang, M A Marchiori, M F Cornelio, and D Valente. Optimal rectification in the ultrastrong coupling regime. *Phys. Rev. E*, 89(6):62109, jun 2014.

[92] Kota Ito, Kazutaka Nishikawa, and Hideo Iizuka. Multilevel radiative thermal memory realized by the hysteretic metal-insulator transition of vanadium dioxide. *Applied Physics Letters*, 108(5):53507, 2016.

[93] Geoff Wehmeyer, Tomohide Yabuki, Christian Monachon, Junqiao Wu, and Chris Dames. Thermal diodes, regulators, and switches: Physical mechanisms and potential applications. *Applied Physics Reviews*, 4(4):41304, 2017.

[94] Cyril Elouard, David A Herrera-Martí, Maxime Clusel, and Alexia Auffèves. The role of quantum measurement in stochastic thermodynamics. *npj Quantum Information*, 3(1):9, 2017.

[95] Juyeon Yi, Peter Talkner, and Yong Woon Kim. Single-temperature quantum engine without feedback control. *Phys. Rev. E*, 96(2):22108, aug 2017.

[96] Eric Chitambar and Gilad Gour. Quantum resource theories. *Rev. Mod. Phys.*, 91(2):25001, apr 2019.

[97] Alexei Gilchrist Thomas Guff, Nathan A. McMahon, Yuval R. Sanders. A Resource Theory of Quantum Measurements. 2019.

[98] C Jarzynski. Nonequilibrium Equality for Free Energy Differences. *Phys. Rev. Lett.*, 78(14):2690–2693, apr 1997.

[99] Sai Vinjanampathy and Janet Anders. Quantum thermodynamics. *Contemporary Physics*, 57(4):545–579, 2016.

[100] Vlatko Vedral. An information{\textendash}theoretic equality implying the Jarzynski relation. *Journal of Physics A: Mathematical and Theoretical*, 45(27):272001, jun 2012.

[101] Sebastian Deffner and Christopher Jarzynski. Information Processing and the Second Law of Thermodynamics: An Inclusive, Hamiltonian Approach. *Phys. Rev. X*, 3(4):41003, oct 2013.

[102] Takahiro Sagawa and Masahito Ueda. Generalized Jarzynski Equality under Nonequilibrium Feedback Control. *Phys. Rev. Lett.*, 104(9):90602, mar 2010.

[103] Doron Cohen and Yoseph Imry. Straightforward quantum-mechanical derivation of the Crooks fluctuation theorem and the Jarzynski equality. *Phys. Rev. E*, 86(1):11111, jul 2012.

[104] Carsten Hartmann, Christof Schütte, and Wei Zhang. Jarzynski's Equality, Fluctuation Theorems, and Variance Reduction: Mathematical Analysis and Numerical Algorithms. *Journal of Statistical Physics*, 175(6):1214–1261, 2019.

[105] Michele Campisi, Peter Talkner, and Peter Hänggi. Fluctuation Theorem for Arbitrary Open Quantum Systems. *Phys. Rev. Lett.*, 102(21):210401, may 2009.

[106] Alexey E Rastegin. Non-equilibrium equalities with unital quantum channels. *Journal of Statistical Mechanics: Theory and Experiment*, 2013(06):P06016, jun 2013.

[107] Alexey E Rastegin and Karol \ifmmode \dotZ\else Ż\fiyczkowski. Jarzynski equality for quantum stochastic maps. *Phys. Rev. E*, 89(1):12127, jan 2014.

[108] Michel Le Bellac, Fabrice Mortessagne, and G George Batrouni. *Equilibrium and Non-Equilibrium Statistical Thermodynamics*. Cambridge University Press, Cambridge, 2004.

[109] Shuoming An, Jing-Ning Zhang, Mark Um, Dingshun Lv, Yao Lu, Junhua Zhang, Zhang-Qi Yin, H T Quan, and Kihwan Kim. Experimental test of the quantum Jarzynski equality with a trapped-ion system. *Nature Physics*, 11(2):193–199, 2015.

[110] Gerhard Huber, Ferdinand Schmidt-Kaler, Sebastian Deffner, and Eric Lutz. Employing Trapped Cold Ions to Verify the Quantum Jarzynski Equality. *Phys. Rev. Lett.*, 101(7):70403, aug 2008.

[111] Yehuda B. Band. Adiabatic approximation for the density matrix. *Physical Review A*, 45(9):6643–6651, 1992.

[112] Zhaoyan Wu and Hui Yang. Validity of the quantum adiabatic theorem. *Phys. Rev. A*, 72(1):12114, jul 2005.

[113] Andris Ambainis and Oded Regev. An Elementary Proof of the Quantum Adiabatic Theorem. pages 1–12, 2004.

[114] V. Vedral. *The role of relative entropy in quantum information theory*, volume 74. 2002.

[115] Mohsen Kian and Mohammad W. Alomari. Klein's trace inequality and superquadratic trace functions. 1(January):1–14, 2020.

[116] J M R Parrondo, C Van den Broeck, and R Kawai. Entropy production and the arrow of time. *New Journal of Physics*, 11(7):73008, jul 2009.

[117] Hadi Saboorian-Jooybari and Zhangxin Chen. Calculation of re-defined electrical double layer thickness in symmetrical electrolyte solutions. *Results in Physics*, 15(May):102501, 2019.

[118] Kenneth R Brown, Jungsang Kim, and Christopher Monroe. Co-designing a scalable quantum computer with trapped atomic ions. *Npj Quantum Information*, 2:16034, 2016.

[119] M. H.S. Amin and V. Choi. First-order quantum phase transition in adiabatic quantum computation. *Physical Review A - Atomic, Molecular, and Optical Physics*, 80(6):1–5, 2009.

[120] Rainer Blatt and David Wineland. Entangled states of trapped atomic ions. *Nature*, 453(7198):1008–1015, 2008.

[121] Rayner-Canham. Charge Densities of Selected Ions. *Descriptive Inorganic Chemistry*, pages 13–15, 1976.

[122] F. G. Major and H. G. Dehmelt. Major-Exchange-Collision-Technique-for-rf-Spectroscopy-of-Stored-Ions-1968.pdf, 1968.

[123] Klemen Bohinc, Veronika Kralj-Iglič, and Aleš Iglič. Thickness of electrical double layer. Effect of ion size. *Electrochimica Acta*, 46(19):3033–3040, 2001.

[124] B. B. Blinov, D. Leibfried, C. Monroe, and D. J. Wineland. Quantum computing with trapped ion hyperfine qubits. *Experimental Aspects of Quantum Computing*, 3(October):45–59, 2005.

[125] Song Hi Lee and Jayendran C Rasaiah. Proton transfer and the mobilities of the H+ and OH ions from studies of a dissociating model for water. *The Journal of Chemical Physics*, 135(12):124505, 2011.

[126] J. Edwards. The Mechanism of Electropolishing of Copper in Phosphoric AcidSolutions: II . The Mechanism of Smoothing. *Journal of The Electrochemical Society*, 100(8):223–230, 1953.

[127] Tristan A. Sharp, Spencer L. Thomas, Ekin D. Cubuk, Samuel S. Schoenholz, David J. Srolovitz, and Andrea J. Liu. Machine learning determination of atomic dynamics at grain boundaries. *Proceedings of the National Academy of Sciences of the United States of America*, 115(43):10943–10947, 2018.

[128] M Kulakov, I Luzinov, and K G Kornev. Capillary and Surface Effects in the Formation of Nanosharp Tungsten Tips by Electropolishing. *Langmuir*, 25(8):4462–4468, apr 2009.

[129] H. F. MATARÉ. Main Electronic Features of Grain Boundaries in Metallic and Non-Metallic Materials. *Le Journal de Physique Colloques*, 36(C4):C4–447–C4–454, 1975.

[130] John Goold, Marcus Huber, Arnau Riera, L\'\idia del Rio, and Paul Skrzypczyk. The role of quantum information in thermodynamics{\textemdash}a topical review. *Journal of Physics A: Mathematical and Theoretical*, 49(14):143001, feb 2016.

[131] Mark E Tuckerman, Dominik Marx, and Michele Parrinello. The nature and transport mechanism of hydrated hydroxide ions in aqueous solution. *Nature*, 417(6892):925–929, 2002.

[132] Edyta Łyczkowska-Widłak, Paweł Lochyński, and Ginter Nawrat. Electrochemical polishing of austenitic stainless steels. *Materials*, 13(11):1–25, 2020.

[133] Hui Zheng, Xiang Guo Li, Richard Tran, Chi Chen, Matthew Horton, Donald Winston, Kristin Aslaug Persson, and Shyue Ping Ong. Grain boundary properties of elemental metals. *Acta Materialia*, 186:40–49, 2020.

[134] Saman Setoodeh Jahromy, Felix Birkelbach, Christian Jordan, Clemens Huber, Michael Harasek, Andreas Werner, and Franz Winter. Impact of partial pressure, conversion, and temperature on the oxidation reaction kinetics of Cu 2 O to CuO in thermochemical energy storage. *Energies*, 12(3):1–16, 2019.

[135] G. Yang, B. Wang, K. Tawfiq, H. Wei, S. Zhou, and G. Chen. Electropolishing of surfaces: theory and applications. *Surface Engineering*, 33(2):149–166, 2017.

[136] R Parshad. Grain Boundaries in Metals. *Nature*, (4024):875–876, 1946.

[137] Ryan Burt, Greg Birkett, and X S Zhao. A review of molecular modelling of electric double layer capacitors. *Phys. Chem. Chem. Phys.*, 16(14):6519–6538, 2014.

[138] J. M.R. Parrondo, C. Van Den Broeck, and R. Kawai. Entropy production and the arrow of time. *New Journal of Physics*, 11, 2009.

[139] Donald J. Douglas, Aaron J. Frank, and Dunmin Mao. Linear ion traps in mass spectrometry. *Mass Spectrometry Reviews*, 24(1):1–29, 2005.

[140] Jonathan W Lee, Ali Mani, and Jeremy A Templeton. Atomistic and Molecular Effects in Electric Double Layers at High Surface Charges. *Langmuir*, 31(27):7496–7502, jul 2015.

[141] Gobind Basnet. Fabrication of Tungsten Tips Suitable for Scanning Probe Microscopy by Electrochemical Etching Methods. MAI/ 52-01, 2013.

[142] Jun Ding, Lu-sheng Wang, Kun Song, Bo Liu, and Xia Huang. Molecular Dynamics Simulation of Crack Propagation in Single-Crystal Aluminum Plate with Central Cracks. *Journal of Nanomaterials*, 2017:5181206, 2017.

[143] Michael Johanning, Andrés F. Varón, and Christof Wunderlich. Quantum simulations with cold trapped ions. *Journal of Physics B: Atomic, Molecular and Optical Physics*, 42(15), 2009.

[144] Solar Storms and No-fog Glass. Use Individual Atoms To Perform Calculations. *Scientific American*, 2008.

[145] G.W.A.D. Foundations for microstrip circuit design — Second Edition. *Microelectronics Reliability*, 32(5):739–740, 1992.

[146] David A Welch, B Layla Mehdi, Hannah J Hatchell, Roland Faller, James E Evans, and Nigel D Browning. Using molecular dynamics to quantify the electrical double layer and examine the potential for its direct observation in the in-situ TEM. *Advanced Structural and Chemical Imaging*, 1(1):1, 2015.

[147] S Korenblit, D Kafri, W C Campbell, R Islam, E E Edwards, Z-X Gong, G-D Lin, L-M Duan, J Kim, K Kim, and C Monroe. Quantum simulation of spin models on an arbitrary lattice with trapped ions. *New Journal of Physics*, 14(9):95024, sep 2012.

[148] S Deffner, M Brunner, and E Lutz. Quantum fluctuation theorems in the strong damping limit. {*EPL*} *(Europhysics Letters)*, 94(3):30001, apr 2011.

[149] Andrew N Jordan, Cyril Elouard, and Alexia Auffèves. Quantum measurement engines and their relevance for quantum interpretations. *Quantum Studies: Mathematics and Foundations*, 2019.

[150] Jiteng Sheng, Yuanxi Chao, and James P Shaffer. Strong Coupling of Rydberg Atoms and Surface Phonon Polaritons on Piezoelectric Superlattices. *Phys. Rev. Lett.*, 117(10):103201, aug 2016.

[151] M. Bernards, F.; Kleinmann, M.; Gühne, O.; Paternostro. Daemonic Ergotropy: Generalised Measurements and Multipartite Settings. *Entropy*, 21:771, 2019.

[152] Jesse I Watjen, Bo Zhao, and Zhuomin M Zhang. Near-field radiative heat transfer between doped-Si parallel plates separated by a spacing down to 200 nm. *Applied Physics Letters*, 109(20):203112, 2016.

[153] Dominic V Else, Francisco Machado, Chetan Nayak, and Norman Y Yao. Improved Lieb-Robinson bound for many-body Hamiltonians with power-law interactions. *Phys. Rev. A*, 101(2):22333, feb 2020.

[154] C M Hargreaves. Anomalous radiative transfer between closely-spaced bodies. *Physics Letters A*, 30(9):491–492, 1969.

[155] Lei Wang and Baowen Li. Thermal Logic Gates: Computation with Phonons. *Phys. Rev. Lett.*, 99(17):177208, oct 2007.

[156] Philippe Faist, Mario Berta, and Fernando Brandão. Thermodynamic Capacity of Quantum Processes. *Phys. Rev. Lett.*, 122(20):200601, may 2019.

[157] Vincenzo Alba and Pasquale Calabrese. Quantum information scrambling after a quantum quench. *Phys. Rev. B*, 100(11):115150, sep 2019.

[158] Lei Wang and Baowen Li. Thermal Memory: A Storage of Phononic Information. *Phys. Rev. Lett.*, 101(26):267203, dec 2008.

[159] John P S Peterson, Tiago B Batalhão, Marcela Herrera, Alexandre M Souza, Roberto S Sarthour, Ivan S Oliveira, and Roberto M Serra. Experimental Characterization of a Spin Quantum Heat Engine. *Phys. Rev. Lett.*, 123(24):240601, dec 2019.

[160] Michael Modest. *Radiative Heat Transfer.* Academic Press, 3rd edition, 2013.

[161] Cyril Elouard, George Thomas, Olivier Maillet, J. P. Pekola and A. N. Jordan. A quantum heat switch based on a driven qubit. 2020.

[162] Dakotah Thompson, Linxiao Zhu, Rohith Mittapally, Seid Sadat, Zhen Xing, Patrick McArdle, M Mumtaz Qazilbash, Pramod Reddy, and Edgar Meyhofer. Hundred-fold enhancement in far-field radiative heat transfer over the blackbody limit. *Nature*, 561(7722):216–221, 2018.

[163] Paola Cappellaro Akira Sone, Yi-Xiang Liu. Quantum Jarzynski equality of open quantum systems in one-time measurement scheme. 2020.

[164] Juan Carlos Cuevas and Francisco J García-Vidal. Radiative Heat Transfer. *ACS Photonics*, 5(10):3896–3915, oct 2018.

[165] Teemu Ojanen and Antti-Pekka Jauho. Mesoscopic Photon Heat Transistor. *Phys. Rev. Lett.*, 100(15):155902, apr 2008.

[166] Paul Skrzypczyk, Anthony J Short, and Sandu Popescu. Work extraction and thermodynamics for individual quantum systems. *Nature Communications*, 5(1):4185, 2014.

[167] V Fernández-Hurtado, A I Fernández-Dominguez, J Feist, F J Garcia-Vidal, and J C Cuevas. Super-Planckian far-field radiative heat transfer. *Phys. Rev. B*, 97(4):45408, jan 2018.

[168] B Karimi, J P Pekola, M Campisi, and R Fazio. Coupled qubits as a quantum heat switch. *Quantum Science and Technology*, 2(4):44007, aug 2017.

[169] Rafael Sánchez and Markus Büttiker. Optimal energy quanta to current conversion. *Phys. Rev. B*, 83(8):85428, feb 2011.

[170] Jordan M Horowitz and Todd R Gingrich. Thermodynamic uncertainty relations constrain non-equilibrium fluctuations. *Nature Physics*, 16(1):15–20, 2020.

[171] Giovanni Barontini and Mauro Paternostro. Ultra-cold single-atom quantum heat engines. *New Journal of Physics*, 21(6):63019, jun 2019.

[172] Bao-qing Guo, Tong Liu, and Chang-shui Yu. Multifunctional quantum thermal device utilizing three qubits. *Phys. Rev. E*, 99(3):32112, mar 2019.

[173] Roland R Netz. Approach to equilibrium and nonequilibrium stationary distributions of interacting many-particle systems that are coupled to different heat baths. *Phys. Rev. E*, 101(2):22120, feb 2020.

[174] L Szilard. über die Entropieverminderung in einem thermodynamischen System bei Eingriffen intelligenter Wesen. *Zeitschrift für Physik*, 53(11):840–856, 1929.

[175] Ehud Altman. Many-body localization and quantum thermalization. *Nature Physics*, 14(10):979–983, 2018.

[176] Gaomin Tang and Jian-Sheng Wang. Heat transfer statistics in extreme-near-field radiation. *Phys. Rev. B*, 98(12):125401, sep 2018.

[177] D R Schmidt, R J Schoelkopf, and A N Cleland. Photon-Mediated Thermal Relaxation of Electrons in Nanostructures. *Phys. Rev. Lett.*, 93(4):45901, jul 2004.

[178] Mutsuo M Yanase. Optimal Measuring Apparatus. *Phys. Rev.*, 123(2):666–668, jul 1961.

[179] Wolfgang Niedenzu, Victor Mukherjee, Arnab Ghosh, Abraham G Kofman, and Gershon Kurizki. Quantum engine efficiency bound beyond the second law of thermodynamics. *Nature Communications*, 9(1):165, 2018.

[180] Van A Ngo and Stephan Haas. Demonstration of Jarzynski's equality in open quantum systems using a stepwise pulling protocol. *Phys. Rev. E*, 86(3):31127, sep 2012.

[181] Gavin E Crooks. Entropy production fluctuation theorem and the nonequilibrium work relation for free energy differences. *Phys. Rev. E*, 60(3):2721–2726, sep 1999.

[182] Dakotah Thompson, Linxiao Zhu, Edgar Meyhofer, and Pramod Reddy. Nanoscale radiative thermal switching via multi-body effects. *Nature Nanotechnology*, 15(2):99–104, 2020.

[183] Dmitry A Abanin, Ehud Altman, Immanuel Bloch, and Maksym Serbyn. Colloquium: Many-body localization, thermalization, and entanglement. *Rev. Mod. Phys.*, 91(2):21001, may 2019.

[184] Keye Zhang, Francesco Bariani, and Pierre Meystre. Quantum Optomechanical Heat Engine. *Phys. Rev. Lett.*, 112(15):150602, apr 2014.

[185] Daniel Nickelsen and Michael Kastner. Classical Lieb-Robinson Bound for Estimating Equilibration Timescales of Isolated Quantum Systems. *Phys. Rev. Lett.*, 122(18):180602, may 2019.

[186] Juliette Monsel, Cyril Elouard, and Alexia Auffèves. An autonomous quantum machine to measure the thermodynamic arrow of time. *npj Quantum Information*, 4(1):59, 2018.

[187] Cyril Elouard and Andrew N Jordan. Efficient Quantum Measurement Engines. *Phys. Rev. Lett.*, 120(26):260601, jun 2018.

[188] Carlo Sparaciari, Jonathan Oppenheim, and Tobias Fritz. Resource theory for work and heat. *Phys. Rev. A*, 96(5):52112, nov 2017.

[189] L M A Pascal, H Courtois, and F W J Hekking. Circuit approach to photonic heat transport. *Phys. Rev. B*, 83(12):125113, mar 2011.

[190] R Gallego, A Riera, and J Eisert. Thermal machines beyond the weak coupling regime. *New Journal of Physics*, 16(12):125009, dec 2014.

[191] Raam Uzdin, Amikam Levy, and Ronnie Kosloff. Equivalence of Quantum Heat Machines, and Quantum-Thermodynamic Signatures. *Phys. Rev. X*, 5(3):31044, sep 2015.

[192] Juan Carlos Cuevas. Thermal radiation from subwavelength objects and the violation of Planck's law. *Nature Communications*, 10(1):3342, 2019.

[193] Yohei Morikuni, Hiroyasu Tajima, and Naomichi Hatano. Quantum Jarzynski equality of measurement-based work extraction. *Phys. Rev. E*, 95(3):32147, mar 2017.

[194] Cyril Elouard, David Herrera-Mart\'\i, Benjamin Huard, and Alexia Auffèves. Extracting Work from Quantum Measurement in Maxwell's Demon Engines. *Phys. Rev. Lett.*, 118(26):260603, jun 2017.

[195] Philippe Ben-Abdallah and Svend-Age Biehs. Near-Field Thermal Transistor. *Phys. Rev. Lett.*, 112(4):44301, jan 2014.

[196] C S Adams, J D Pritchard, and J P Shaffer. Rydberg atom quantum technologies. *Journal of Physics B: Atomic, Molecular and Optical Physics*, 53(1):12002, dec 2019.

[197] Tsuyoshi Yamamoto and Takeo Kato. Quantum critical phenomena in heat transport via a two-state system. *Phys. Rev. B*, 98(24):245412, dec 2018.

[198] D Gelbwaser-Klimovsky, N Erez, R Alicki, and G Kurizki. Work extraction via quantum nondemolition measurements of qubits in cavities: Non-Markovian effects. *Phys. Rev. A*, 88(2):22112, aug 2013.

[199] S Das, A.; Ghosh. Measurement Based Quantum Heat Engine with Coupled Working Medium. *Entropy*, 21:1131, 2019.

[200] A E Allahverdyan, R Balian, and Th. M Nieuwenhuizen. Maximal work extraction from finite quantum systems. *Europhysics Letters ({EPL})*, 67(4):565–571, aug 2004.

[201] M. Masius Max Planck. *The theory of heat radiation.* P. Blakiston's Son & Co., 1914.

[202] Xing Zhang Hexin Liu, Haidong Wang. A Brief Review on the Recent Experimental Advances in Thermal Rectification at the Nanoscale. *Appl. Sci.*, 9:344, 2019.

[203] Bernhard Altaner. Nonequilibrium thermodynamics and information theory: basic concepts and relaxing dynamics. *Journal of Physics A: Mathematical and Theoretical*, 50(45):454001, oct 2017.

[204] Huzihiro Araki and Mutsuo M Yanase. Measurement of Quantum Mechanical Operators. *Phys. Rev.*, 120(2):622–626, oct 1960.

[205] Karl Joulain, Younès Ezzahri, Jérémie Drevillon, and Philippe Ben-Abdallah. Modulation and amplification of radiative far field heat transfer: Towards a simple radiative thermal transistor. *Applied Physics Letters*, 106(13):133505, 2015.

[206] Jonne V Koski, Ville F Maisi, Jukka P Pekola, and Dmitri V Averin. Experimental realization of a Szilard engine with a single electron. *Proceedings of the National Academy of Sciences*, 111(38):13786–13789, 2014.

[207] Ronnie Kosloff and Amikam Levy. Quantum Heat Engines and Refrigerators: Continuous Devices. *Annual Review of Physical Chemistry*, 65(1):365–393, 2014.

[208] D. Adams. *The Hitchhiker's Guide to the Galaxy*. San Val, 1995.